Probing interaction and dispersion of carbon nanotubes in metal and polymer matrices

Ekaterina Pavlenko

THÈSE

En vue de l'obtention du

DOCTORAT DE L'UNIVERSITÉ DE TOULOUSE

Délivré par : *l'Université Toulouse 3 Paul Sabatier (UT3 Paul Sabatier)*

Présentée et soutenue le *jeudi 25 septembre 2014* **par :**

Ekaterina PAVLENKO

Probing interaction and dispersion of carbon nanotubes in metal and polymer matrices

---

JURY

Philippe COLOMBAN	Directeur de recherche, UPMC (Paris)	Rapporteur
Christophe LAURENT	Professeur, CIRIMAT (Toulouse)	Président du Jury
Cécile ZAKRI	Professeur, CRPP (Pessac)	Examinatrice
Victoria TISHKOVA-LÉONI	Maître de conférences, CINaM (Marseille)	Examinatrice
Rozenn LE PARC	Maître de conférences, L2C (Montpellier)	Examinatrice
Wolfgang BACSA	Professeur, CEMES (Toulouse)	Directeur de Thèse

---

École doctorale et spécialité :
SDM : Physique de la matière - CO090
Unité de Recherche :
Centre d'Élaboration de Matériaux et d'Etudes Structurales (CEMES) UPR8011 CNRS
Directeur de Thèse :
Wolfgang BACSA - Professeur, CEMES (Toulouse)
Pascal PUECH - Maître de conférences, CEMES (Toulouse)
Rapporteur :
Philippe COLOMBAN - Directeur de recherche, UPMC (Paris)
Jean-Yves CAVAILLÉ - Professeur, INSA (Lyon)

Acknowledgements

First and above all, I would like to express my deepest gratitude to my supervisors Wolfgang Bacsa and Pascal Puech. It was a great pleasure to work with them both professionally and personally throughout the entire duration of my PhD. I am sincerely indebted for their bountiful advice, guidance, and the time spent helping me to improve upon this thesis. I was continuously surrounded by their support, immense knowledge, and enthusiasm, demonstrated best by Pascal's ardency to work late on Friday nights; the true value of which became wholly apparent as time passed (had it not been recognized initially)! I was incredibly fortunate to have supervisors who cared so much about my work. I cannot imagine having better! Thank you so much!

I also gratefully acknowledge Victoria Tishkova-Léoni for giving me inspiration, clear and patient explanations, valuable advice, and especially for her friendship!

Besides my advisors and Victoria, I would like to thank the rest of my thesis committee: the two referees Philippe Colomban and Jean-Yves Cavaillé, the President of the jury Christophe Laurent, and Cécile Zakri and Rozenn Le Parc for their careful reading of the manuscript, thoughtful and detailed comments and suggestions.

I am also thankful to all members of the Carbon group for providing an excellent atmosphere, foremost, the group leader Marc Monthioux for encouraging me to give an oral presentation in French, and to Claudine Puech for her translating assistance.

Furthermore, I would like to thank the technical staff of CEMES: Antoine Zwick, Frédéric Neumayer and Sébastien Moyano for their help with the Raman experiments; Sébastien Joulie and Floran Houdellier for the technical assistance with the TEM; Philippe Salles for his help with the conductivity measurements and Laure Noé for providing an extremely clean preparation laboratory where working was a pleasure.

I also thank the collaborators from the Queen Mary University of London: Andrei Sapelkin, Stephen King, and Richard Heenan for their help with the SANS and SAXS experiments and related discussions; as well as Mark Baxendale for his help with the impedance spectroscopy measurements. My thanks also go to the collaborators from Toulouse: François Boyer from the ICA for the mechanical tests of the CNT/PEEK composites; and Christophe Guiderdoni from the CIRIMAT for the copper samples and the tribological tests.

I would also like to acknowledge my former supervisors from the Lomonosov Moscow State University Alexander Obraztsov and Peter Kopylov, as well as my good friend Alexander Lanin for helping me to develop a scientific background that allowed me to start a PhD.

I am especially grateful to Ivan Nikitskiy for inspiring me in difficult moments and to my friends Victoria Prudkovskaya, Vladimir Prudkovskiy, Anna Kotova, Oleg Polivin, Olena Kraieva, Agnieszka Krawczyńska, Philippe Mallet-Ladeira and Florian Chaumeton for their support and for all the fun we had together during these three years of my PhD. I also thank Maxim and Nina Oprya for coming to my defense all the way from Moscow.

Last but not the least, I would like to thank my family: my grandparents and my aunt for their support, my father for encouraging me to start a PhD and my mother for the careful proof-reading of the manuscript.

Contents

Introduction

Polymer composites are interesting for the aircraft and transport industries due to their light weight and mechanical strength. Utilization of composite materials instead of metallic alloys makes it possible to reduce fuel consumption and manufacturing costs. But most high performance polymers suitable for aerospace applications are electrically insulating. Considerable attention has been given in recent years to improve the electrical conductivity of polymer composites. While conductive polymers are available they are not suitable for structural applications. When mixing conducting polymers with mechanical strong polymers a large mass fraction is needed which drastically degrades the mechanical properties. Adding conducing filler particles turned out to be a better strategy. New carbon materials are promising candidates for their use as filler particles. Fullerenes were discovered in 1985 and are now used as UV absorbers. Using the same synthesis process carbon nanotubes (CNTs) were discovered in 1991. Their small size and perfect structure caught a lot of attention. The high aspect ratio, high Young's modulus and high electrical conductivity of CNTs had the consequence that they are considered for a wide range of applications. Progress in making single layer graphene in 2004 furthermore intensified the interest in carbon nanomaterials. CNTs are a new generation of composite filler materials which can potentially replace conventional fillers. A small quantity of well dispersed CNTs can significantly increase the conductivity of the polymer. A percolation (electrical conductivity) threshold as low as 0.002wt% has been observed for epoxy matrix. Currently, polymer composite is the largest application area for CNTs. When designing a nanocomposite one expects to combine the properties of the matrix and the filler material. However the properties of the filler depend on whether the particles are agglomerated or not. The dispersion of the nanoparticles is a key parameter in improving the properties of the nanocomposite. CNTs are a lot smaller than carbon fibers and as a result the van der Waals interactions are playing a more important role for CNTs. CNTs tend to agglomerate due to their high aspect ratio and large surface area making dispersion challenging. Furthermore incorporation of fillers into a thermoplastic polymer increases its viscosity making the dispersion even more difficult. When using a thermoset like epoxy, the CNTs can be mixed in before polymerization.

The high thermal stability of CNTs gives the opportunity to introduce them into a metal matrix. The high toughness of the CNTs in a metal composite can be used to reduce material losses caused by friction and wear, one of the key engineering challenges of the today's mechanical systems. We were able to show in the course of this work that incorporation of a small amount of double wall CNTs (DWNTs) into copper leads to a significant improvement of the tribological properties such as micro hardness and lubrication leading to a reduction in the wear volume. Establishing a relationship between CNT characteristics and macroscopic behavior of composites is also crucial for mechanical reinforcement of copper wires for high magnetic field coils.

To have better fundamental understanding one needs to study the nanocomposite at microscopic and macroscopic scales. Macroscopic behavior such as the electrical conductivity and tensile deformation depends on the structure at the micrometer scale. However it is often challenging to image nanoparticles in a matrix and monitor their interaction. Elaborate research tools such as neutron scattering, synchrotron radiation

facilities and advanced electronic microscopy are cost intensive while Raman spectroscopy is a versatile and straightforward tool. Raman spectroscopy offers several advantages for microscopic analysis. Since it is a scattering technique, specimens do not need any primary preparation such as sectioning, surface treatment or thinning. Raman spectra can be collected from a very small volume (< 1 μm in diameter). The spectral bands allow the identification of a compound present on a specific location and volume.

In recent years low cost Raman spectrometers have become available. Raman spectroscopy is applied in food industry to detect the product composition (Tellspec®), in geology to examine shale gas minerals (a patent in 2014 was granted for identifying the maturity of the rock with a 1450cm^{-1} Raman band). Raman is also widely used in the characterization of carbon nanomaterials. Raman spectroscopy can be highly sensitive allowing to observe a single nanotube 1.2nm wide with only 10^5 atoms. CNTs have a strong Raman signal with many characteristic spectral bands that can be used to indicate modifications of the CNT when subjected to external influence. CNTs can in turn be used as a tool to probe its surroundings. A single wall tube (SWNT) cannot serve as a local sensor since all the atoms are located on the surface, neither can multiwall tubes (MWNT) due to the fact that most of the atoms are inside and do not directly interact with the environment. In case of DWNTs one tube is exposed to the environment while the other one is not. When comparing the Raman spectra from the inner and outer tubes we can consider DWNTs as molecular sensors.

The subject of this thesis is of primary importance for aerospace industry and for the 'Aerospace Valley' platform in Toulouse. The goal of this work is to contribute to the fundamental understanding of CNT composites.

In this thesis at first I investigate DWNTs as molecular sensors and their possible applications to nanocomposites. Secondly, I study the wear of CNT/copper composites and in the third part I investigate the dispersion of CNTs in a polymer matrix and the modification of the polymer due to the presence of CNTs.

Chapter 1

Composite materials

A composite material is a multi-component system in which components with significantly different physical or chemical properties are blended to form a new material with characteristics different from simply the average of the individual components properties. There are two main categories of composite constituent materials: matrix and filler. The matrix surrounds and supports the filler while the filler impacts its special mechanical and physical properties (strength, stiffness, conductivity etc.) to enhance the matrix properties.

1.1 Matrix

1.1.1 Polymer matrices. PEEK

Polymers are the most widely used matrix materials in modern composites [1]. One of the major reasons why polymer composite materials (PCM) are so attractive is that they can reduce weight of a construction element while maintaining or improving its mechanical characteristics. This property makes polymer composites especially attractive for transportation in general and aerospace applications in particular, since weight reduction leads to lower fuel consumption and emission. Presently, in modern aircrafts up to 50% of the airframe is made from composite materials. Weight reduction of final products is thus 20-50% [2]. Advanced polymer composites do not corrode like metals. The combination of corrosion and fatigue cracking is a significant problem for commercial aluminum fuselage structures [2]. PCMs are relatively easy to process and

they can be molded into complex shapes. This means that a composite part can replace many metallic parts that had to be assembled to achieve the same function; hence it leads to cost reduction. When manufacturing parts made from polymer composites, the waste of material is not more than 30wt%. Whereas, for comparison, for parts from high-strength alloys of aluminum used in the aviation industry, the waste may be up to 90% (of which 70-80% are recycled), this is associated with low series production [3]. Another significant advantage is that the properties of polymer composite materials can be easily controlled by simply changing the composition and preparation conditions [2]. Other important properties that can be obtained include improved wear resistance, enhanced fatigue life, low thermal expansion, low or high thermal conductivity, etc. But an important disadvantage of polymer composites is a nonvisible impact of damage. Thus they need to be better studied to prevent failure.

The properties of the final composite depend strongly on the intrinsic properties of the polymer used. The properties of the composite can be divided into three groups. When trying to enhance and improve the properties of one group, we automatically degrade the others. The first group includes strength, stiffness and heat resistance, the second - plasticity, viscosity and fracture toughness, the third – processability and manufacturability. For example, a polymer with a lower processing temperature is easier to process but this implies that the heat resistance is also low. The goal when constructing a composite material is to find a compromise between these three property groups taking also into account the environmental, economic, market and other aspects.

Thermosets and thermoplastics

Polymers can be divided into two main classes: thermosets (e.g. epoxy, polyester, polyurethane, vulcanized rubber and phenol) and thermoplastics (e.g. polypropylenes, polyethylenes, polyimide (PI), polysulfone (PSU), poly (ether ether ketone) (PEEK), poly (ether ketone ketone) PEKK, polyphenylene sulfide (PPS)).

The first class are typically relatively low viscosity liquids (at the process temperature), which, after introducing a reinforcing material are cured and change irreversibly into an infusible, insoluble highly cross-linked, three-dimensional molecular network that does not melt at high temperatures.

The second group are linear polymers which soften and melt at high temperatures, and return to the solid state upon cooling.

The main advantages of thermosets include good processing properties: low viscosity; good wettability and impregnability of the reinforcing material, relatively low cure temperatures, good adhesion to most fibers, increased heat resistance, resistance to chemical media, water and weather resistance, low permeability for liquids and gases. Their properties can be controlled over a wide range by varying the components, adding modifiers and catalysts, changing curing conditions, etc. But thermosets have a number of disadvantages such as: brittleness, low fracture toughness and impact strength, impossibility of recycling, long curing times, and significant shrinkage in most chemical cases.

Epoxies and polyesters have been the principal polymer matrix materials for several decades, but advanced thermoplastics such as PEEK and PPS are now receiving considerable attention for their excellent toughness and low moisture absorption properties, their simple processing cycles, and high-temperature capabilities.

Aerospace grade epoxies are typically cured at about 177°C and are generally not used at temperatures above 150°C, whereas advanced thermoplastics such as PPS, PI,

and PEEK have melting temperatures in the range of 315-370°C [1]. Other advantages of thermoplastics are: a possibility of recycling, facilitation of product reparation, more efficient methods of processing, less energy consuming, possibility of molding larger and more complex detail configurations, higher productivity, reduced flammability, smoke emission during combustion and combustion products toxicity, high resistance to radiation.

On the other hand, the replacement of thermosets by thermoplastics requires a number of complex technological problems to be solved. Due to a high viscosity melt polymer processing has to be carried out at high temperatures and high pressures.

Amorphous and semi-crystalline thermoplastics

Thermoplastic polymers appear in two states: amorphous and semi-crystalline. Amorphous polymers have a randomly arranged molecular structure while semi-crystalline contain both crystalline and amorphous regions in the same sample.

Amorphous polymers do not have a well-defined melting point. They tend to gradually soften over a relatively wide temperature range known as glass transition temperature (T_g). Above the glass transition, the polymer transforms from a hard and relatively brittle state into a molten or rubber-like state. This transformation is reversible when lowering the temperature and can be repeated many times without affecting the material properties.

In contrast, crystalline polymers have true melting temperatures (T_m) where the polymers turn into a liquid state. The crystallinity of a semi-crystalline polymer strongly depends on the thermal history of the material. Annealing the sample, one can vary the degree of crystallinity and the morphology of the crystal structure [4] [5].

When crystallization takes place from a liquid state, the crystallized areas are highly anisotropic and form crystalline lamellae (Figure 1.1a). These lamellae are formed from folded on themselves local linear chains. Amorphous areas where the monomers were not able to self-organize are present between the crystalline lamellae. The presence of amorphous areas is often due to rapid cooling rates or to defect linkage of monomers. The lamellar structures grow radially from a starting point to form larger structures called spheroids (Figure 1.1b).

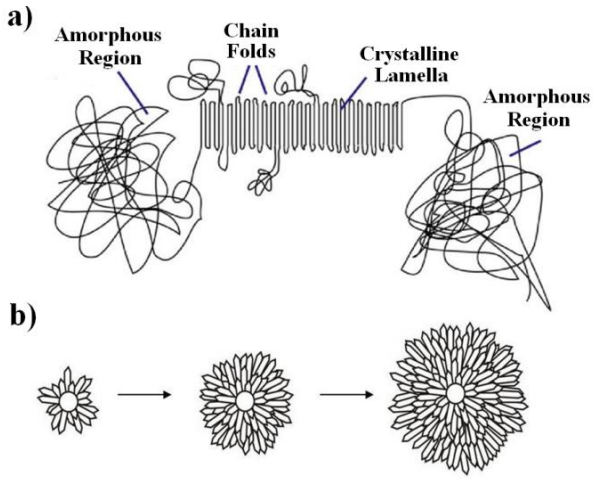

Figure 1.1. a) Semi-crystalline structure b) Spheroids

There are many factors that can cause crystallization at a particular point. For example, it may be either a polymer seed or an external agent (impurity), or a nucleating agent, or a filler particle.

PEEK

Poly (ether ether ketone) (PEEK) is a semi-crystalline thermoplastic polymer suitable for prolonged use at high temperatures. Its chemical structure is shown in Figure 1.2.

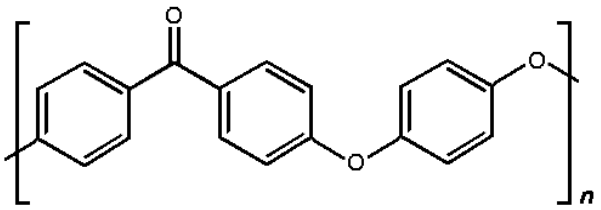

Figure 1.2. PEEK chemical structure.

The mechanical properties and chemical resistance of PEEK depend on the degree of crystallinity which varies slightly with cooling velocity and remains between 30 and 40%. PEEK crystallizes in two steps. The primary crystallization is a spherulite growth from a seed. A spherulite is formed of lamellar stacks separated by amorphous areas. A lamellar stack is approximately 10nm thick and a spherulite is about 10μm in diameter, however the size of the spherulites can vary significantly depending on the thermal history. The secondary crystallization corresponds to the interlaminar crystallization of amorphous areas and thickening of spherulites [6].

Due to deactivated aromatic nature the polymer has a high melting point (334°C) and a high degree of oxidative stability. This allows its long-term use at temperatures ranging from -40° to +250°C and gives PEEK an ability to withstand short-term heating up to 300°C [7].

Despite its high-temperature performance, PEEK can be processed on standard equipment. Corrosive gases are not liberated during processing; consequently, corrosion-resistant materials are unnecessary. Drying for 3 hours at 150°C is recommended. Failure of drying results in bubbling and the occurrence of surface streaking, but no degradation is observed. Consequently, the left over material can be reused.

A distinctive feature of PEEK is that the polymer maintains its excellent mechanical properties, stiffness, fatigue characteristics, load bearing and good dimensional stability even at high temperatures and exposures to chemicals [7]. It is resistant to high energy radiation (X-rays, gamma radiation); has a high resistance to surface electrical discharges, temperature and humidity changes; can be exploited in hot water (even up to 200°C) and is suitable for contacts with food. The polymer is resistant to the action of thermoplastic steams, has low flammability and very low levels of smoke emission when burned. A summary of the main PEEK properties is given in Table 1.1.

Mechanical	Tough, ductile, abrasion resistant Excellent fatigue characteristics Load bearing at high temperature
Thermal	High melting point High continuous service temperature
Flammability	Low flammability, fire, smoke properties
Chemical	Essentially inert to organics High degree of acid and alkali resistance Particularly resistant to high temperature water/steam
Hard radiation	No significant degradation below 1100 Mrad
Processing	Easily processed on conventional equipment

Table 1.1. PEEK—Key Properties [7].

In particular, a high crystalline melting point and outstanding chemical resistance open entirely new applications in aggressive environments. Such applications include cable insulation, monofilaments, coatings, molded parts, and high-strength composites.

Due to its chemical structure, PEEK is compatible with many reinforcing agents. Mixing poly (ether ether ketone) with carbon fibers, graphite, polytetrafluoroethylene (PTFE) or glass fiber significantly improves its properties, increasing frictional quality, mechanical strength, wear resistance, hardness, dimensional stability and other properties.

The price of PEEK is high, typically up to 500€/kg for small quantity (2014). Its use is reserved to technical domains such as medicine and aeronautic.

1.1.2 Metal matrices. Copper

Metal matrix composites (MMCs) have many advantages over conventional metals including a higher specific modulus, higher specific strength, better properties at elevated temperatures, lower coefficients of thermal expansion and better wear resistance. But, their toughness is lower than that of monolithic metals and they are more expensive at present. In comparison with most polymer matrix composites, MMCs have certain superior mechanical properties, namely higher transverse strength and stiffness, greater shear and compressive strengths and better high temperature capabilities. There are also advantages in some of the physical properties of MMCs such as no significant moisture absorption, non-inflammability, high electrical and thermal conductivities, and resistance to most radiations [8]. MMCs are under consideration for a wide range of applications. They have been extensively studied for many years. The primary interest has come from the aerospace industry for airframe and spacecraft components. Now they are increasingly used in automotive, electronics and sport industries.

MMC reinforcements can be generally divided into five major categories: continuous fibers, discontinuous fibers, whiskers, wires and particulate. With exception of wires, which are metals, reinforcements are generally ceramics. Typically these ceramics are oxides, carbides and nitrides which are used because of their excellent combinations of specific strength and stiffness at both ambient and elevated temperatures [8].

The matrix of a MMC is defined as a metal, but pure metal is rarely used: it is generally an alloy. The two most commonly used metal matrices are based on aluminum and titanium. Both of these metals have comparatively low densities and are available in a variety of alloy forms. The most common reinforcements of aluminum and its alloys are SiC and Al_2O_3. Aluminum MMCs are mainly used in bracing systems, pistons, brake discs and airframes. Titanium alloys have higher tensile strength-to-weight ratios as well as better strength retentions at 400–500°C than those of aluminum alloys and conventional materials. Titanium MMCs are used in applications where performance is demanded without regard to cost-effectiveness. Other metals were also considered as possible matrices for MMC. Magnesium is even lighter that aluminum, but it is exposed to atmospheric corrosion which makes it less suitable for many applications. Beryllium is the lightest of all structural metals and has a tensile modulus higher than that of steel. However, it is extremely brittle, which makes it unsuitable for a matrix material. Nickel- and cobalt-based super alloys have also been used as matrices, but they tend to oxidize the reinforcing fibers at elevated temperatures [9].

Copper

Another metal that is used as a matrix in MMCs is copper. It is a ductile soft metal with very high electrical (59.6×10^6 S/m) and thermal conductivities, which are the second highest among pure metals at room temperature. Copper has a high resistance to both atmospheric and aqueous corrosion, but its use as a structural material is limited because of great weight. However, some of its outstanding characteristics, such as its high electrical and heat conductivity, in many cases overbalance the weight factor. The major applications of copper are in electrical wires (65%), roofing and plumbing (25%), transport (7%) and other (3%) [10]. Copper is mostly used as a pure metal, but when a higher hardness is required it is combined with other elements to make an alloy (5% of total use) such as brass and bronze. Copper is 100% recyclable without any loss of quality, regardless of whether it is in a raw state or contained in a manufactured product.

1.2 Filler: Carbon nanotubes

At first the constituents were typically macroscopic. Since composites technology advanced over the last years the reinforcement materials constantly decreased in size. Presently there is a considerable interest in “nanocomposites” having nanometer sized reinforcements. Carbon nanotubes (CNTs) have shown a high potential as fillers because of their outstanding properties such as high stiffness, strength and tenacity, thermal and electrical conductivity, etc [1].

CNTs can be viewed as graphene sheets rolled into hollow cylinders. Nanotubes are categorized as single-walled nanotubes (SWNTs) and multi-walled nanotubes (MWNTs). SWNTs consist of a single sheet of graphene rolled seamlessly to form a cylinder with diameter of order of 1nm and length of up to centimeters [11]. MWNTs consist of several concentric cylinders with an interlayer spacing of 0.34nm [12]. The diameter of MWNTs generally ranges from 2 to 100nm [13]. The arrangement of concentric graphene cylinders in MWNTs can be described by two models. In the more common *Russian Doll* model, sheets of graphene are arranged in concentric cylinders while in the *Parchment* model, a single sheet of graphite is rolled in around itself, resembling a scroll of parchment. Individual nanotubes naturally align themselves into "ropes" held together by van der Waals forces.

1.2.1 SWNT structure

To define the one dimensional structure of a carbon nanotube we first need to look at the unit sell of 2D graphene. Figure 1.3 shows a unit sell of graphene (rhombus) which contains two carbon atoms A and B. The lattice vectors in real space $\mathbf{a_1}$ and $\mathbf{a_2}$ are given by [14]:

$$\mathbf{a_1} = \left(\frac{\sqrt{3}\,a}{2}, \frac{a}{2}\right) \text{ and } \mathbf{a_2} = \left(\frac{\sqrt{3}\,a}{2}, -\frac{a}{2}\right)$$

where $a = |\mathbf{a_1}| = |\mathbf{a_2}| = 1.42 \times \sqrt{3} = 2.46\text{Å}$ is the lattice constant of graphene.

Correspondingly, the basis vectors $\mathbf{b_1}$ and $\mathbf{b_2}$ of the reciprocal lattice are given by:

$$\mathbf{b_1} = \left(\frac{2\pi}{\sqrt{3}\,a}, \frac{2\pi}{a}\right) \text{and } \mathbf{b_2} = \left(\frac{2\pi}{\sqrt{3}\,a}, -\frac{2\pi}{a}\right)$$

The shaded hexagon in Figure 1.3 represents the Brillouin zone (BZ) of graphene. The three high symmetry points, Γ, K and M of the Brillouin zone are shown at the center, the corner, and the center of the edge, respectively.

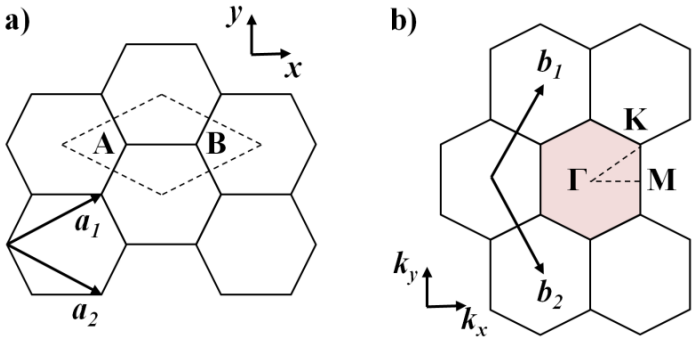

Figure 1.3. a) The unit cell (dotted rhombus) of a graphene lattice with basis vectors $\boldsymbol{a_1}$ *and* $\boldsymbol{a_2}$ *b) the Brillouin zone (shaded hexagon) of a graphene layer with* $\boldsymbol{b_1}$ *and* $\boldsymbol{b_2}$ *reciprocal lattice vectors. The high symmetry points, Γ, K and M are indicated* [14].

The nanotube structure can be described by the diameter or a chiral vector $\boldsymbol{C_h}$ defined by the following equation:

$$\boldsymbol{C_h} = n\boldsymbol{a_1} + m\boldsymbol{a_2} = (n, m)$$

where $\boldsymbol{a_1}$ and $\boldsymbol{a_2}$ are unit vectors in a two-dimensional hexagonal lattice above, and n and m are integers. If $m = 0$, the nanotubes are called zigzag nanotubes, and if $n = m$, the nanotubes are called armchair nanotubes. Otherwise, they are called chiral.

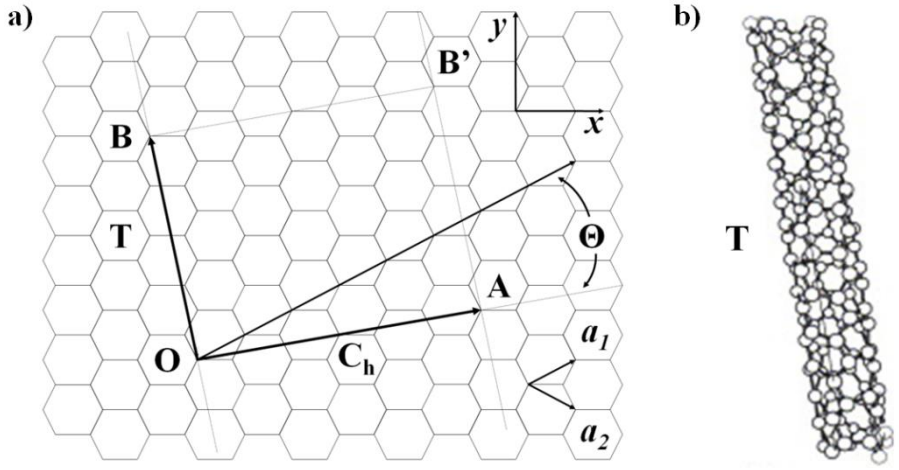

Figure 1.4. a) The unrolled honeycomb lattice of a nanotube. When we connect sites O and A, and sites B and B', a portion of a graphene sheet can be rolled seamlessly to form a SWNT. The vectors OA and OB define the chiral vector $\boldsymbol{C_h}$ *and the translational vector* $\boldsymbol{T}$ *of the nanotube, respectively. The rectangle OAB'B defines the unit cell for the nanotube. The figure is constructed for an (n, m) = (4, 2) nanotube* [15] *b) The (4, 2) SWNTs, showing the translation vector* $\boldsymbol{T}$ [14].

Mathematically, the nanotube diameter is given by:

$$d_t = \frac{a\sqrt{m^2 + n^2 + nm}}{\pi} = \frac{|\boldsymbol{C_h}|}{\pi}$$

where a is the lattice constant in the graphene sheet $(a = 2.46\text{Å} = \sqrt{3}a_{C-C}, a_{C-C} = 1.421\ \text{Å})$. The chiral angle Θ is given by:

$$\tan\Theta = \frac{\sqrt{3}m}{2n + m}$$

Thus, the structure of any nanotube can be expressed by either two indices (n, m) or equivalently by d_t and Θ.

To define the unit cell for the 1D nanotube, we define the vector OB in Figure 1.4 as the shortest repeat distance along the nanotube axis, thereby defining the translation vector $\boldsymbol{T}$:

$$\boldsymbol{T} = t_1\boldsymbol{a_1} + t_1\boldsymbol{a_1} \equiv (t_1, t_2)$$

where the coefficients t_1 and t_2 are related to (n, m) by

$$t_1 = \frac{(2m + n)}{d_R} \text{ and } t_1 = -\frac{(2m + n)}{d_R}$$

where d_R is the greatest common divisor of $(2n + m, 2m + n)$ and is given by:

$$d_R = \begin{cases} d \text{ if } n - m \text{ is not a multiple of } 3d \\ 3d \text{ if } n - m \text{ is a multiple of } 3d \end{cases}$$

where d is the greatest common divisor of (n, m).

The magnitude of the translation vector $\boldsymbol{T}$ is:

$$|\boldsymbol{T}| = T = \frac{\sqrt{3}C_h}{d_R}$$

The unit cell of the nanotube in real space is defined as the area delineated by the lattice vectors $\boldsymbol{T}$ and $\boldsymbol{C_h}$. The number of hexagons, N, contained within the 1D unit cell of a nanotube is determined by the integers (n, m) and is given by

$$N = \frac{2(m^2 + n^2 + nm)}{d_R}$$

The corresponding vectors in reciprocal space are the reciprocal lattice vectors $\boldsymbol{K_2}$ along the nanotube axis and $\boldsymbol{K_1}$ in the circumferential direction, which gives the discrete k values in the direction of the chiral vector $\boldsymbol{C_h}$. The vectors $\boldsymbol{K_1}$ and $\boldsymbol{K_2}$ satisfy the relations:

$$\boldsymbol{C_h} \cdot \boldsymbol{K_1} = 2\pi, \quad \boldsymbol{T} \cdot \boldsymbol{K_1} = 0, \quad \boldsymbol{C_h} \cdot \boldsymbol{K_2} = 0, \quad \boldsymbol{T} \cdot \boldsymbol{K_2} = 2\pi$$

This can be rewritten as

$$\boldsymbol{K_1} = \frac{1}{N}(-t_2\boldsymbol{b_1} + t_1\boldsymbol{b_2}), \quad \boldsymbol{K_2} = \frac{1}{N}(m\boldsymbol{b_1} - n\boldsymbol{b_2})$$

where $\boldsymbol{b_1}$ and $\boldsymbol{b_2}$ are the reciprocal lattice vectors of a 2D graphene sheet.

The CNT Brillouin zone is a collection of N 1D equidistant cutting lines through the k space of graphene (Figure 1.5)

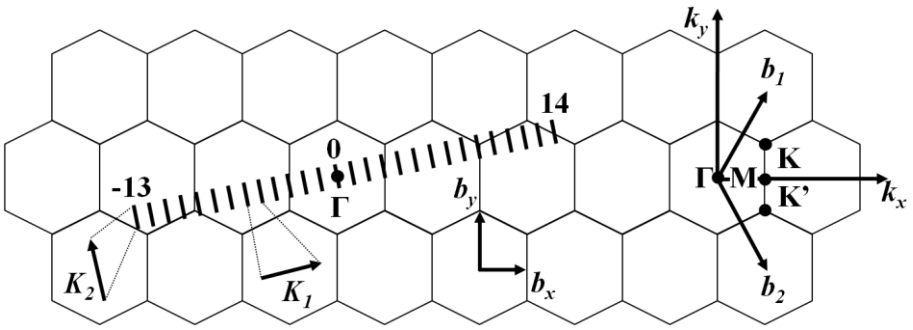

Figure 1.5. Parallel equidistant lines represent the cutting lines for the (4, 2) nanotube. The cutting lines are labeled by the cutting line index μ, which assumes integer values from 1-N/2=13 to N/2=14 [14].

For each of the μ (μ=1-N/2,..., N/2) discrete values of the circumferential wave vectors, 1D electronic energy band appears (one π-band and one π*-band), whereas each μ gives rise to 6 branches in the phonon dispersion relations.

1.2.2 Electronic structure of SWNTs

The electronic structure of SWNTs is derived from that of a single graphene, but in the case of SWNTs, the quantum confinement of the 1D electronic states must be taken into account. The electronic σ bands are responsible for the strong in-plane covalent bonds within the 2D graphene sheets, while the π bands are responsible for weak van der Waals interactions between such graphene sheets in bulk graphite. In contrast to the σ bands, the π bands are close to the Fermi level, so that electrons can be excited from the valence (π) to the conduction (π^*) band optically [14].

The electronic band structure of graphene can be obtained with the tight binding (TB) model. Within this model it is assumed that the crystal potential is strong, and the electron is captured by its own ion during the motion through the lattice, the electron remains there for a long time before tunneling to the next ion. During the capture interval, the electron stays primarily around a single ion, i.e. its state function is essentially that of an atomic orbital, uninfluenced by other atoms [16].

Figure 1.6a shows the π and π^* bands of 2D graphene in the first Brillouin zone. The optical transitions occur close to the corners of the 2D hexagonal Brillouin zone, called the K points, where the valence and conduction bands touch each other. The energy dispersion around the K point is linear in k which gives graphene and SWNTs their unique electronic properties [14].

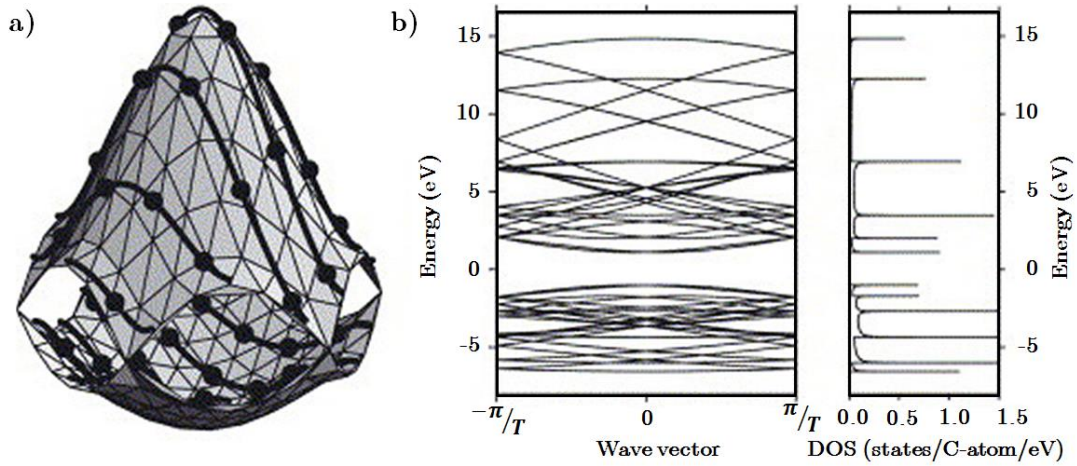

Figure 1.6. a) The calculated constant energy contours for the conduction and valence bands of a graphene layer in the first Brillouin zone using the π-band nearest neighbor tight binding model [15]. The valence and conduction bands touch in the K points. Solid curves show the cutting lines for the (4, 2) nanotube [17], as shown in Figure 1.5, but translated to the first Brillouin zone of 2D graphite, the dark points indicating the connection points
b) Electronic energy band diagram for the (4,2) nanotube obtained by zone-folding from a) c) Density of electronic states for the band diagram shown in b) [14].

To obtain the electronic band structure of the nanotube in a $E(k)$ graph, one needs to plot all the 1D cutting lines of the 2D energy surface of graphene. These cutting lines originate from wave vectors allowed by quantization around the circumference. Figure 1.6a illustrates this for a (4, 2) SWNT.

SWNTs can be classified into three different classes determined by the n and m indices. A class is defined by the reminder of $2n+m$ divided by 3 (Figure 1.7b). Both classes with reminder 1 and 2 are semiconducting nanotubes. None of the allowed k vector falls on the K point. For the class where $2n+m$ is a multiple of 3 some of the k vectors fall on the K point and these SWNTs are classified as "metallic". However, due to the curvature effect, only armchair ($n = m$) SWNTs are truly metallic, while the other MOD0 SWNTs ($n \neq m$) are metallic at room temperature, but exhibit a small ($\sim meV$) chirality-dependent energy gaps (quasi-metallic) at lower temperatures.

The density of states (DOS) of 1D materials has characteristic maxima, called van Hove singularities. It is important that the rate of optical transitions in carbon nanotubes is related primarily to the electronic states at the van Hove singularities, while the energy positions of van Hove singularities depend on the diameter and chirality of the CNT. For this reason, optical spectroscopy can be used for the structural determination of a given (n, m) carbon nanotube.

The optical transition energies E_{ii} between the electronic valence and conduction bands as a function of diameter (Kataura plot [18]) can be calculated and have been experimentally verified.

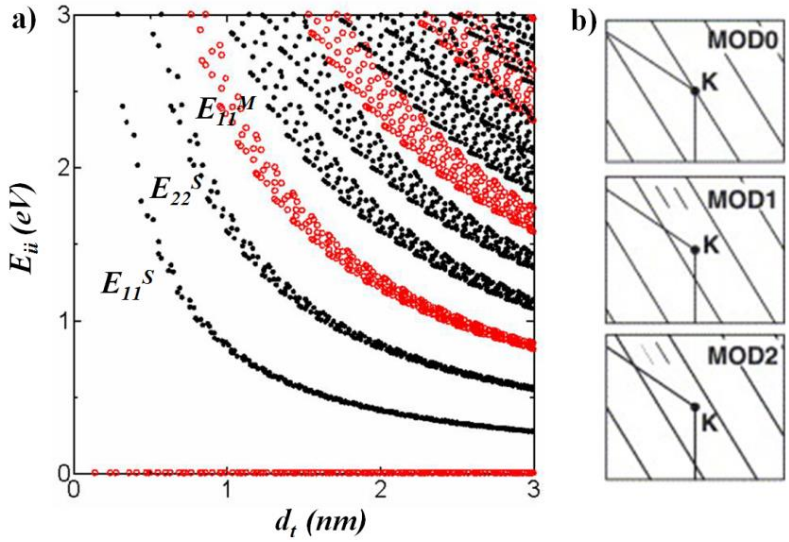

Figure 1.7. a) Electronic transition energies Eii vs. nanotube diameter d_t for SWNTs (calculated with TB method). Stars, filled and open circles stand for MOD0, MOD1 and MOD2 SWNTs, respectively. b) Schematic figure defining the SWNT classes: MOD0—metallic, where one cutting line crosses the K point; MOD1 and MOD2—semiconducting. Superscripts S or M are used to denote the electronic transition energies E_{ii}^M for metallic SWNTs and E_{ii}^S for semiconducting SWNTs [14].

Excitonic effects play an important role in photo excitation and have been observed in two photon excitation spectra [19] [20] [21].

Photolumiscence (PL) is an important tool for CNT characterization. By plotting the emission wavelength, chirality distribution in the sample can be identified [22].

1.2.3 Phonon structure of SWNTs

Phonons play a major role as carriers of thermal energy in thermal conduction processes and in thermodynamic properties, such as the heat capacity, and as an important scattering process for bringing electrons into equilibrium with the lattice.

The phonon dispersion relations and the phonon density of states for a SWNT can be derived from graphene using band folding. The 2D graphene sheet has $p = 2$ atoms per unit cell, thus having $3p = 6$ phonon branches: 3 acoustic (A) and $(3p - 3) = 3$ optic (O) (Figure 1.8a). For one acoustic branch and one optic phonon branch, the atomic vibrations are perpendicular to the graphene plane, and they correspond to the out-of-plane (o) phonon modes. For two acoustic and two optic phonon branches, the vibrations are in-plane (i). In a first approximation the displacement of the nearest neighbor atoms are considered and, the phonon modes are classified as longitudinal (L) or transverse (T) according to vibrations parallel with or perpendicular to, respectively, the bond direction. Therefore, along the high symmetry ΓM and ΓK directions, the six phonon dispersion curves are assigned to LO, iTO, oTO, LA, iTA, and oTA phonon modes (Figure 1.8b) [14].

The phonon dispersion for a (10, 10) SWNT obtained by band folding is illustrated in Figure 1.8c, and the respective phonon DOS with van Hove singularities is shown in Figure 1.8d.

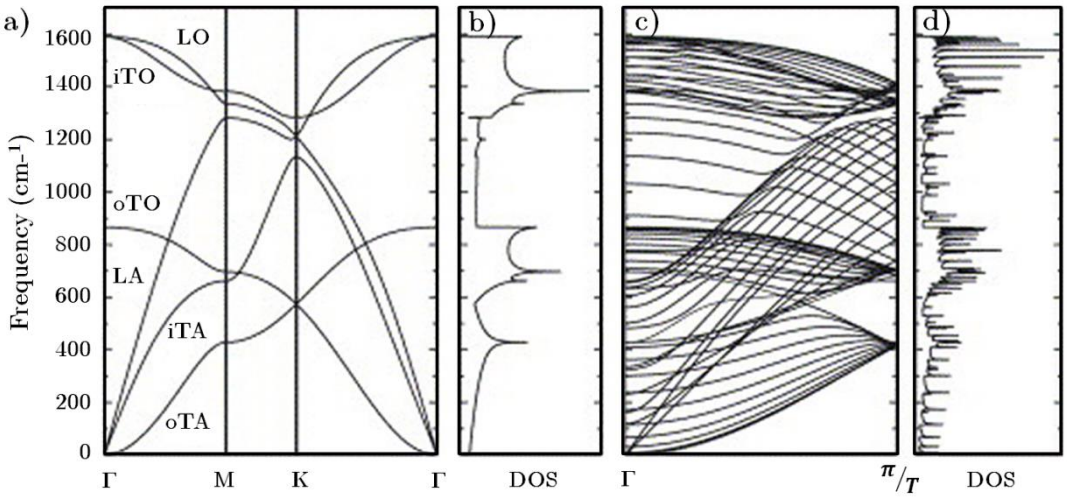

Figure 1.8. a) Phonon dispersion of 2D graphite using the force constants from [23]. *The phonon branches are labeled: out-of-plane transverse acoustic (oTA); in-plane transverse acoustic (iTA); longitudinal acoustic (LA); out-of-plane transverse optic (oTO); in-plane transverse optic (iTO); longitudinal optic (LO). b) The phonon density of states for a 2D graphene sheet. c) The calculated phonon dispersion relations of an armchair carbon nanotube with (n,m)=(10,10) d) The corresponding phonon density of states for a (10,10) nanotube* [14].

Electron phonon coupling (EPC) plays an important role in the physical properties of CNTs. Ballistic transport, excited state dynamics, and Raman spectra depend on it. In particular, the optical phonons EPC limits high field ballistic transport [24].

1.2.4 Properties

Nanotubes are light weight (density ~0.8-1.8g/cm^3 [25]) and have remarkable electrical, thermal, and mechanical properties. In 2000, Yu *et al.* measured Young's moduli values for individual MWNT of between 0.27–0.95TPa, strengths in the 11–63GPa range, and a toughness of ~1240J·g^{-1} [26]. For SWNTs, Young's moduli were found to be in the range of 0.32–1.47TPa and strengths between 10 and 52GPa with a toughness of ~770J·g^{-1} [27]. Even the most defective carbon nanotubes have strengths of several GPa [28]. Furthermore, CNTs are thermally stable. They can stand temperatures up to 500°C [29] in air and up to 2000°C in Argon atmosphere [30]. Theory predicts a room temperature thermal conductivity of up to 6000W/m·K [31]. While this has not yet been attained, thermal conductivity as high as 3000W/m·K has been measured [32].

1.2.5 Electronic transport

Diffusive conduction

Electrical resistance in metals arises because electrons propagating through the solid are scattered due to deviations from perfect translational symmetry. These are produced either by impurities (giving rise to a temperature independent contribution to the resistance) or the phonons in a solid.

The conductance of a macroscopic conductor is described by Ohm's law:

$$G = \sigma \frac{A}{l}$$

where A and l are the cross-section and length of the conductor, respectively. The conductivity σ of the sample is determined by intrinsic material parameters, first described by the Drude conductivity:

$$\sigma = \frac{ne^2}{m}\tau_m$$

where apart from the charge carrier concentration n, the only free parameter is τ_m, the characteristic momentum relaxation time of the charge carriers. The associated length scale is $l_m = v_F \tau_m$, with v_F being the Fermi velocity of the electron. This quantity determines the distance that the electron traverses between two scattering events. A conductor is in the diffusive regime if $l \gg l_m$. The charge carrier scatters several times when crossing the conductor.

Ballistic conduction

The simple Drude model is not valid for sufficiently small conductors, and inherently fails if the size of the structure becomes so small, that the electron crosses it in a timescale of τ_m. If no scattering occurs inside the conductor ($l \ll l_m$) such as for a nano-constriction, one falls in the ballistic regime. A lot of research has been carried out on electronic transport properties of 1D systems [33] [34]. In the absence of magnetic field and if one neglects the coherence effects, the conductance of a confined system, like the conductance of a nanowire (NW), is defined by the Landauer formula:

$$G = \frac{2e^2}{h} NT$$

It depends on the transmission probability T and on the number of propagating modes N, which is determined by the cross-section of the NW. Thus, assuming a ballistic transport regime, the conductance is quantized in

$$G_0 = \frac{2e^2}{h} \approx (12.9k\Omega)^{-1}$$

units when the cross-section is varied.

First the quantized conductance for MWCNTs was observed by Frank *et al.* [35] when moving a nanotube contact at constant speed into and out of the mercury contact as a function of time (Figure 1.9).

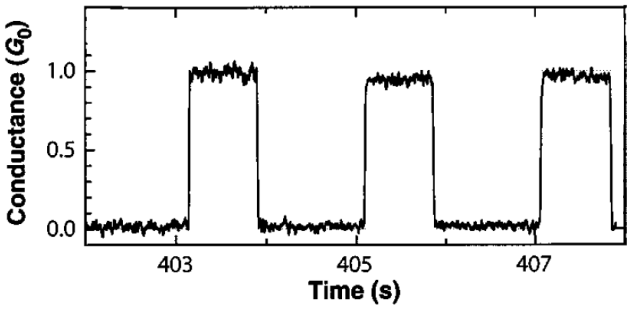

Figure 1.9. Conductance measurements. The period of motion is 2s and the displacement Δz=±2.5 mm. The conductance "jumps" to ~1G_0 and then remains constant for ~2 μm of its dipping depth. The direction of motion is then reversed and the contact is broken after 2 mm. The cycle is repeated to show its reproducibility [35].

Pristine carbon nanotubes are extremely conductive. Ballistic transport implies that Joule heating is minimized. As a result the nanotubes can carry very large current densities of up to 10^9 A/cm^2 [36]. In comparison, for superconductive materials such as MgB_2 the current density can be as high as 10^5-10^6 A/cm^2 at 4K [37]. In addition, carrier mobilities as high as 10^5 cm^2/Vs have been observed in semi-conducting nanotubes [38]. Superconductivity has also been observed in SWNTs, albeit with transition temperatures of 5K [39].

These outstanding properties make CNTs potentially ideal candidates for improvement of mechanical and electrical properties of composites.

1.2.6 Synthesis

A wide variety of synthesis techniques have been used for growing CNTs of different properties: size, aspect ratio, purity, entanglement and straightness. Currently, chemical and physical methods are used to synthesize carbon nanotubes in industrial quantities. These methods include electric arc discharge, laser ablation and chemical vapour deposition (CVD) [25].

Electric arc discharge is the first technique where CNTs have been grown. The arc discharge is run in an inert He or Ar atmosphere. In this process the carbon of the cathode sublimates through the impact of the accelerated electrons.

In laser ablation, a laser vaporizes a graphite target in a high-temperature reactor (about 1200 °C), while an inert gas is bled into the chamber. Nanotubes are obtained on the cooled surfaces of the reactor as the vaporized carbon condenses.

CVD is the most common method in which a controlled reaction of thermal decomposition of a hydrocarbon gas (methane, carbon monoxide, acetylene, ethylene or ethanol) at the sites of metal catalysts such as Ni, Fe or Co produces single and multi-wall carbon nanotubes. Interestingly the diameter of the synthesized nanotubes is related to sizes of metal particles. CVD grown tubes are cheaper, have higher purities and can be produced in large quantities, but they are more defective and their properties are much lower than the arc produced ones. Aligned arrays of tubes with controlled diameter and length can be produced with plasma-enhanced CVD (PECVD). If plasma is generated by the application of a strong electric field during growth, then the nanotube growth will follow the direction of the electric field. Aligned arrays can be rolled into carbon threads where each filament is a bundle of thousands of CNTs.

1.3 Nanocomposite CNT@Cu

One of the objectives of adding fibrous reinforcements such as CNTs to a metal matrix is to increase the tensile strength and the elastic modulus of the composite. CNTs have a higher stiffness and strength compared to the metal matrix. But CNT/metal nanocomposites have shown lower strength than expected [40], possibly because of the low interfacial bonding strength between the matrix and the CNT. Proper bonding would lead to efficient load transfer and effective utilisation of the strength of the CNTs. Carbon nanotube reinforced metallic matrix composites are not yet commercially available. However, there are several potential applications for these composites (Table 1.2). Carbon nanotubes have better strength and stiffness than carbon fibers and hence have the potential in replacing carbon fiber reinforced MMCs in various applications. Overcoming the challenges in processing will result in efficient use of the CNTs in MMCs [41].

Industry	Application	Wanted property
Automobile industry	Brake shoes, cylinder liners, piston rings, gears	High strength, wear resistance, good thermal conductivity, low density
Aerospace industry	Aircraft brakes, landing gears	Good wear resistance, good thermal conductivity, low density, high strength
Space applications	High gain antenna boom, structural radiators	Low density, high strength, low coefficient of thermal expansion, good electrical conductivity
Sports industry	Light weight bicycles, tennis and badminton rackets	High strength, high elastic modulus
Electronic packaging	Heat sinks for thermal management, solders	High thermal conductivity, low coefficient of thermal expansion, increased strength

MEMS and sensors	Micro-beams, micro-gears	High elastic modulus, high surface area
Battery and energy storage	Anodes and anode coatings, hydrogen storage materials	Large surface area, reduced response times, increased H_2 adsorption—desorption rate, high current density

Table 1.2. Potential applications of CNT-reinforced metal composites in various industries [41].

Another important objective of adding CNTs is to obtain a self-lubricating material, preventing the need for liquid lubricants. In particular CNT/Cu composites are of great interest [42] [43] [44] [45].

Different methods of fabrication such as powder metallurgy, mechanical alloying and sintering, extrusion, hot pressing and electro- and electroless deposition have been applied for synthesizing CNT-reinforced MMCs. Recently some novel methods have been designed for obtaining better dispersion of CNTs. These methods include molecular level mixing, nanoscale dispersion and spark plasma sintering which although successful, are still on a laboratory scale [41].

1.3.1 Mechanical properties

Incorporation of CNTs in copper leads to a significant improvement of mechanical properties such as microhardness, wear resistance and low friction coefficient. However, the results reported by different groups vary widely due to different experimental conditions: the type of CNTs used, the preparation routes and the testing conditions (counterface, load, distance, relative humidity). Powder metallurgy technique, comprising of compaction and sintering, helps increasing the hardness up to 20% and decreasing the wear loss by 70% with 15 vol.% MWNT addition. [42]. CNTs coated with Ni improved bonding with the Cu matrix resulting in about 80–100% increase in the hardness for 9–16 vol.% MWNT addition [46]. Spark plasma sintering of 10 vol.% MWNT/Cu composite improved the hardness by 80% [40]. The microwave sintered CNT/Cu composites exhibited up to 70% lower coefficient of friction and up to ten times lower wear rate compared to unreinforced copper on addition of 15 vol.% of copper-coated MWNTs [43]. CNT/Cu composites fabricated by molecular level mixing showed up to a 100% increased hardness and up to 70% increased wear resistance with 10 vol.% CNTs addition. The remarkable enhancement of hardness is originated from the homogeneously distributed CNTs in Cu matrix, high interfacial strength at CNT/Cu interfaces and high relative density of nanocomposites. The dispersed CNTs in Cu-matrix provide enhanced wear resistance by retarding the peeling of Cu grains during sliding wear process [45]. When using DWNTs [47], a doubling of the Vickers microhardness and a fourfold decrease of the average friction coefficient compared to pure Cu, were obtained for a 5 vol.% carbon loading. The needed volume fraction to improve the mechanical properties is significantly lower when using DWNTs. Indeed, a given DWNT weighs much less than a MWCNT of the same length [48] and therefore many more DWNTs are present for a given carbon weight loading, which can greatly modify the matrix microstructure and ultimately give better results for lower carbon loadings.

1.4 Nanocomposite CNT@PEEK

Incorporation of CNTs into a polymer results in a significant change in mechanical, electrical and thermal properties of the matrix. There are various factors that influence property modification such as processing techniques, type of CNTs, aspect ratio and CNT content. So it is very important to optimize these conditions to obtain nanocomposites with desired properties. It is generally observed that a particular processing method which is good for one property may not be good for another. One such example is surface modification of CNTs, that generally enhances the mechanical properties but deteriorates the electronic properties [49].

A number of studies has been devoted to the evaluation of the mechanical, electrical and thermal properties of CNT/polymer nanocomposite obtained under different conditions and filler loadings.

Polymer/CNT composites can be fabricated by several methods including solution mixing, sonication, melt compounding and in-situ polymerization [50] [51]. The melt blending process was reported to be the most suitable for the integration of CNTs into the PEEK matrix. This approach presents two main advantages: firstly, it is environmentally sound, due to the absence of organic solvents; secondly, it is compatible with conventional industrial processes, such as extrusion, injection and blow molding [52].

Properties

Thermal stability

The thermal stability of nanocomposites is a key parameter for their technological applications. It can be evaluated by thermo-gravimetric analysis (TGA). The incorporation of SWCNTs into PEEK was reported [53] to shift the matrix curve towards higher temperatures which means that the resulting composite is more thermally stable than the initial polymer.

Wang *et al.* [54] also observed an improved thermal stability on the incorporation of MWCNTs wrapped with poly (ether sulfone) (PES). Which was attributed to the restriction of the thermal motion of PEEK chains making the composites more thermally stable.

However, the thermal stability of PEEK composites did not show a significant improvement with increasing the content of wrapped in PES MWCNTs in PEEK, while the incorporation of increasing SWCNT loading progressively enhanced the stability of the matrix. The observed stabilization was attributed to the above mentioned barrier effect of CNTs, combined with the higher thermal conductivity of the composite that facilitates heat dissipation [53].

The type of CNTs and the preparation procedure affect the decomposition process. Samples prepared with mechano-chemical pre-treatments present higher thermal stability than those obtained by direct mixing; a more uniform and fine dispersion of the CNTs improves the interfacial adhesion between the nanotubes and the matrix and restricts the thermal motion of the PEEK chains, leading to composites thermally more stable. Well dispersed nanotubes hinder the diffusion of the degradation products from the bulk of the polymer to the gas phase and thereby delay the degradation temperatures [53].

Crystallization and melting behavior

The dynamic crystallization of composites is of great interest, because it influences the physical properties. Generally, the crystallization and melting behaviour of CNT/polymer nanocomposites is analyzed by differential scanning calorimetry (DSC). The basic principle underlying this technique is that when the sample undergoes a physical transformation such as phase transitions, more or less heat will need to flow to it than to the reference sample to maintain both at the same temperature. The transition temperatures are taken as the peak maximum or minimum in the calorimetric curves.

Diez-Pascual observed a decrease in the crystallization temperature (T_c) with the incorporation of SWNTs in PEEK, whereas they did not significantly modify the level of crystallinity of the composite [53]. These observations were attributed to the fact that nanotubes reduced the crystallization rate of the PEEK matrix, and were explained by a nanoconfinement effect [55]: the CNT network imposes a confinement on polymer chain diffusion and crystal growth which slows down the overall crystallization process, leading to lower values of T_c, for the composites. On the other hand, samples with improved degree of dispersion of the SWCNTs presented slightly higher T_c. The existence of small agglomerates was assumed to make the confinement effect more important and, consequently, decrease the crystallization temperatures [53].

This behavior differs from that found by Rong *et al.* [56] who observed a shift of crystallization peaks (T_c) to higher temperature with the incorporation of MWCNTs in a PEEK matrix. They assumed that CNTs increased the amount of nuclei crystallizing per unit volume of the PEEK matrix and rarely blocked the PEEK chains mobility due to weak interaction, thus accelerating the nucleation process on PEEK crystallization at low content.

Both authors observed a decrease in T_c with increasing the filler content, due to CNT agglomeration and, consequently, intensification of the restrictions on the crystal growth. In general, differences between the levels of crystallinity of the composites are quite small, lower than 5%.

In the case of the melting process, the addition of SWCNTs did not significantly change the melting temperature T_m [53], while the incorporation of MWNTs caused a little shift to high temperature compared with pure PEEK [56].

Mechanical Properties

The mechanical properties of polymer composites are usually studied by Dynamic Mechanical Analysis (DMA). A sinusoidal stress is applied and the strain in the material is measured allowing one to determine the complex modulus. The temperature of the sample or the frequency of the stress is varied, leading to variations in the complex modulus. This approach can be used to locate the glass transition temperature of the material, as well as to identify transitions corresponding to other molecular motions. The most important parameters obtained from these experiments are the storage modulus E', which gives an idea of stiffness behavior and load bearing capability of the sample and the loss modulus E", which is proportional to the amount of energy dissipated as heat as well as the ratio of the loss to storage modulus $\tan(\delta)$, related to the degree of molecular mobility in the polymeric material. The glass transition temperature (T_g) can be defined as the peak maximum in the loss modulus or loss tangent curve.

Diez-Pascual *et al.* conducted the temperature dependent measurements of the storage E' and loss E'' moduli for different 1wt% SWNT/PEEK nanocomposites at 1Hz [53]. They observed a progressive decrease in E' with increasing temperature, showing a very strong decay in the temperature range between 138-170°C, which correlates with the glass transition of the material. This drop in the modulus is attributed to an energy dissipation phenomenon involving cooperative motions of the polymer chains [57]. The incorporation of SWNTs induces a remarkable increase in the storage modulus of the matrix at temperatures below the glass transition, which becomes insignificant at higher temperatures. Experimental data reveal a non-linear growth of E' with CNT content, the increase being more pronounced at low concentrations. At very low concentrations, the nanotubes are well dispersed and E' increases rapidly with increasing SWNT content. However, when the concentration gets higher, the nanotubes interact and form small aggregates.

The aforementioned results are in contrast to the study of vapour-grown carbon nanofibres/PEEK composites [58] prepared by injection molding, which revealed a linear increase in stiffness with increasing nanofibre loading. This contradiction can be explained based on the large aspect ratio, high mass density and low flexibility of carbon nanofibers compared to CNTs [59] and on the processing employed that play a key role in the resulting properties of these materials.

The value of the loss modulus of PEEK as a function of temperature exhibits a low broad peak (at around -95°C), attributed to the β relaxation associated with local motions of the ketone groups, and an intense sharp peak (at 148.3°C), denominated the α relaxation whose maximum corresponds to the glass transition temperature (T_g) of the polymer. The addition of SWNTs results in a reduction of the magnitude of E'' at temperatures below T_g. Furthermore, the β relaxation was broadened, smoothed and shifted to higher temperatures. This suggests that SWNTs act as a barrier for the local movements of the ketone groups. Moreover, the CNTs restrict rotational motion within the polymer chains, causing small increases in T_g, hence in the stiffness of these systems.

Deng *et al.* [60] investigated the tensile properties of PEEK/MWNTs, and found increases in the storage modulus with increasing MWNTs loading fraction at both below and above the glass transition temperature; at 25°C, the tensile modulus increased by ~90% for composites including 15wt% MWNTs, and the increment reached ~160% at 200°C. According to those results, the improvement of MWNTs in the mechanical behavior of the matrix is more effective at higher temperatures.

The processing routes and the type of CNTs have a strong influence on the mechanical response of the composites. Samples with higher purity, quality and aspect ratio have higher E'. Composites with a more homogeneous distribution of nanotubes, exhibit higher E' and T_g. Experimental results do confirm that the overall mechanical performance of CNT/PEEK nanocomposites is well above the required for potential aircraft applications [53].

1.4.1 Conductivity

The incorporation of carbon nanotubes into polymer composites can be used in the electronic and aerospace industries to dissipate heat, shield electromagnetic radiation [61] and prevent the build-up of static charge [62]. The conductivity in the composites results from the formation of a continuous conductive path of CNTs in the polymer matrix at the percolation threshold.

Percolation theory

The term percolation was introduced by Broadbent and Hammersley [63] in 1957 to understand the permeation of a gas in a porous medium. The percolation theory deals with statistical properties of disordered sets of objects (links or sites) arranged on a regular lattice (between two nodes for links, nodes for sites). The transport properties of these systems arise from their geometrical and morphological properties.

Percolation on a network

Following the percolation theory [64], the probability of occurrence of a percolation network is null when the proportion of conductive sites p is below a critical threshold p_c. Consequently, the conductivity of the network is zero for $p < p_c$. On the contrary, when the proportion of conducting sites is larger than pc the conductive particles form a percolating network through the insulating network (Figure 1.10).

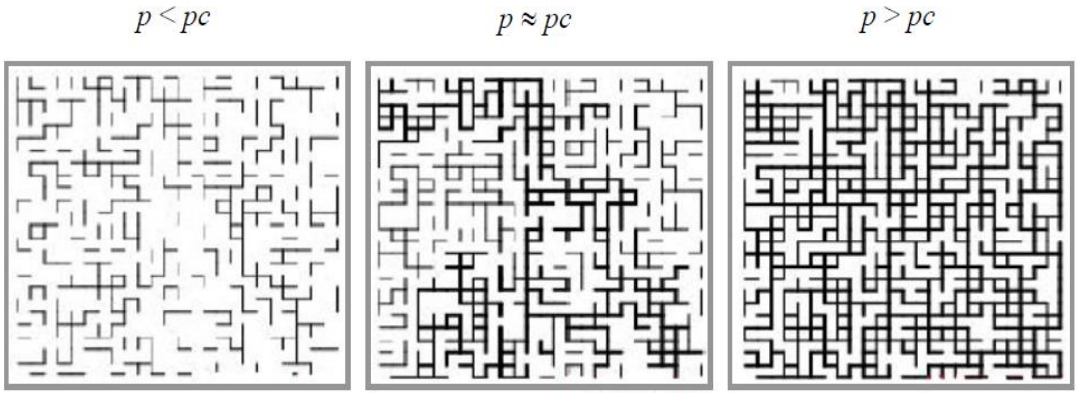

Figure 1.10. Schematic representation of the percolation on a square lattice of links, depending on the fraction p. The "backbone" is shown in bold.

The electrical conductivity σ and the probability P of a site to belong to the infinite network increase with the concentration p (Figure 1.11), but two quantities σ and P are not proportional. When all sites are conductive $p = 1$, the probability of belonging to the percolation network is certain for each site: $P(p) = 1$. The dotted curve represents the schematic evolution of the probability of a site to belong to the percolation network. The slope of the conductivity is zero at the threshold p_c while the slope of the probability of belonging to the percolation cluster is infinite.

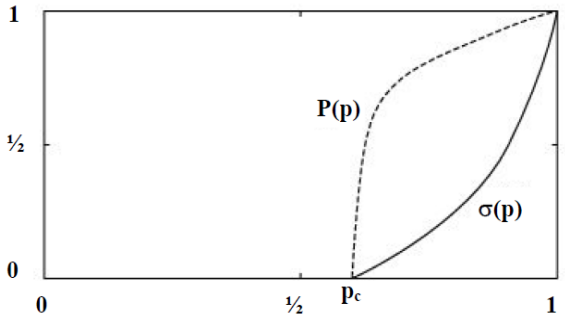

Figure 1.11. The probability P of belonging to the infinite cluster and electrical conductivity σ depending on the content of conductive particles p.

This discrepancy is explained by the diversity of links that make up the network. Many links do not carry any current, because they go nowhere and are called "dead ends" of the grid (Figure 1.12).

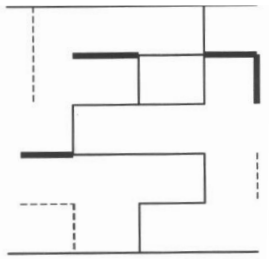

Figure 1.12. Schematic representation of a percolating network: infinite cluster (solid lines), dead ends (bold) and isolated clusters (dotted lines).

The "dead ends" are portions of clusters that are connected to the whole network by a single link. When we erase all the "dead ends", we are left with the "backbone" – the links involved in the conduction of current. This structure corresponds to the geometric skeleton of the percolation network. Deleting a link located on a loop of the geometric skeleton decreases the amount of current passing through the network.

Critical exponents of the percolation

If we consider an infinite network of resistors, the electrical conductivity in the vicinity, but above the percolation threshold $(p > p_c)$ follows the power law:

$$\sigma \propto (p - p_c)^t$$

where t is the critical exponent associated with transport properties depending on network dimension.

According to the assumption of the finite size scaling, the dependence of the electrical conductivity on the sample size is assumed to evolve as [64]:

$$\sigma(L, \xi) \propto \begin{cases} \xi^{-\frac{t}{\nu}}, & L \gg \xi \\ L^{-\frac{t}{\nu}}, & L \ll \xi \end{cases}$$

where L is the network finite size and ξ is the correlation length (average distance between two sites in the same finite cluster) following a power law:

$$\xi \propto (p - p_c)^{-\nu}$$

where ν is a universal exponent whose value is 1, 4/3 and 0.89 in 1, 2 and 3 dimensions, respectively.

For a sufficiently large network size (larger than the correlation length), the electrical conductivity σ is independent on the size of the network and can then be described by the equation:

$$\sigma \propto (p - p_c)^t$$

To verify the above relations, numerical simulations were performed according to the Monte-Carlo method [64]. Initially, networks containing a random mixture of conducting or insulating sites (or links) were simulated numerically. Secondly, the

electrical conductivity σ of each obtained network was measured. Figure 1.13 shows the results of numerical simulations at the percolation threshold [64].

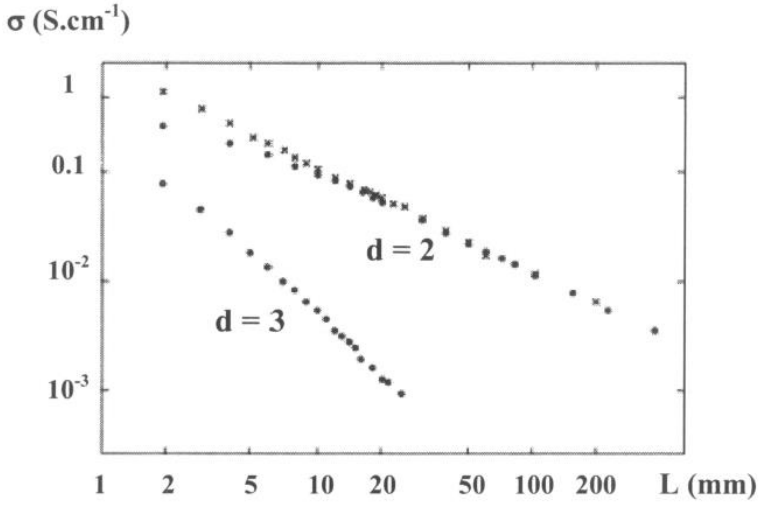

Figure 1.13. Variation of the conductivity σ with the network size L in three and two dimensions right at the percolation threshold. The two data sets for two dimensions refer to different geometries [64].

The electrical conductivity σ of two and three dimensional networks (d=2 and 3, respectively) is represented as a function of their sizes L. These results confirm the power-law dependences of σ on L. According to the literature [64] and [65] the critical exponent t is independent of material and has a theoretical value t~1.6–2.0 for three dimensional, and 1.0–1.3 for two dimensional systems.

Several experimental investigations were in good agreement with the equation for the electrical percolation, but critical exponent t is not universal in many practical systems. For tunneling percolation systems, t becomes material dependent and can be significantly different from 2 [66] because of the specific distributions of both conducting and non-conducting phases.

Dynamic percolation

Processing conditions – especially time and temperature – can strongly alter the percolation threshold and conductivity values of composite [67] [68]. This phenomenon results from the ability of the fillers to "self-assemble" [68] in the molten matrix or in thermosets before curing [69], and is known in the literature as "dynamic percolation".

Combessis *et al.* [67] reported a case of a very low density polypropylene composite. With annealing time the electrical conductivity σ of the composite gradually raised, while the effective percolation threshold p_c dropped (Figure 1.14).

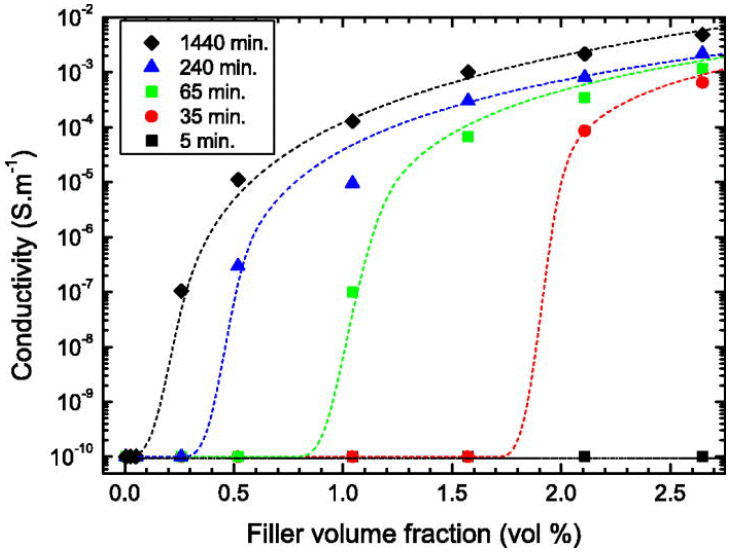

Figure 1.14. Conductivity versus amount of filler to reveal the percolation transition after each annealing step (5, 35, 65, 240, 1440 min). The critical filler fraction ("percolation threshold") is reduced by a factor of at least ten, while the electrical conductivity gained more than seven orders of magnitude [67].

The increase in conductivity has been associated to a filler re-organization in the melt, and the formation and growth of a percolating network.

The self-organization was observed to induce a divergence of the critical exponent t. The t value has been found generally higher than the universal value 2, particularly for systems showing low p_c. Values departing from the expected universal value of 2 were proposed to be an indicator of the degree of completion of the organization process (Figure 1.15) [67].

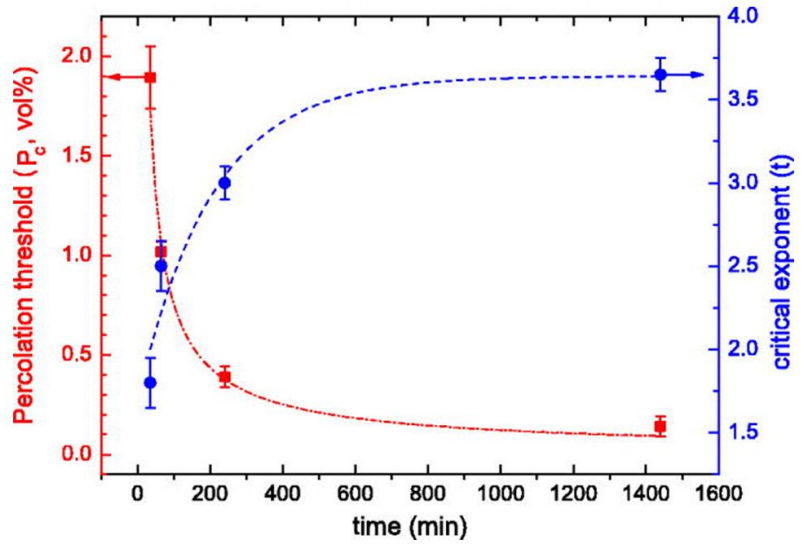

Figure 1.15. Changes in percolation threshold (■) and critical exponent (●) as a function of the annealing time at 200°C [67].

The dynamic percolation may be viewed of as a transition from a metastable system obtained by shear mixing to a thermodynamically more stable one, in which the internal stresses or the overall free energy are reduced.

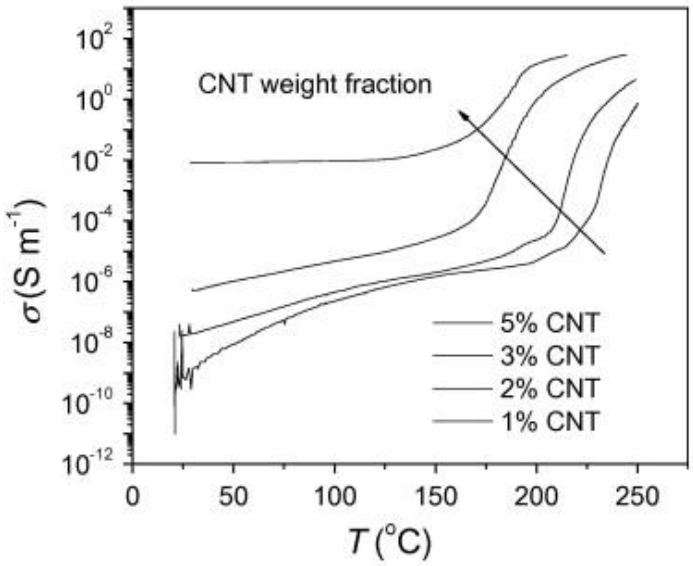

Figure 1.16. Logarithmic plot of conductivity versus temperature of CNT composite with different CNT loadings. A transition point is shown in each curve [68].

Zhang *et al.* [68] observed CNTs in a thermoplastic polyurethane matrix during annealing. The temperature at which the dynamical percolation takes place in melt has been found dependent on the concentration of CNTs (Figure 1.16).

Although high shear flow is essential for the dispersion of CNTs in the composite, the composite melt should be given enough time under low shear flow to develop its conductive network. This shows the complexity of the fabrication of a nanocomposite.

Electrical conductivity of CNT/PEEK composites

Pure PEEK is an insulating polymer (σ~10^{-15}-10^{-13} S/cm [70]), and becomes electrically conductive with the incorporation of CNTs. With increasing concentration of CNTs, number of CNT contacts increases and insulating PEEK film thickness between adjacent CNTs decreases which results in higher electrical conductivity. As the amount of CNT increases and reaches the percolation threshold the electrical conductivity increases rapidly and can be described by an above mentioned classical percolation equation:

$$\sigma = \sigma_0 (p - p_c)^t$$

where σ_0 is the conductivity scale factor related to the intrinsic conductivity of the filler, p is the concentration of conductive filler, p_c is the percolation threshold and t is the critical exponent reflecting the system dimensionality of the composite [70]. Figure 1.17 illustrates the transition from an insulating into a semiconducting or a conducting material.

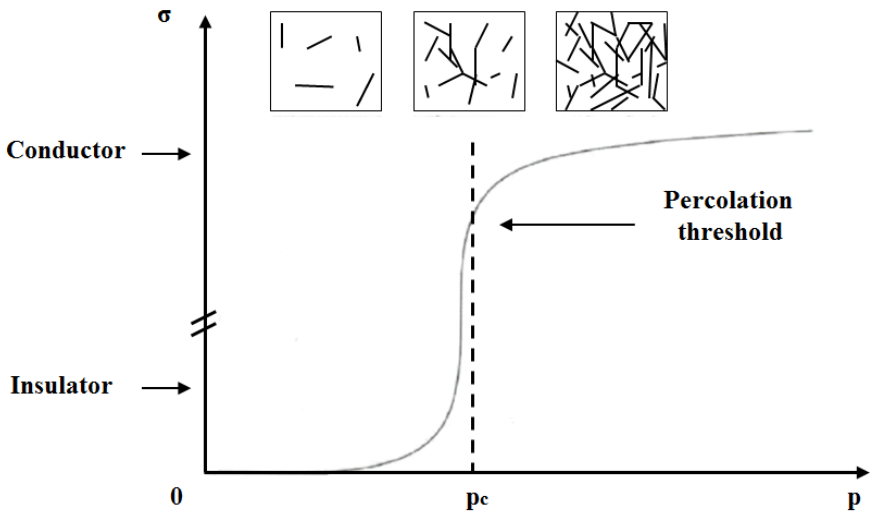

Figure 1.17. A schematic picture of the percolation phenomenon [71].

According to the percolation theory, for a random distribution of CNTs with atypical aspect ratio $\eta = 1000$, the excluded volume concept gives a statistical percolation threshold $p_c \sim 0.7/\eta \sim 0.07\text{wt\%}$ [72]. Percolation thresholds significantly lower than this value are attributed to dynamic percolation [73], which allows for particle movement and reaggregation.

In the literature it has been reported that percolation threshold lies in a wide range of weight percentage of CNTs, depending on the type of polymer of both thermosetting [74] and thermoplastics [75], processing technique and the type of CNT used. Bauhofer and Kovacs [72] summarized the published data based on many parameters like CNT type, synthesis method, treatment, dimensionality, polymer type, dispersion methods etc. They reported a wide range of percolation threshold from 0.002 to 12wt% of CNT. Thermoplastic systems usually percolate at around 1–5wt% [49].

For SWNTs/PEEK composites Diez-Pascual *et al.* [76] observed a low percolation threshold (less than 0.1wt%) and the electrical conductivity at room temperature of 10^{-2} S·cm^{-1} at 1wt% of nanotube loading.

The percolation threshold of double wall carbon nanotube (DWNTs)/PEEK nanocomposites was reported to be at 0.25wt% for composites prepared with a twin screw extruder (Figure 1.18a) [77]. The room temperature maximum conductivity σ_{max} of the composite at 2wt% of DWNTs was about 3×10^{-2} S·cm^{-1}.

For MWNTs/PEEK composites fabricated using melt blending Bangarusampath *et al.* [49] observed a percolation at 1.3wt% with a conductivity of 10^{-2} S·cm^{-1} for 2wt% of MWNTs (Figure 1.18b). The conductivity value of 1 S·cm^{-1}, required for the electrostatic applications, has been achieved at 17wt% loading.

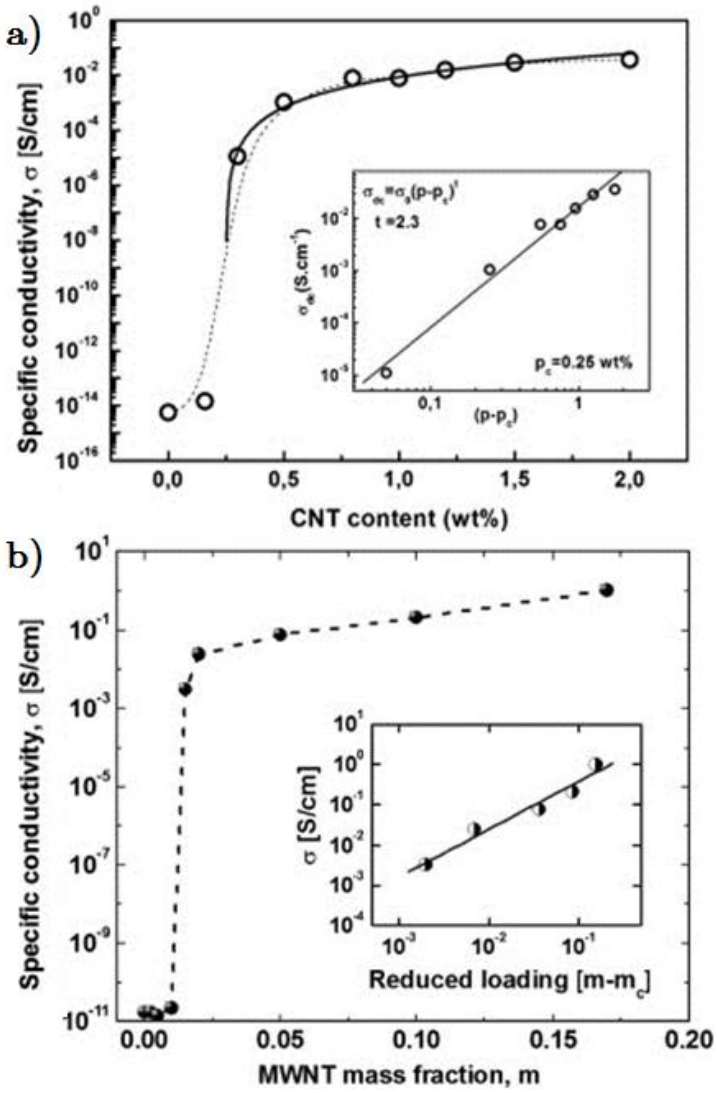

Figure 1.18. Electrical conductivity of the a) DWNTs/PEEK [77]
b) MWNTs/PEEK [49] composites as a function of CNTs weight fraction.

This value is comparatively lower than that reported by Mohiuddin [70] who measured an experimental value of the percolation threshold at 3.5wt% for MWNT/PEEK composites prepared by shear mixing. This higher percolation threshold could be attributed to the fact that CNT aggregates were not properly disentangled. Breakage of CNTs could be another reason for such high percolation threshold in this material system. A decrease in conductivity was found at higher loading of CNTs (more than 10wt%), which is an indication of formation of CNT agglomerates [70]. Since high conductivity values require a good CNT dispersion many attempts have been devoted to obtain a better dispersion of CNTs. Progress has been achieved in the dispersion of the SWNTs in the PEEK matrix by using polyetherimide (PEI) [78] and polysulfones [76]. However, functionalisation has the effect that the thermal and electrical properties are lower compared to the raw SWNTs/PEEK composites [53] and [76]. The wrapping or functionalisation of the SWNTs increases the tube–tube electrical resistance.

Charge transport mechanism

To understand the charge transport mechanism in the nanocomposites, the temperature dependence of electrical conductivity in 8wt%, 9wt% and 10wt% CNT/PEEK samples was investigated by Mohiuddin *et al.* [70]. The electrical conductivity of the composites increases during the heating process over a temperature range from room temperature to 140°C which is below the glass transition temperature of the matrix (143°C) (Figure 1.19).

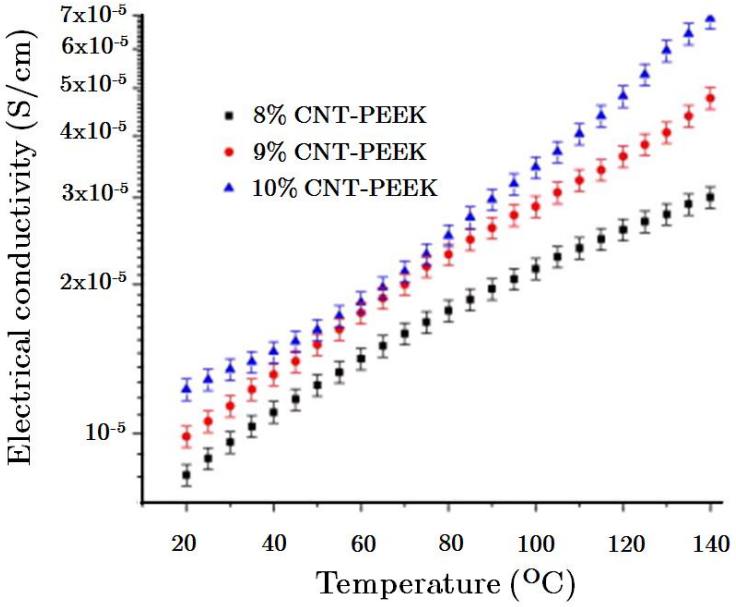

Figure 1.19. Electrical conductivity of samples with 8–10wt% of CNTs at different temperatures [70].

The trend of electrical conductivity is concave downward for 8wt% CNT/PEEK while those 10wt% CNTs are concave upward with the increasing temperature. This phenomenon was attributed to the complex combination of the effect of temperature and the effect of increasing number of CNT contacts.

In the case of 8wt% of CNTs dominates the tunneling mechanism of electrons. The electrons tend to jump from nanotube to nanotube across the gap made of polymeric material. Increasing the temperature reduces the modulus (stiffness) of the polymer and correspondingly enlarges the tunneling gap, which makes the jumping of the electrons more difficult. For composites with 10wt% of CNTs the amount of CNTs is large and there are significant numbers of contacts between the CNTs, and the polymeric gap is smaller. When the number of electrical contacts is sufficiently large, the conduction by electronic movement is dominant. With increase in temperature, the electron mobility increases which leads to a higher electrical conductivity [70]. The curve of a 9wt% CNT composite is straight indicating that the effects of reducing polymer stiffness (thus enlarging the gap and reducing conductivity) and increasing electronic movement in the CNTs balance out over the temperature range.

Thermal conductivity of CNT/PEEK composites

In contrast to the electrical conductivity, the thermal conductivity of PEEK increases linearly with CCVD MWNT loading fraction, and no percolation effects are observed. The pure PEEK thermal conductivity of ~0.3 W/m·K more than doubles to 0.7 W/m·K at 17wt% of MWNTs (Figure 1.20) [49].

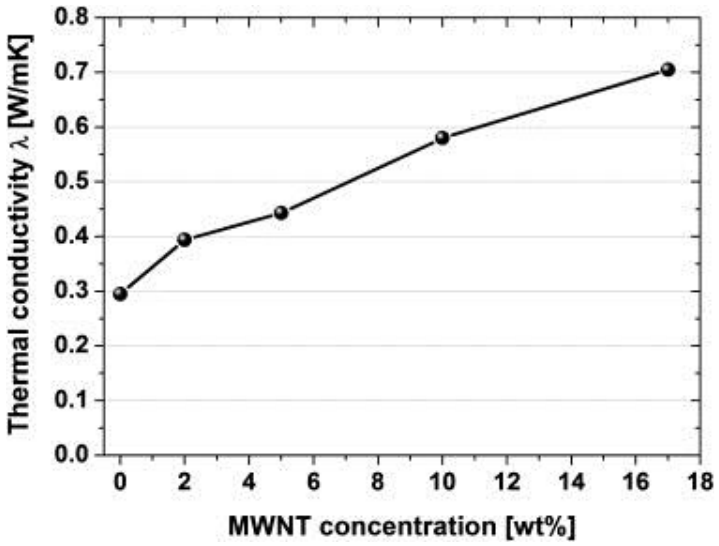

Figure 1.20. Thermal conductivity of PEEK nanocomposite as a function of MWNT concentration [49].

The absence of a percolation effect is explained by a much smaller intrinsic difference between the filler and matrix property values [79]. Even the ideal axial thermal conductivity of MWNTs (3000 W/m·K) [32] is only a factor of 10^4 greater than that of the matrix, whereas a critical ratio of 10^5 has been suggested for the emergence of percolation phenomena [79]. Below this value, rule-of-mixtures approaches are more appropriate.

For composites including 0.1, 0.5 and 1wt% laser-grown SWCNTs (thermal conductivity ~10^3 W/m·K) Diez-Pascual also observed, an almost linear increment of thermal conductivity of about 40, 115 and 150wt%, respectively [80]. It is also noted that the thermal conductivity is sensitive to the attributes of the filler, presence of defects and content in metal impurities. Compatibilized samples display slightly lower thermal conductivity, since the wrapping hinders the direct contact among the tubes [76].

1.5 Challenges of dispersion and quantification

As shown above a homogeneous distribution of CNTs in a composite is essential, since it is responsible for homogeneous properties of the composite. But nano-scale dimensions, large aspect ratios and high flexibilities of CNT turn dispersion into a challenge. Nanotubes are agglomerated together with a van der Waals binding energy of ~500eV per micrometer of tube-tube contact [81]. The most common technique to separate CNTs is dispersing them in a liquid media [82]. At the beginning solutions of CNTs in water were sonicated to suspend them temporally, but the level of dispersion

was not satisfactory. Surfactants can be added to the water allowing to individualize the CNTs. Fluorescence was used to observe the state of CNT dispersion in aqueous sodium dodecyl sulfate (SDS) surfactant [83]. Semi-conducting SWNTs fluoresce, while CNT bundles quench the fluorescence due to metallic tubes.

Alternatively, nanotubes can be dispersed subsequent to chemical treatment such as functionalization [84] [85] or by protonation with superacids [86], but these techniques tend to alter CNT properties such as electronic structure [87].

Many applications require pure solvents. A significant improvement would be to disperse pristine nanotubes in common solvents without the aid of a third dispersant phase. Selecting a surface tension of the solvent close to the sp^2 carbon could lead to good dispersions (Figure 1.21) [87]. Different solvents were tested and the quality of dispersion was evaluated by atomic force microscopy (AFM) and photoluminescence (PL) spectra. N-Methyl-2-pyrrolidone (NMP) was found to be a good solvent to suspend CNTs [87].

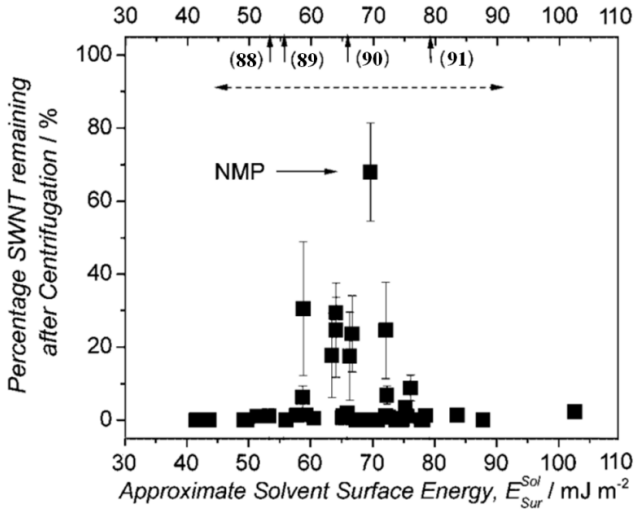

Figure 1.21. Fraction of nanotubes remaining after centrifuging dispersions (concentration = 0.1mg·mL^{-1}) made in a range of solvents as a function of solvent, surface tension (bottom axis). The best 12 solvents were measured 5 times and the mean and standard deviation plotted. The top axis shows the approximate solvent surface energy. The horizontal arrow shows the approximate range of measurements of nanotube and graphite surface energy reported in the literature. The vertical arrows indicate four typical literature values [88] [89] [90] [91] [87].

Since CNTs do not disperse spontaneously, sonication is always required. In our CNT deposition experiments, we use NMP as a solvent. We have carried out several tests and found that the optimal sonication temperature is close to 50°C.

When fabricating a composite the CNT large aspect ratio causes extremely high viscosity in the melt or dissolved polymers, which in turn affects their uniform dispersion [80]. In composite materials nanotubes have a strong tendency to gather together and form micron-sized agglomerates, which adversely affects the mechanical properties of the nano-composites. Carbon nanotubes assembled in ropes were shown to act as crack-initiators and decreased composite elastic properties [92]. Thereby different techniques have been employed to improve the CNT dispersion in matrices (nanotubes have been purified, ball milled, functionalized, surface treated with plasma and

dispersed in compatibilizing agents) [76] [78]. Inhomogeneous mixtures were found to be far more common phenomenon in SWNT reinforced composites rather than MWNT [92].

Besides the difficulty in obtaining stable and homogeneous dispersions of nanotubes, another complication is finding an efficient method to evaluate and quantify their state of dispersion. A complete characterization at nano(micro)-scopic and macroscopic scales is fundamental to obtain information about the changes induced in the polymer with the addition of CNTs. There are only a few such methods reported [41]. Agglomerates of carbon nanotubes can be visualized directly or, alternatively, a mechanical or an electric response of CNT-based materials could indirectly indicate the state of filler dispersion. Observation of CNT-based samples by optical microscopy enables to access mainly hundred micrometer-sized agglomerates. While imaging of CNT-based polymeric composites by scanning or transmission electron microscopy (SEM and TEM, respectively) gives an access to the nanometer scale. But these methods often require pre-treatments by means of gold or carbon sputtering or microtome slicing of the sample, which is sometimes complicated and might cause a defect in the original pattern of the composite [92].

However, there has been hardly any study in the quantification of dispersion in carbon nanotube composites. The majority of the researchers mention uniform CNT dispersion in the composites which is based on visual examination of the microstructure. Quantification of the degree or quality of CNT reinforcement is important since it helps in comparing various microstructures and the effectiveness of various methods for dispersion of CNTs in composites.

Luo and Koo [93] proposed a method based on the statistical distribution of horizontal and vertical separation distances between the peripheries of the particles/carbon fibers in a cross-sectional image of the composite. A log-normal distribution was found to fit the distribution obtained. Two parameters, $D_{0.1}$ and $D_{0.2}$, were defined representing the probability that the values lied between $\mu \pm 0.1\mu$ and $\mu \pm 0.2\mu$ of the values, respectively, μ being the average distance. The larger the values of $D_{0.1}$ and $D_{0.2}$ the better the distribution, since it meant uniform separation of the filler materials.

Pegel *et al.* [94] used spatial statistics on TEM images of polymer CNT composites to study the variation of the area fraction of CNTs as a function of radius of the nanotubes. They showed that the variation of the area and spherical contact distribution function converged to 100% faster in case of clustered CNT configurations.

Bakshi's group [41] suggested quantifying the spatial distribution of CNTs in nanocomposites using binary images of CNT distribution obtained from actual SEM images. Two parameters were proposed which are complimentary. The first one called Dispersion Parameter (DP) is based on the image analysis technique and is obtained based on the size of CNT cluster while the second one, named the Clustering Parameter (CP) is based on distances between centers of the nanotubes obtained by Delaunay triangulation.

Recently, Tishkova *et al.* [77] proposed to use Raman spectroscopy to access the dispersion state of DWNTs in a PEEK polymer matrix. Several Raman maps at different scales and different regions were carried out. The interaction of the outer tube with the matrix was determined from the line shape of the Raman G band. This allowed the author to distinguish regions where the nanotubes were well dispersed and regions where the nanotubes were agglomerated. This method will be discussed in more detail in the next chapter.

Chapter 2

Experimental methods

2.1 Raman spectroscopy

2.1.1 Fundamentals of Raman spectroscopy

Raman scattering is the inelastic scattering of the incident electromagnetic radiation from materials. In most cases scattering from phonons are studied, and hence the Raman frequencies that are specific to each material and depend on the structure and composition. Thus, Raman spectroscopy is highly selective, which allows to identify and differentiate molecules and chemical species that are very similar.

From the classical point of view when a molecule interacts with an incident electromagnetic field $\boldsymbol{E} = E_0 cos(2\pi\nu_0 t)$, a dipole moment $\mu_{\boldsymbol{ind}}$ is induced in the molecule:

$$\mu_{\boldsymbol{ind}} = \alpha \boldsymbol{E} = \alpha E_0 cos(2\pi\nu_0 t)$$

where ν_o is the frequency of the electromagnetic field and α is a polarizability of the molecule. The polarizability of the molecule α, is a function of displacement q. Using the small amplitude approximation, the polarizability can be described as a linear function of displacement,

$$\alpha = \alpha_0 + q \left(\frac{\partial \alpha}{\partial t}\right)_{q=0} + \cdots$$

which, when combined with the previous equation, results in

$$\mu_{\boldsymbol{ind}} = \alpha E_0 cos(2\pi\nu_0 t) + q_0 \cos(2\pi\nu t) E_0 \cos(2\pi\nu_0 t) \left(\frac{\partial \alpha}{\partial t}\right)_{q=0}$$

We can see that there are two resultant effects from the interaction of the molecule with the incident light. The first term is called Rayleigh scattering, which is the

dominate effect and results in no change in the frequency of the incident light. The second term is the Raman scattered component that can be rewritten as:

$$q_0 E_0 \left(\frac{\partial \alpha}{\partial t}\right)_{q=0} [cos(2\pi \{\nu_0 - \nu\}t) + \cos(2\pi\{\nu_0 + \nu\}t)]$$

Two frequencies that were not present in the incident light appear in the scattered light. The new components can be calculated as the frequency of the incident light plus or minus the frequency of the molecular vibration. The increase in frequency is known as an Anti-Stokes shift and the decrease in frequency is known as a Stokes shift. By measuring the change in frequency of the incident light one can derive the vibrational frequency of a molecule. The Stokes scattering, which involves loss of energy, is observed to give a stronger signal than the anti-Stokes scattering. This is in disagreement with the classical equation (which predicts equal intensities for both processes) and is the most obvious indication of the breakdown of the classical picture. The quantum-mechanical theory of Raman scattering solves this problem.

From the quantum physical point of view, the molecular vibrations are pseudo-particles (phonons) with an energy and a wavevector. The scattering process is regarded as the creation and annihilation of phonons by photons. For a population of molecules, a given fraction will be in each vibrational state, as determined by the Boltzmann distribution function, with the ground vibrational state heavily favored at low or moderate temperatures. This interpretation leads to the fact that a photon is much more likely to create a phonon than to destroy it, since the probability of annihilation of a vibrational quantum depends on the probability of finding the system in an excited vibrational state which is zero at zero Kelvin. At high temperatures and low frequencies, creation and annihilation have similar probabilities.

When using a quantum physical picture, the intensity of Raman scattering I is proportional to the squared polarizability in the reciprocal space χ [95]. For the Stokes part, it corresponds to:

$$I_{Stokes} \propto (n+1)\omega_S^3 \omega_0 |\chi(\omega_0, \omega_S)|^2$$

And for the Anti-Stokes part to:

$$I_{Anti-Stokes} \propto n\omega_{AS}^3 \omega_0 |\chi(\omega_0, \omega_{AS})|^2$$

where $n = \frac{1}{\exp\left(\frac{\hbar\omega}{k_B T}\right)-1}$ is the Bose-Einstein factor, ω is the phonon frequency, ω_0 is the frequency of the incident light, ω_S=ω_0-ω (and ω_{AS}=ω_0+ω) are Stokes (and Anti-Stokes) frequencies, respectively.

Consequently, the ratio of Stokes/Anti-Stokes Raman intensities can be effectively employed to determine the temperature of the sample, assuming that the polarizability is constant in the Stokes/Anti-Stokes range:

$$T \cong \frac{\hbar\omega}{k_B} \ln\left(\frac{I_S}{I_{AS}}\right)$$

For a solid, in addition to the energy conservation, that is given by

$$\omega = \omega_0 - \omega_S$$

we have the wavevector conservation. The size of the Brillouin zone is in the order of $2/a$, where a is the size of the direct lattice. Using visible light, the photon wavevector is 2, which is typically 1000 times smaller than the Brillouin zone extension. The photon wavevector change is nearly zero comparatively to the size of the Brillouin zone. Thus, in a solid, the second law for Raman scattering is:

$$\boldsymbol{q_{phonon} = k_{incident\ photon} - k_{scattered\ photon} \cong 0}$$

As a consequence, not all phonon modes are Raman active. We can observe phonons corresponding to the point (center of the Brillouin zone) modulated by the polarizability.

For amorphous materials, the wavevector selection rule is relaxed permitting every mode to contribute to the spectrum with some coupling factors. Apart of this the Raman signal obeys the Bose-Einstein population statistics and the temperature of the sample can be extracted.

The power of the scattered light PS is proportional to the intensity of the incident light Io, and approximately the inverse of the wavelength in the fourth power:

$$P_S \propto \frac{I_0}{\lambda^4}$$

Therefore, to get intense Raman signals it is desirable to use a short excitation wavelength and a high laser power. However, when dealing with organic molecules one has to take into account the fluorescence when a photon of the incident beam is absorbed and the system stays in an excited state. When excited some of the energy is dissipated by molecular collisions or transferred to a nearby molecule, and then the remaining energy is emitted as a photon to relax back to the ground state. The emitted photon usually carries less energy and therefore has a longer wavelength than the excitation photon, thus the emitted fluorescence can be distinguished from the excitation.

In contrast to the Raman scattering process the fluorescence depends strongly on excitation energy and cannot take place at any frequency of the incident light. This means that a fluorescence peak is anchored at a specific frequency, whereas a Raman peak maintains a constant separation from the excitation frequency for a large range of excitation energies. Most organic molecules will tend to fluoresce when excited by high energy (short wavelength) photons. Fluorescence can strongly overwhelm the signal in the Raman spectrum. This is because the Raman scattering cross-section is comprised to a very small fraction (about 1 in 10^7) of the incident photons. As a result, visible lasers are typically only used for inorganic and semiconducting materials such as CNTs. For organic molecules it is important to shift the laser wavelength into the near infrared to reduce fluorescence while respecting the CCD spectral detection range. Due to their availability and the fact that they allow to reduce fluorescence without scarifying spectral resolution, 785nm diode lasers are often used for organic molecules or polymers with delocalized electrons. For increased sensitivity with inorganic molecules, a 532nm laser is the best choice because fluorescence is no longer an issue.

2.1.2 Raman spectroscopy of CNTs

Raman spectra can provide information about structural properties of CNTs: phonons which depend on the tube diameter; phonon resonances which depend on the electronic structure of the CNTs; as well as information about sample defects and doping state. Raman spectra from CNTs have a number of distinctive spectral bands which make it possible to distinguish between spectra measured on pristine samples that is, ideally defect-free, undoped, unstrained CNTs, and those measured on samples subjected to external perturbations such as electric and magnetic fields and strain or defects.

Typical Raman spectra of single-walled, double-walled and multi-walled CNT bundles are shown in Figure 2.1.

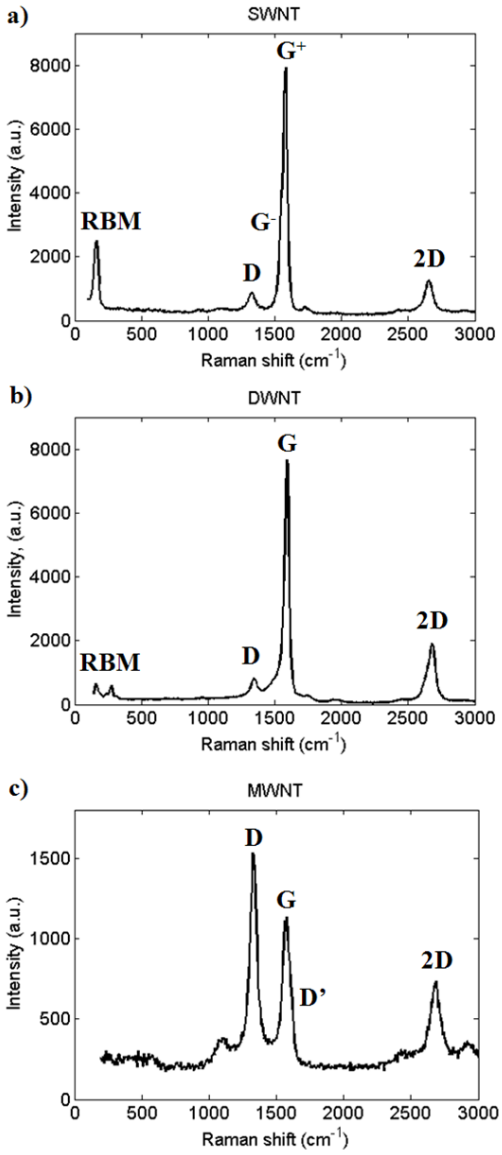

Figure 2.1. Typical Raman spectra of CNT bundles excited with λ=532nm a) single-walled b) double-walled and c) multi-walled.

Radial breathing mode

Radial breathing modes (RBMs) are present in CNTs and they fall in the low frequency range (between 120 and 350cm^{-1}). They are caused by radial oscillations of carbon atoms (Figure 2.2).

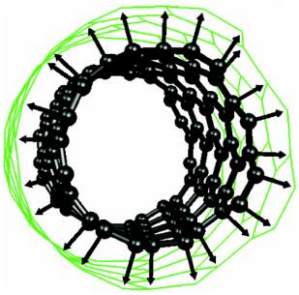

Figure 2.2. Radial breathing mode of an (8, 4) nanotube. The arrows indicate the motion of the carbon atoms during the vibration [96].

RBMs can be used to obtain information about the single wall nanotube (SWNT) diameter (d_t) through its frequency (ω_{RBM}):

$$\omega_{RBM} = \frac{A}{d_t} + B$$

where A and B are experimentally determined parameters. For a typical single-walled CNT bundle with a diameter range ~ 1.5 ± 0.2nm, A = 234cm^{-1}, B = 10cm^{-1} [97], where the B parameter is assigned to the tube-tube interaction. For an isolated SWNT on a Si substrate, A = 248cm^{-1}, B = 0 [98].

It is important to point out that, for the usual diameter range 1nm $< d_t <$ 2nm, these two sets of parameters give similar d_t for a given ω_{RBM}, differing considerably only for $d_t <$ 1nm and $d_t >$ 2nm. However, for $d_t <$ 1nm, the lattice distortions leading to a chirality dependence of ω_{RBM} should be taken into account leading to a more complex relation [99]. For large diameter tubes ($d_t >$ 2nm) the intensity of the RBM feature is weak and is hardly observable.

The RBM frequency can be as well derived from continuous mechanics [100]:

$$\omega_{RBM}(cm^{-1}) = \frac{1}{d}\sqrt{\frac{4c_{11}h}{Nm_0}} = \frac{235}{d_t(nm)}$$

where c_{11} is the elastic constant of graphene, h is the height of the graphene layer and N is the number of carbon atoms of mass m_0 per unit area.

Or from the G mode frequency [100] (see next section):

$$\omega_{RBM}(cm^{-1}) = \frac{a_{c-c}}{d}\omega_G = \frac{226}{d_t\,(nm)}$$

where $a_{c\text{-}c}$ is the carbon-carbon distance.

The dependences of the RBM frequency ω_{RBM} on the nanotube diameter d_t for bundles and isolated tubes are shown in Figure 2.3. The dotted line represents the dependence for a nanotube bundle and a solid one - for isolated nanotubes on the Si substrate.

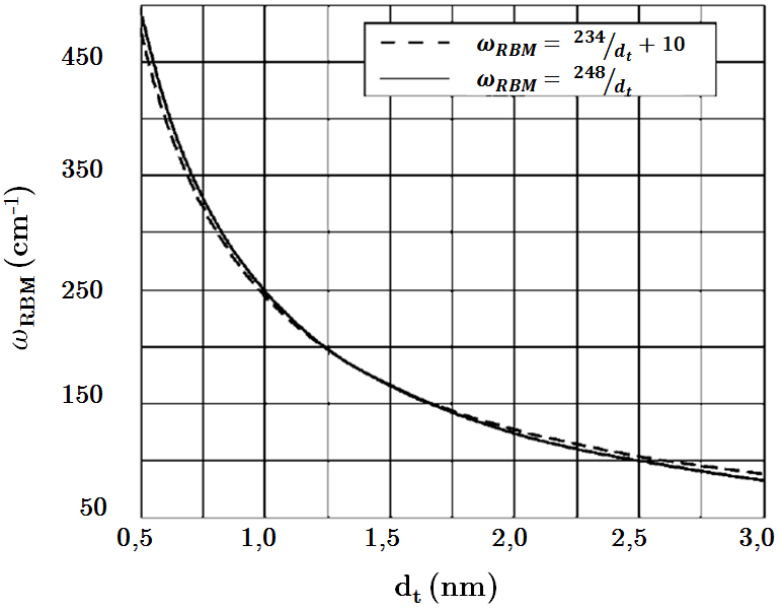

Figure 2.3. Dependence of the RBM-frequency on the single-walled CNT diameter [98] [97].

The RBM features can be used to make (*n, m*) assignments for individual isolated SWNTs, by utilizing a Kataura plot (Figure 1.7a in Chapter 1). The d_t values (which are dependent on the (*n, m*)) can be obtained from the RBM frequency measurements, and the E_{ii}~E_L from the resonance condition when using a tunable laser.

In particular using the Kataura plot one can identify metallic and semi-conducting tubes. This approach has been widely employed since no preliminary preparation is required. Krupke *et al.* [101] developed a method to separate metallic from semiconducting single-walled carbon nanotubes from suspension using alternating current dielectrophoresis. To prove the effectiveness of the separation a comparative Raman spectroscopy study was carried out on the dielectrophoretically deposited tubes and on a reference sample. Figure 2.4.

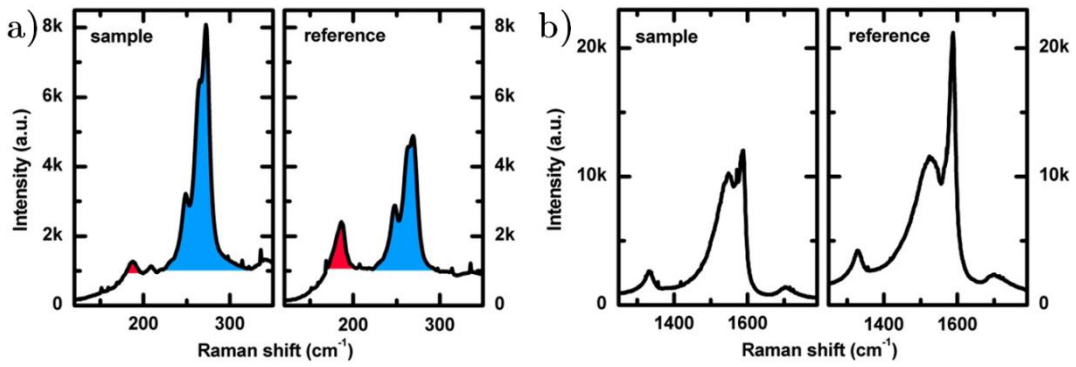

Figure 2.4. Raman spectra of SWNTs deposited via ac dielectrophoresis compared to a reference sample deposited on Si without the application of an electric field.
a) RBM associated with metallic (blue) and semiconducting (red) SWNTs
b) G-mode region [101].

DWNT Raman spectra exhibit a pair of RBM peaks, which can be associated with the inner and outer tubes. It was shown [102] that the inner and outer tubes impose considerable stress on one another, and this stress influences significantly their RBM frequencies, making the (*n, m*) identification different from that used for SWNTs.

Levshov *et al.* [103] performed transmission electron microscopy, electron diffraction, and Raman scattering experiments on an individual suspended double-walled carbon nanotube. The first two techniques allowed the unambiguous determination of the DWNT structure: (12,8)@(16,14). However, the low-frequency features in the Raman spectra couldn't be connected to the derived layer diameters by means of the 1/d power law, used for the diameter dependence of the SWNT radial-breathing mode. This disagreement comes from the mechanical coupling (hardening) between the layers of the DWNT, which results in collective vibrational mode.

In the case of MWNTs the RBM bands in Raman spectra are not evident, since the RBM signal from large diameter tubes is usually too small. It has been found that the absolute Raman cross section which is proportional to the matrix element $\left|\frac{\partial(E_b^c - E_b^v)}{\partial u}\right|^2$ varies roughly as $1/d^2$ (Figure 2.6) [104]

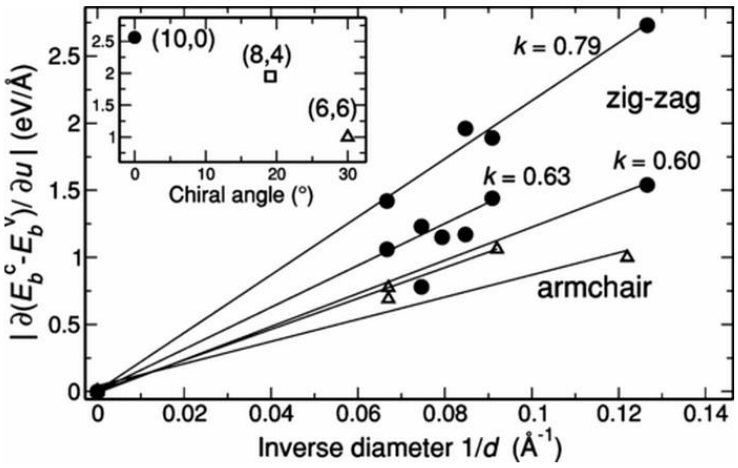

Figure 2.6. Calculated band-energy changes (absolute value) per unit change in radius for zigzag (circles) and armchair tubes (triangles) [104].

Raman G-band

One of the main characteristic bands of CNTs is the so called Raman G-band, which is the most intense band and is located between 1570 and 1600cm^{-1}.

In contrast to the graphene G band, which exhibits one single Lorentzian peak at 1582cm^{-1} due to the tangential vibrations of the C atoms, the SWNT *G*-band splits into two sub bands: the G^+ (~1590cm^{-1}) band and a less intense G^- (~1530-1570cm^{-1}) band.

For SWNTs the TO phonon mode is along the circumference, while the LO mode is along the tube axis. Full ab-initio calculation are required to attribute the LO and TO modes to the G^+ and G^- bands. In the case of a semi-conducting tube, the G^+ is along the tube axis (LO) and the G^- is along the circumference (TO), the opposite attribution was found for metallic tubes (Figure 2.7) [105].

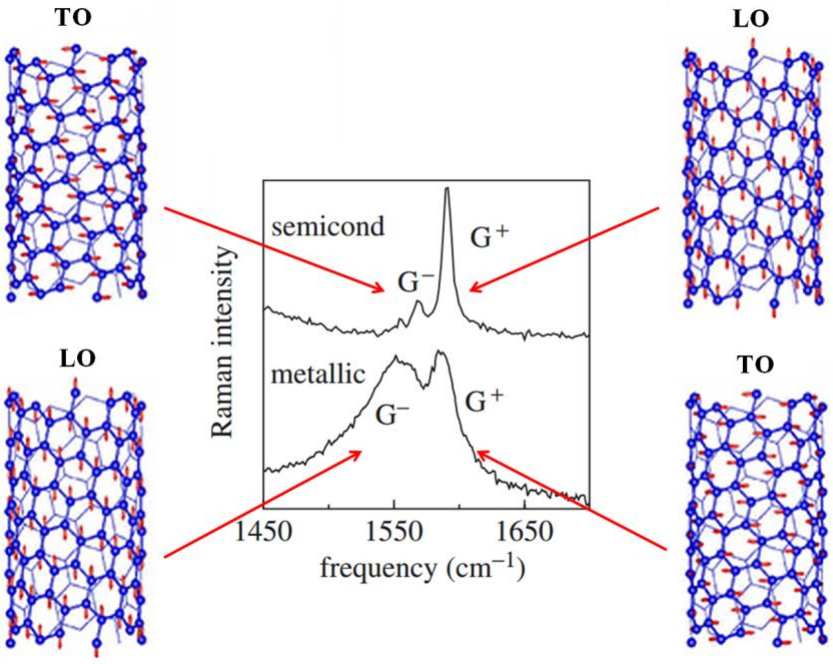

Figure 2.7. Raman G^+ and G^- peaks for semiconducting and metallic SWNTs. In semiconducting tubes the two peaks have a Lorentzian line shape and a FWHM of ~12 cm^{-1} [105].

The frequency of the G band for a metallic tube is affected by so called Kohn anomaly. For certain phonons with a wave vector connecting two points of the Fermi surface it is possible to have an abrupt change of the electronic screening of the atomic vibrations. This results in a sudden softening of the phonon frequencies, which is called Kohn anomaly. This is possible for the K and points in the Brillouin zone, corresponding to the phonons of the G and D bands.

The position of the G^- band is diameter dependent. It is possible to estimate the diameter of the tube from the shift of the G^- band, but with a lower accuracy than from the RBMs [102]:

$$\omega_{G^+} - \omega_{G^-} = -\frac{45.7}{d^2}$$

for semi-conducting tubes and

$$\omega_{G^+} - \omega_{G^-} = -\frac{79.5}{d^2}$$

for metallic tubes

We have performed Raman experiments on a single peapod (C_{60}@SWNT) and deduce a diameter of 1.5nm from the RBM frequency and the G band splitting. The presence of a resonant Raman response only under 2.33eV excitation combined with the peapod diameter allowed us to identify the external SWNT as a semiconducting tube. Thereafter the selective excitation of the C_{60} at an absorption threshold transformed the C_{60} into an inner tube leading to a DWNT (Figure 2.5) [106].

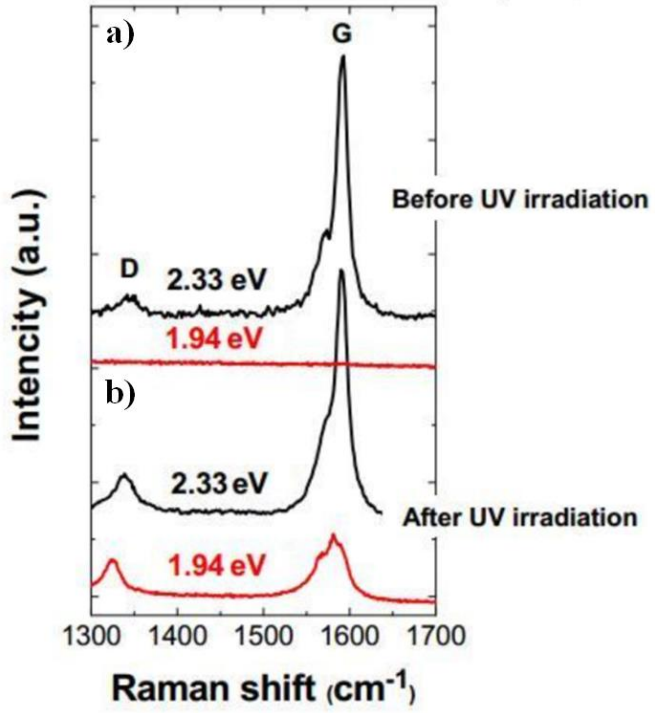

Figure 2.5. Raman spectra at different excitation energies of a) a peapod and b) a peapod transformed into a DWNT after UV irradiation [106].

For DWNTs there are two main contributions attributed to the two G^+ modes that are located at $1592cm^{-1}$ for the outer nanotube and at $1581cm^{-1}$ for the inner nanotube. The G^+ bands overlap at normal pressure and split with increasing pressure [107]. The G^- modes are weaker in intensity and are located at lower frequency shifts.

Whereas the G^+ - G^- splitting is large for small diameter tubes, the G band splitting for large diameter MWNTs is both small and smeared out because of the diameter distribution and a large number of defects. Therefore the G band exhibits a weakly asymmetric characteristic lineshape, with a peak appearing at the graphite frequency $1580cm^{-1}$.

The G bands for different tubes and highly oriented pyrolytic graphite (HOPG) are shown in Figure 2.8.

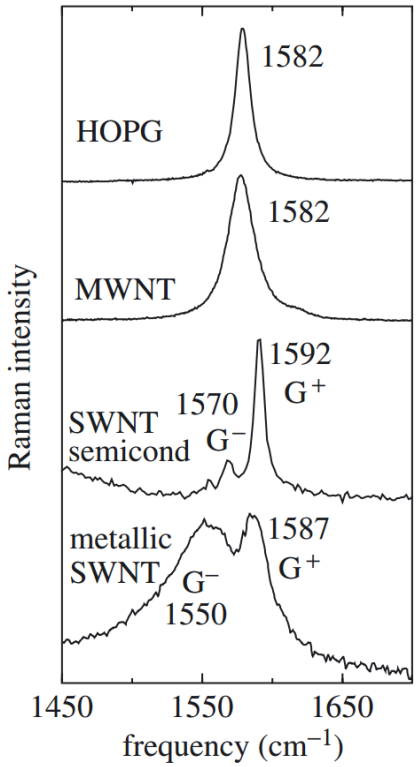

Figure 2.8. The shape and position of the G-band in Raman spectra of various carbon materials [108].

There are several effects which can be seen with the Raman G band for nanoubes. The main effects are: strain (leading to a shift of the G band), doping (leading to a shift which depends on the species interacting with the tube and also due to the move of the Fermi level to some quenching [109], [107] and temperature change (leading to a shift, with a rate of -0.024cm^{-1}/K, except for non-equilibrium phonons) [110].

Raman D and D' spectral bands

The D band at around 1350cm^{-1} with visible excitation is observed in sp^2 bonded carbon materials with defects. The understanding of the physical process at its origin was found only in 2000 and accepted by the community in the following years due to many successful consistent explanations. The origin of the D mode in graphite and carbon nanotubes is now attributed to defect-induced double resonant scattering. The defect-induced Raman process consists of four steps:

1. Excitation of an electron–hole pair,
2. Inelastic scattering of the electron (or hole) by a phonon,
3. Elastic scattering of the hole (electron) by a defect,
4. Recombination of the excited electron and hole and emission of a photon.

The second and third steps can be interchanged. For the second-order Raman spectrum (2D band, see next section), the elastic defect scattering is replaced by inelastic scattering by a second phonon, which means that no defect is needed. The process is double resonant, if two of the transitions are real [111].

Scattering between two inequivalent K points (inter-valley) of the graphene Brillouin zone, K and K', leads to the D mode, whereas scattering close to the same K point (intra-valley) results in D' (~1610-1620cm^{-1}) (Figure 2.9).

Only fully symmetric (T_1 or TO) phonons can contribute to the scattering within the same nondegenerate band (D mode) (Figure 2.9a solid arrow). The dashed arrow indicates another possibility of double-resonant scattering, involving phonons from near the Γ point with T_3 symmetry (D' mode) (Figure 2.9a dotted arrow).

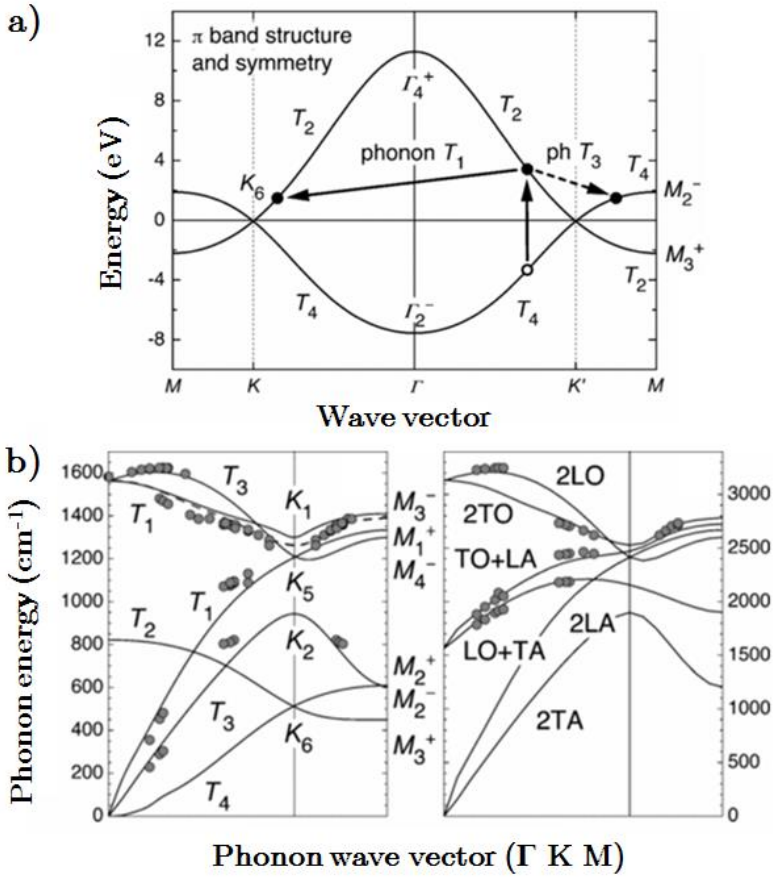

Figure 2.9. a) Electronic π and π bands of graphene along Γ–K–M. The symmetry of the bands is given b) Disorder-induced Raman modes mapped onto the phonon dispersion of graphite (dots). The full lines are ab initio calculations; the dashed line is a cubic-spline fit to the experimentally determined dispersion* [111].

The D-mode in the Raman spectrum is present at the frequency ω_D=1350cm^{-1} at λ=515nm (2.41eV) and is dispersive with the excitation laser energy (Figure 2.10) [112]:

$$\frac{\Delta\omega_D}{\Delta E} = \frac{60cm^{-1}}{eV}$$

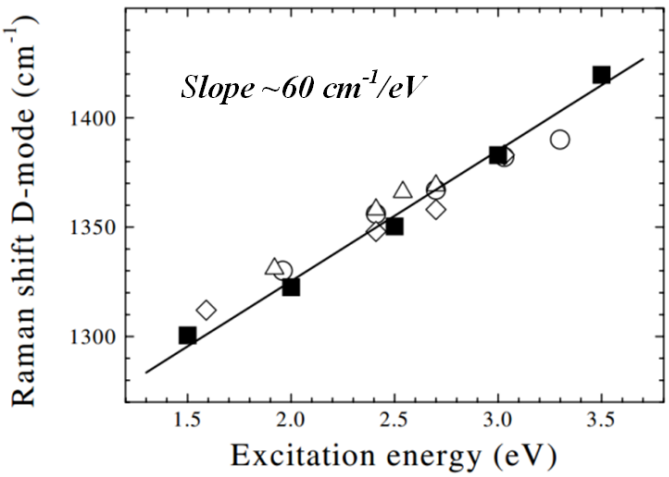

Figure 2.10. Measured and calculated frequencies of the D band as a function of the excitation energy. The open symbols correspond to experimental data and the closed squares to the calculated phonon energies in double resonance [112].

Probing defects with Raman spectroscopy

Ratio of the intensity of D and G band: I_D/I_G:

Tuinstra-Koenig [113] proposed to quantify the evolution of disorder by the ratio I_D/I_G of the integrated intensities of the disorder-induced D band and the G band using the following relation:

$$\frac{I_D}{I_G} = \frac{C(\lambda)}{L_a}$$

where L_a is the size of a crystalline sp^2 cluster, C(λ) is the proportionality constant that depends on the excitation laser wavelength λ. (C(λ) ≈ 4.4nm for λ = 488nm)

A remarkable characteristic in the Raman spectrum of nanographites is a strong dependence of the ratio I_D/I_G on the excitation laser energy E_L used in the Raman experiment [114]:

$$\frac{I_D}{I_G} \propto E_L^{-4}$$

Cançado *et al.* [115] showed that the dependence of the ratio I_D/I_G on the excitation laser energy comes from the fact that the G band differential cross section β is proportional to E_L^4 while the D band differential cross section does not change with the excitation laser energy (Figure 2.11).

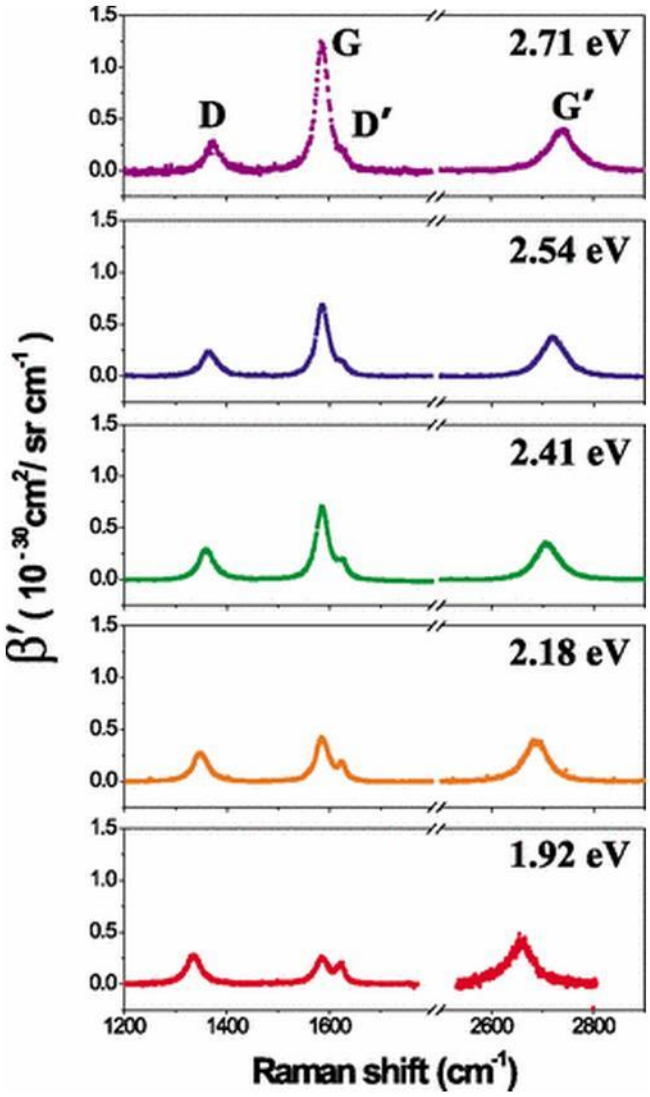

Figure 2.11. The spectral differential cross section of the D, G, D', and 2D bands for the nanographite sample with L_a=35nm, using five different values of E_L (indicated at the top of each spectrum) [115].

But this energy dependence holds only for large crystallite sizes and fails for small crystallite sizes. The Tuinstra and Koenig law is not consistent with a work on graphene where a simple model leads to $I_D/I_G=48/L_a$ (nm) [116].

Consequently, even though the ratio I_D/I_G is often used to characterize the quality of the sample, it cannot serve to get quantitative information. For a set of samples, the evolution is representative, but for various samples making a conclusion is less clear. The line width of the G and D bands and the history of the sample need to be taken into account.

Ratio of the Intensity of the D and D' band: $I_D/I_{D'}$

Raman spectroscopy is able to probe the nature of disorder in graphene through defect-activated peaks. Eckmann *et al.* [117] presented a detailed analysis of the Raman spectra of graphene containing different types of defects. They found that the intensity ratio of the D and D′ peak ($I_D/I_{D'}$) is maximum (~13) for sp^3-defects, it decreases for vacancy-like defects (~7), and it reaches a minimum for boundaries in graphite (~3.5) (Figure 2.12).

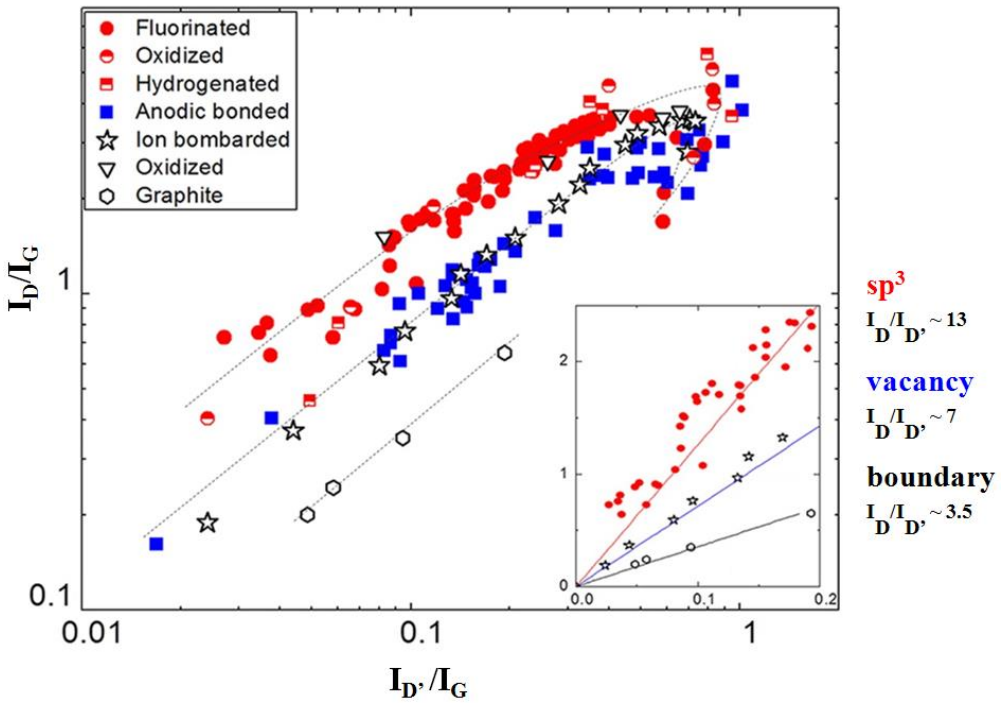

Figure 2.12. I_D/I_G versus ratio $I_{D'}/I_G$. Data from literature (open symbols) have been included: ion bombarded graphene, oxidized graphene and graphite with different grain sizes. The dotted lines are only a guide for the eyes. The inset shows the linear dependence between the two parameters at low defect concentration, giving different $I_D/I_{D'}$ for different type of defects [117].

Ab-initio calculations done by Venezuela *et al.* [118] give a limit of 1.3 for on-site defects (see Figure 18 of the publication).

Raman 2D-band

The first overtone of the D-band arises from a two-phonon double resonant Raman scattering process and is denoted historically by G'. It is observed in the region of 2450 - 2650cm^{-1}. The same band is also referred to as the 2D band. To activate the 2D band, no defects are needed. The Raman fundamental selection rules are satisfied if the sum of the two phonon wave vectors is zero.

A complete description of the 2D band in carbon nanotubes is still a subject of research, but the understanding of its nature has become possible with detailed studies on graphene. Graphene is a simpler system and the coupling in the case of a Bernal bilayer can be fully studied. That is why in the following, we focus our attention on the

2D mode of graphene assuming that the main difference with nanotubes is the diameter dependence which is given for a SWNT by the following relation [119]:

$$\Delta\omega_{2D}(cm^{-1}) = -\frac{35}{d\ (nm)}$$

In a single layer graphene the 2D band is sharp and roughly 4 times more intense than the G band (Figure 2.13) [120].

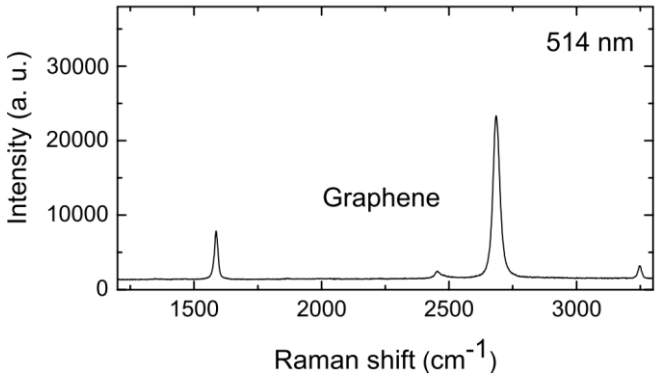

Figure 2.13. Raman spectrum of graphene at 514nm [120].

A bilayer has a much broader and up-shifted 2D band with respect to graphene. It has 4 components, 2D1B, 2D1A, 2D2A, 2D2B; two of which, 2D1A and 2D2A, have higher relative intensities than the other two, as indicated in (Figure 2.14a). These bands can be derived from the electronic band structure and are due to weak coupling between the two layers. Thus, for a bilayer graphene with AB stacking, the 2D band is due to 4 contributions. For random stacking (pyrolitic), the coupling between the layers is very weak and in the 2D range, there is only one Lorentzian that is slightly larger than in the case of a single layer.

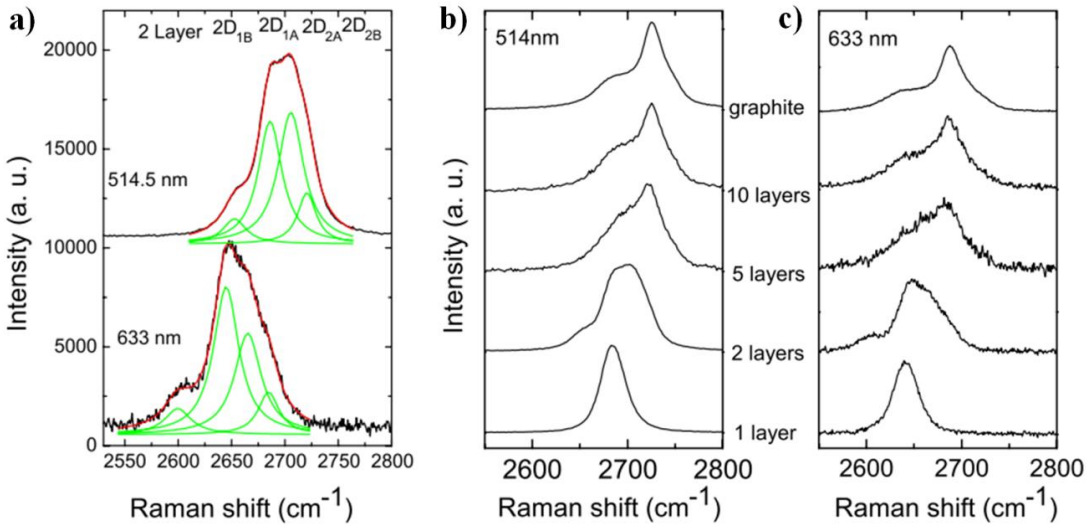

Figure 2.14. a) The four components of the 2D band in 2 layer graphene at 514 and 633nm b) evolution of the spectra at 514nm with the number of layers c) Evolution of the Raman spectra at 633nm with the number of layers [120].

Figures 2.14b and 2.14c show that a further increase of the number of layers leads to a significant decrease in the relative intensity of the lower frequency 2D1peaks. For more than 5 layers the Raman spectrum becomes hardly distinguishable from that of bulk graphite. Thus Raman spectroscopy can clearly distinguish a single layer, from a bilayer and a few (less than 5) layer.

In the case of CNTs the 2D band structure is strongly dependent on the number of walls. Single wall carbon nanotubes show a sharp 2D peak similar to that measured for graphene [121]. For double-walled tubes the inner and outer contributions are not located at the same place leading to global shape changes due to electronic interaction between the layers. Finally we observed that the behavior of the 2D band is different for CCVD grown DWNTs and those obtained from peapods [106].

2.1.3 Double wall CNTs as molecular sensors

The G band of a DWNT is relatively broad due to contributions of the inner and outer tubes. By using high pressure, it is possible to observe the splitting of the broad G band into at least two G^+ bands coming from the inner and the outer tubes.

When the inner and the outer tubes are spectrally well separated, small shifts of the G^+ band of the outer tube can then be well detected. The additional contributions are attributed to the G^- modes. They are weaker in intensity and their respective positions are affected by coupling between the tubes.

The inner tube feels only the strain transmitted by the outer tube while the G^+ band of the outer tube is influenced by both the bond length variation (strain) and the Fermi level position (electron-phonon coupling). By comparing the spectral shifts of the inner and outer tube we can sense the electron phonon coupling of the tube with its surrounding. Thus DWNTs can be considered as molecular sensors.

We have used this ideal nano-sensor in the case of superacid to determine the relationship between the charge transfer f_C and the Raman shift of the G^+ band. To convert the G band shift to charge transfer, Sumanasekera *et al.* [122] results were used. They derived the value of $320f_C$ in cm^{-1} via electrochemical measurements. But this conversion factor is not in accord with phonon shifts observed in Graphite Intercalated Compounds (GICs) by Eklund *et al.* [123].

Lazzeri and Mauri [124] have computed electron-phonon coupling in graphene and showed that the total phonon shift $\Delta\omega$ could be separated into a contribution due to lattice contraction (strain) $\Delta\omega_s$ and a contribution due to nonadiabatic (dynamical) effects labeled $\Delta\omega_d$ *(Figure 2.15)*:

$$\Delta\omega = \Delta\omega_s + \Delta\omega_d$$

with

$$\Delta\omega_s(cm^{-1}) = 350f_C$$

$$\Delta\omega_d\ (\mathrm{cm}^{-1}) \approx\ 204\sqrt{f_C}, \text{for large } f_C$$

When CNTs are immersed in sulfuric acid, a redox reaction takes place. The charge of CNTs with holes is associated with the release of H_2. Recently DFT calculations were performed to understand how this interaction affects the nanotubes. The H^+ modifies the electronic band structure and tends to get close to the nanotube and the HSO_4^- can be in contact with CNT^+ without any modification of the electronic ban structure of the CNT.

At first we deduced the strain induced shift of the outer tube from the shift of the inner tube using the following equation [107]:

$$\Delta\omega_{outer} = 1.7\,\Delta\omega_{inner}$$

Then using high pressure [125] and neutron experiments [126] we deduced the charge transfer from the strain of the outer tube.

The Raman G band shift for the outer nanotube, $\Delta\omega$, as a function of hole charge transfer per carbon atom, f_C, was found to be:

$$\Delta\omega\ (\mathrm{cm}^{-1}) = (350 \pm 20) f_C + (101 \pm 8)\sqrt{f_C}$$

The remaining shift is due to electron phonon coupling. One can note that the value reported by Sumanasekera *et al.* [122] takes only strain into account.

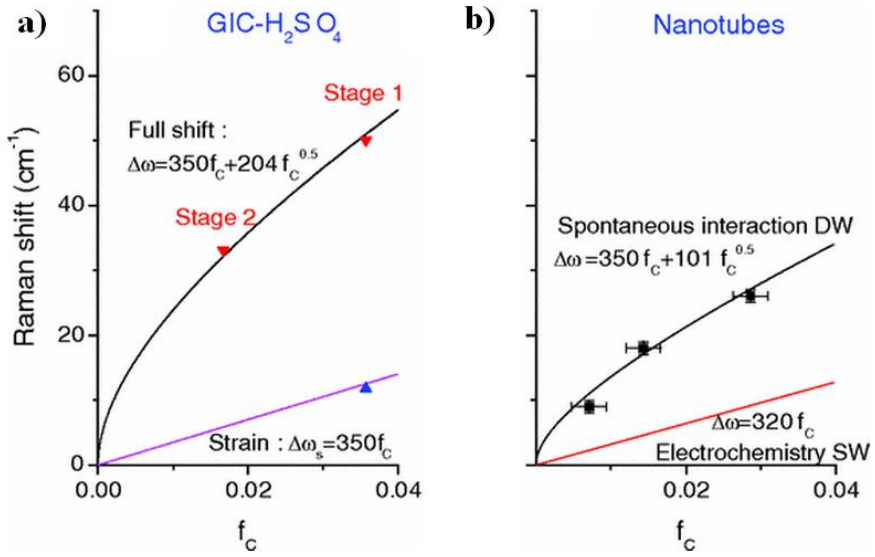

Figure 2.15. a) G mode shift versus the charge transfer for GIC-H_2SO_4 (red upper triangles) with fitted line using a fixed linear term and an adjustable prefactor for the square root term (black line). The lattice contractions were extracted from neutron data (blue lower triangle) [126] *and converted to Raman shifts using high pressure data* [125]*. The linear term (purple line) has been obtained from DFT calculation* [124]*. b) Raman shift of the outer nanotubes of DW with f_C deduced from Raman G^+-band shift of the inner nanotube (black squares) and fitted line using a fixed linear term and an adjustable prefactor for the square root term (black line). The Raman shift deduced from electrochemical data is also reported (red line)* [122]*. The same scale has been used for all plots.*

This result has also been used by Tishkova *et al.* [77] to probe the dispersion of DWNTs in a polymer matrix.

2.1.4 Raman mapping and image analysis

The Raman shift of the G band was previously used to investigate the load transfer in the nanocomposites [127] and their tensile properties [128] [129]. Tishkova *et al.* [77] have recently shown that Raman spectroscopy could also be effectively employed to access the dispersion state of CNTs in a PEEK polymer matrix. As it was previously shown that the G band of DWNTs is split due to the contribution of the two walls. The inner tube feels only the strain transmitted by the outer tube while the G band of the outer tube is influenced by both the external pressure [125] from the surrounding matrix and the chemical doping [109].

For well dispersed DWNTs the G band of the outer tubes is up shifted when compared with the inner tube (which serves as a reference) due to the p doping of the outer tube by the chemical groups present in the polymer matrix. This means that the interaction of the outer tube with the polymer matrix can be used as a local sensor for the dispersion of the DWNTs in the PEEK matrix. In case the DWNTs are not well dispersed the interaction with the polymer matrix is reduced. Thus the splitting of the G band is a characteristic of a better dispersion.

Figure 2.16a-b show the G band Raman spectra of 0.8wt% DWNTs/PEEK composite at two different locations on the sample.

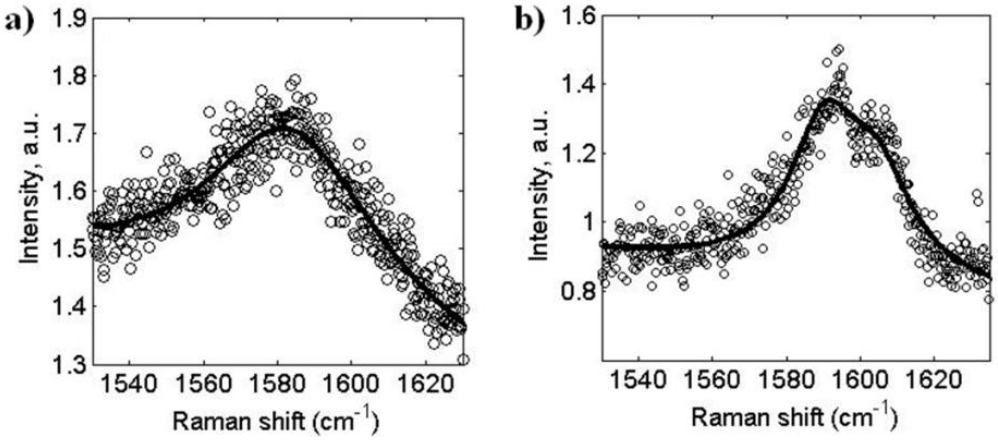

Figure 2.16. High frequency Raman spectra of 0.8wt% DWNTs/PEEK composite for: a) agglomerated DWNTs b) well dispersed DWNTs. The black solid line is the Lorentzian fit to the G band of DWNTs [77].

The G band Raman spectrum in Figure 2.16a is a characteristic of DWNTs agglomerates because no splitting is observed. In Figure 2.16b the up shift of the G band is associated with the interaction between the PEEK matrix and the outer tube and suggests that DWNTs are well dispersed in the polymer matrix.

For statistical analysis several Raman maps were carried out at different regions on the samples. Figure 2.17a–c shows the intensity maps and Figure 2.17d-f shows the spectral position maps of the G band over an area of 200×200μm for a) 0.16, b) 0.8 and c) 1.2wt%. The images are represented for a broad G band without considering the two components.

The G band was analyzed considering three components: inner G^+, outer G^+ and outer G^-. It was observed that the up shift of the broad G band was clearly due to the up shift of the contribution of the G^+ band of the outer tubes.

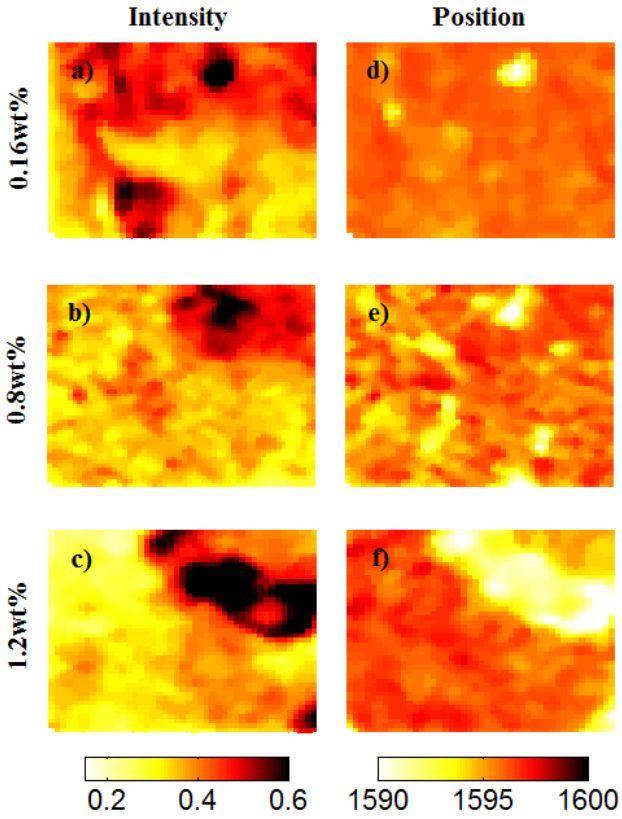

Figure 2.17. Raman imaging of DWNTs/PEEK composites at different weight fraction. a–c) intensity of the G band d–f) the position of the G band. (a and d) 0.16wt%. (b and e) 0.8wt%. (c and f) 1.2wt%. The size of the maps is 200 × 200μm [77].

As a first approximation the intensity I_G of the G band was assumed to be proportional to the density of tubes. At low concentration the G band is absent in some areas due to the lack of nanotubes. As the CNT concentration increases, I_G increases and larger several micrometer sized agglomerates of nanotubes are visible. Figure 2.17d–f shows that the G band is located at 1600–1605cm^{-1} at low CNTs concentration for a large part of the image. At higher concentration the G band is downshifted in energy. At a weight fraction of 1.2wt% (Figure 2.17f), the G band is strongly downshifted to 1570cm^{-1} at several positions on the nanocomposite sample.

In order to evaluate the quality of the DWNT distribution in the PEEK matrix at different CNT concentrations the weighted mean W and the associated standard deviation σ of the G band position have been determined:

$$W = \frac{\sum_i I_i P_i}{\sum_i I_i}$$

$$\sigma^2 = \frac{\sum_i I_i (P_i - \overline{P})^2}{\sum_i I_i}$$

where P, $\overline{P}$ and I are respectively the spectral position, the spectral position mean value and the intensity of the G band.

The weighted mean of the spectral position refers to the interaction of the outer tube with the polymer. If the G band of the outer tube is up shifted, the DWNTs are in interaction with the polymer matrix. The standard deviation corresponds to the homogeneity of the dispersion. This means when the weighted mean is up shifted and the standard deviation is close to zero, the DWNTs are well dispersed in the polymer matrix.

Figure 2.18 shows the obtained weighted mean of the spectral position and its standard deviation as a function of DWNTs weight fraction.

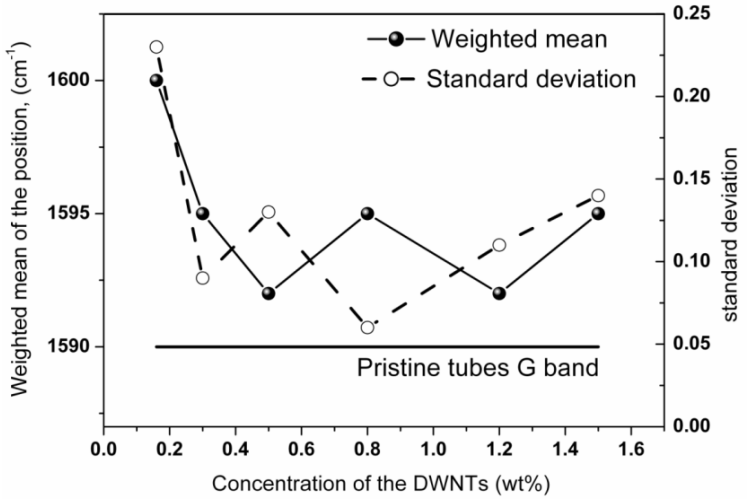

Figure 2.18. Weighted mean and standard deviation of the G band position as a function of DWNTs/concentration in PEEK matrix. Solid line – position of the G band for the pristine DWNTs (from 1582 to 1600cm^{-1}) [77].

The weighted mean of the G band position below the percolation threshold (0.3wt%) displayed the highest value indicating a good dispersion, while above 0.3wt% the value was found independent of the weight fraction and the standard deviation presented the same behavior.

So, using a DWNT as a molecular sensor, Raman spectroscopy was able to show that the dispersion of individual tubes was better at low concentration but the overall dispersion was not homogeneous.

For large scale use of CNTs in polymer composites MWNT are necessary due to their lower cost. Guehenec *et al.* [130] have studied dispersions of MWNTs by Raman mapping. Figure 2.19 represents a typical Raman spectrum obtained for MWNT/PEEK composite. Apart of the G and D bands one can also see a peak at 1144cm^{-1} corresponding to the asymmetric C—O—C stretch vibration in the PEEK polymer.

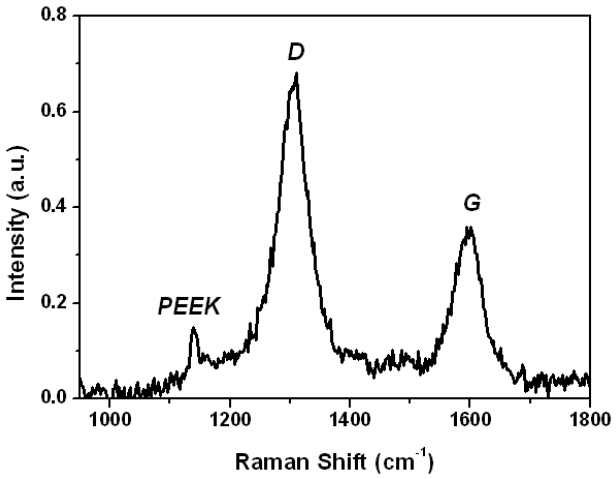

Figure 2.19. A typical Raman spectrum obtained for a 3wt% PEEK/MWNT composite without considering the background [130].

Three Raman maps based on the intensities of the D, G and PEEK bands were generated. Figure 2.20 shows an example of these maps. Black parts correspond to lower intensities while brighter parts to higher intensities. Each map is presented in one of three primary colors (red, green, blue) (Figure 2.20); the superimposed image is formed by adding the three primary color maps. The total image is shown in Figure 2.20d. Red and green colors give together yellow (D and G band). The parts which are presented in yellow correspond to the agglomerates of nanotubes. The blue parts correspond to areas with PEEK only.

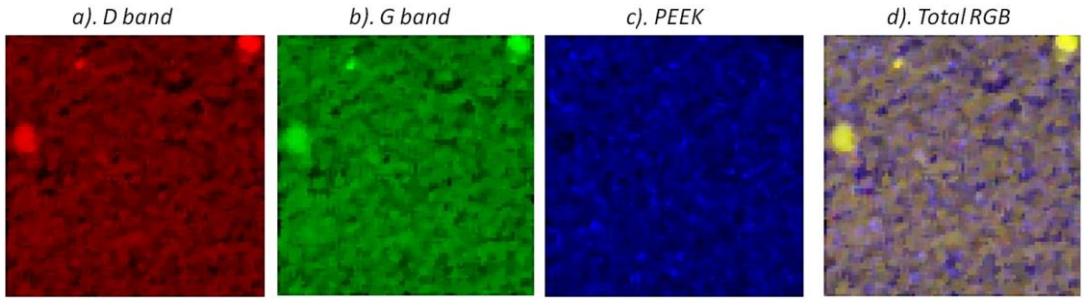

Figure 2.20. Raman spectral images of the intensities of the a) D band in red b) G band in green c) band from polymer PEEK in blue d) superimposed RGB image [130].

To probe the homogeneity of the tube distribution in the composite, Raman maps ranging from 40 to 400μm were recorded. Figure 2.21 presents the summary of all the data obtained for different scales and different samples. At the lower scales one can notice agglomerates and zones only with polymer for sample prepared at 100 and 400rpm. At larger scale, 200×200μm, the distribution for all the samples appears homogeneous. And at the largest scale, 400×400μm, one can notice a few big agglomerates, which could not been observed at lower scales.

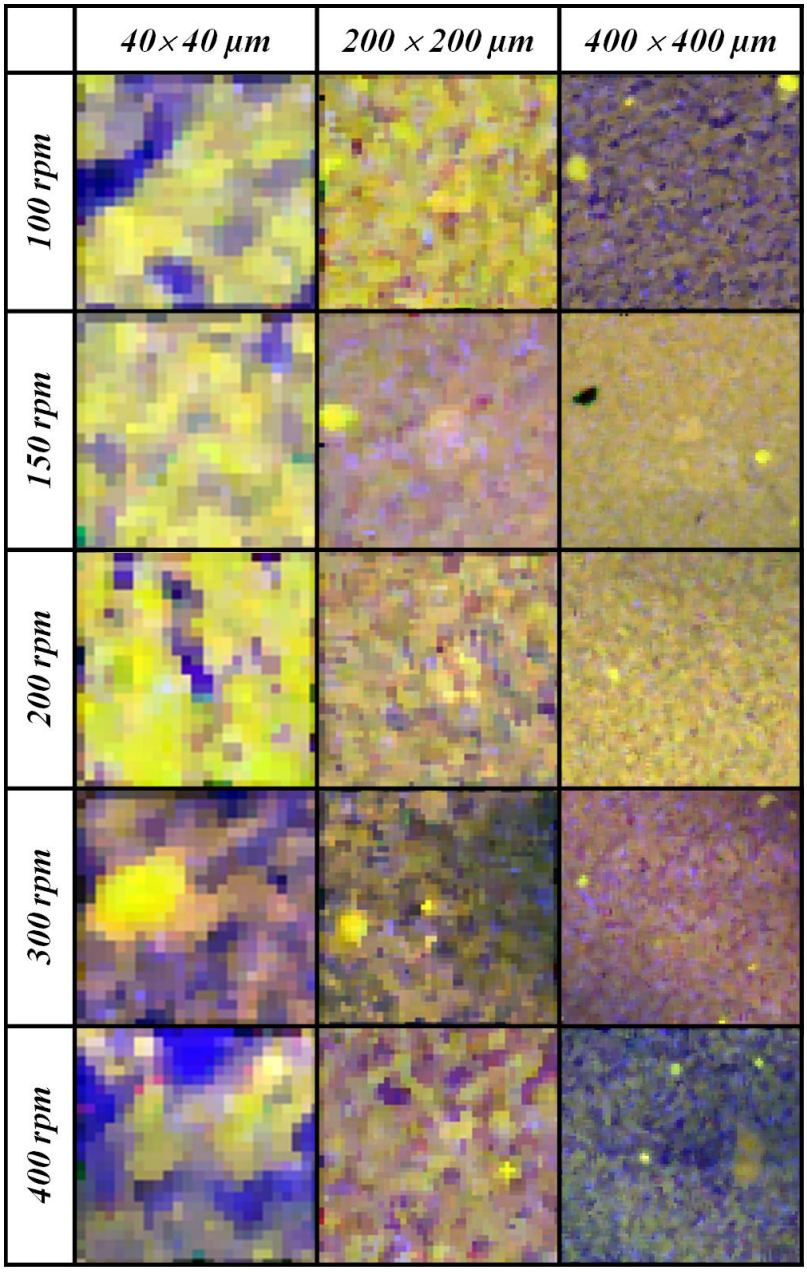

Figure 2.21. Raman spectral images of the dispersion of MW nanotubes in PEEK matrix presented as RGB images. D band (red), G band (green) give together yellow color, the polymer PEEK is presented in blue [130].

To quantify the dispersion of the CNTs the relative noise of the image $2\sigma/I$ was calculated, where σ is the standard deviation and I is the mean intensity of the G band over a map. The minimum of the noise corresponds to the best distribution of the MWNTs. Figure 2.22 represents the relative noises for all samples and measured at different scales. All the three curves show the same tendency. The minimum of the relative noise falls in the 150–200rpm range. This means that at medium speed, the dispersion of the CNTs is more homogeneous compared to fast or slow mixing.

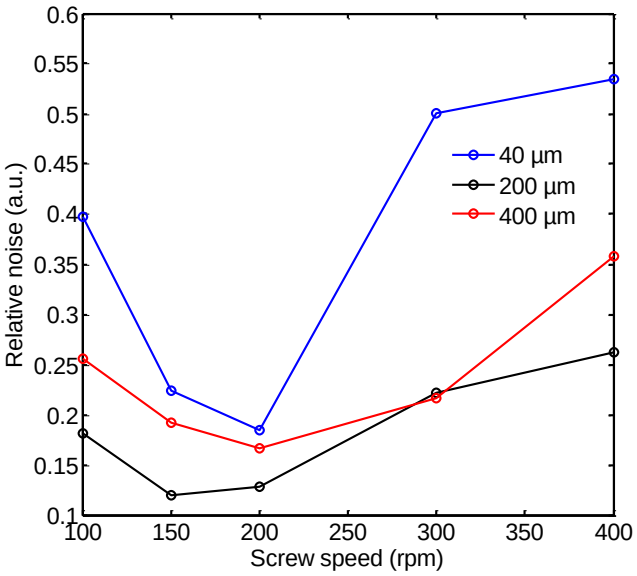

Figure 2.22. Relative noise $2\sigma/I$ for the G band variations in the samples prepared with different speeds. In blue 40 × 40µm; in red 200 × 200µm, and in black 400 × 400µm. The minimum correspond to the best tube dispersion: 150–200rpm [130].

To see whether the tubes were affected by the speed of the twin screw, the mean Raman spectrum for each area as a function of screw speed and the relative intensity of the D band with respect of the G band was calculated. This relative intensity is often used to characterize the defects in CNTs. Figure 2.23 shows the results. The major tendency was that the relative intensity was decreasing with increasing screw speed. This result was attributed to the shortening of the CNTs at higher screw speed that reduced the defects present in the tubes.

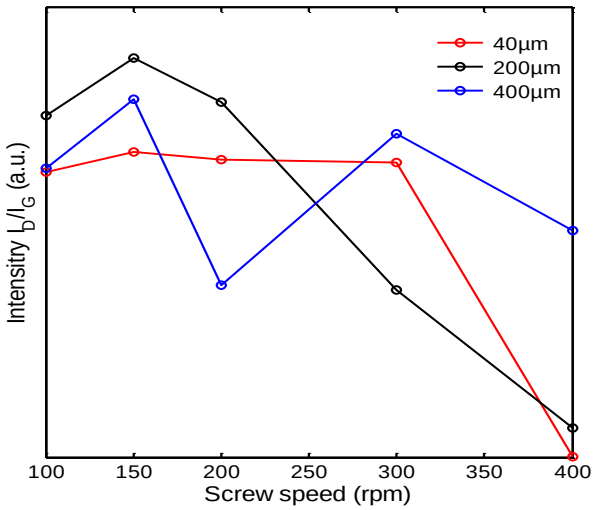

Figure 2.23. The relative intensity of the D band compared to the G band of the averaged Raman spectra calculated for each investigated area as a function of screw speed [130].

These results were consistent with the electrical conductivity measurements, where the optimal conductivity of a composite with CNT content above the percolation threshold (3wt%) was obtained for an intermediate screw speed of 200rpm (Figure 2.24).

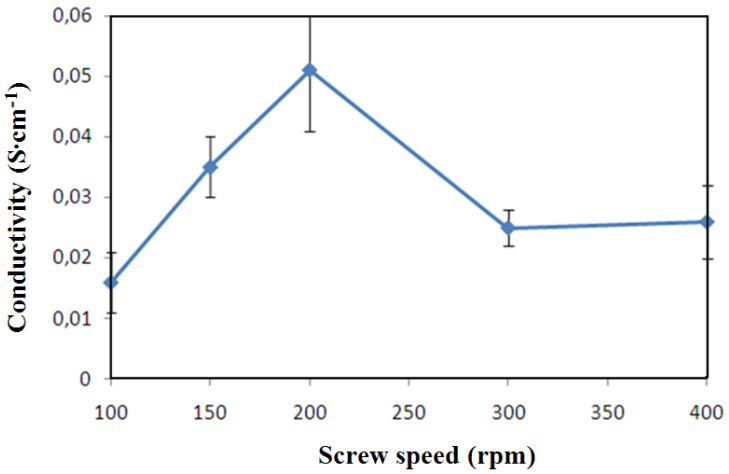

Figure 2.24. Conductivity as a function of screw speed for PEEK/3wt% MWNTs [130].

Thus, two different methods were proposed to probe the dispersion of carbon nanotubes in the composites by Raman spectroscopy. This thesis is based on the work of Tishkova *et al.* and proposes further expansion and development of Raman spectroscopy to investigate CNT composites.

2.1.5 Parameters of Raman spectrometers used

Raman spectroscopy was carried out on an Xplora instrument from Jobin-Yvon-Horiba in a back-scattering configuration with a ×100 or ×50 optical objective which gives a laser spot of ~1-2μm in size and a motorized or piezo electric XY-Table.

For PEEK polymer composites we used a 785nm laser excitation wavelength at low laser power (0.4 mW) in order to avoid luminescence and overexposing the composite with the illuminating laser beam. At this wavelength vibrational bands of both CNTs and PEEK can be observed.

For copper composites a 532nm laser excitation wavelength was used at 3.8mW laser power.

Stocks/Anti-Stocks measurements of copper samples were carried out on a Dilor Visible spectrometer with 530 and 488nm laser excitation wavelengths at 2mW laser power with a ×40 objective.

2.2 Transmission electron microscopy

The resolution of a microscope is determined by the wavelength of the particles illuminating the sample. Since the wavelengths of visible light is from around 380nm to 780nm, nothing smaller than this can be observed with a conventional optical microscope. The electron microscope uses electrons instead of light, and the wavelength of an electron is approximately 5 orders of magnitude smaller than that of visible light giving a lot of zoom to improve lateral resolution. However the quality of lenses is lower for electrons which counterbalances in part their advantage.

The following equation gives the dependence of the wavelength of the electrons λ on the acceleration voltage for an electron microscope V [131]:

$$\lambda = \frac{h}{\sqrt{2m_0 eV}} \frac{1}{\sqrt{1 + \frac{eV}{2m_0 c^2}}}$$

where e is the charge of the electron, m_0 is the rest mass, $m_0 c^2$ is the rest energy.

Transmission electron microscopy (TEM) is used to characterize the structure of the material at scales from nm to hundreds of μm using an electron beam passing through a thin (about 100nm) sample. Electrons passing through and interacting with the sample are then focused on the image forming apparatus such as a fluorescent screen, photographic plate or CCD camera.

Principle of operation

TEM always consists of the following main parts: a vacuum system, an electron source, a series of electromagnetic lenses, an imaging apparatus and a sample holder.

The electron beam diverged from the source is converted by the condenser lenses, and then hits the sample, which is placed near the pole piece of the objective lens. In order to prevent the electrons in the beam from scattering on gas molecules, the specimen is kept at very low pressure in a vacuum chamber. By changing the current in the coil of the intermediate lens one can change its focal length, so that either the plane of the object being studied or the back focal plane of the objective lens will be focused on the fluorescent screen of the microscope. In the first case, we will observe a magnified image of the sample structure, in the second a diffraction pattern.

Not all electron beams emanating from the sample (the past one and several diffracted) reach the screen and participate in the formation of the image. The selection of the beam producing the image is done by the aperture located in the back focal plane of the objective lens. If an image is formed only by the direct (i.e. past) beam it is called a bright field image. In the case the aperture transmits one of the diffracted beams the image is called dark field. The intensity of the beam emerging from the sample, is determined by the scattering and absorption processes, and depends on the structure and composition of the sample, its thickness, orientation and the radiation wavelength.

Optical scheme of a transmission electron microscope

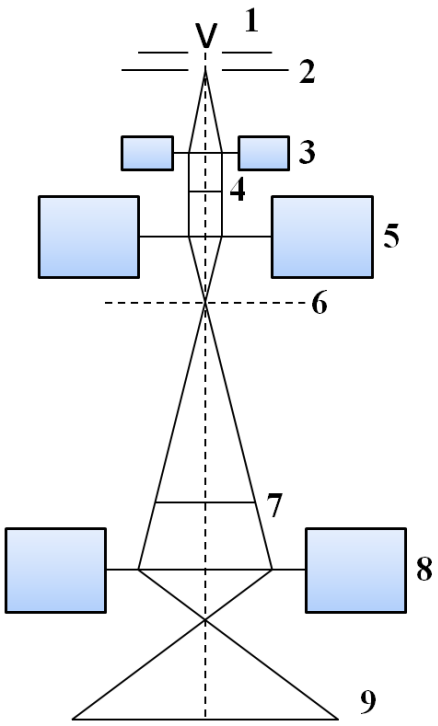

Figure 2.25. Schematic diagram of a transmission electron microscope. 1 - radiation source; 2 anode; 3 - condenser; 4 - object; 5 - objective lens; 6 - primary intermediate image; 7 - secondary intermediate image; 8 - projection lens; 9 - final image.

Schematic diagram of the TEM is shown in Figure 2.25. The cathode in the electron gun 1 emits electrons which are accelerated towards the anode 2 with a powerful electric field. Then the electrons pass through the anode hole. The resulting narrow intense electron beam is injected into the electromagnetic lenses of the TEM. After a two-stage electromagnetic focusing lens (condenser) 3 the electron beam passes through the object 4. The scattered light is then focused with the objective lens 5 that forms the primary image 6. The objective lens gives a magnification of about a 100 times. The intermediate objective lens throws an intermediate image 7 with a small increase (usually up to 10 times) to the object plane of the projection lens 8 and the projection lens forms the final magnified image 9 (the projection lens gives a magnification of up to a 100 times). Thus, the overall magnification of the electron microscope can be up to a 100 000 times.

Sources of electrons (electron guns)

There are two main types of electron guns: thermionic (thermoelectronic) and field emission (FEG). These two sources are not interchangeable. FEG provides a more monochromatic beam, but it is more expensive and less stable. In this work we used a microscope with a thermionic source.

Thermionic emission source

We can heat matter to such a temperature that the electrons can overcome the potential barrier φ, separating the surface and vacuum. This barrier is called the "work function" and is measured in volts. According to the Richardson law:

$$J = AT^2 exp(-\frac{\varphi}{k_B T})$$

where A is a material dependant Richardson's constant [A/m^2K^2], J is the current that occurs when the source is heated to a temperature T at which kBT is comparable to the potential barrier φ. However, when kBT reaches several eV, most materials either melt or evaporate. Therefore materials with high melting points or with a very low work function are used. Usually this is either a tungsten (W) filament (T_m = 3660K), or lanthanum hexaboride (LaB_6) that has a low work function. A source with a LaB_6 crystal has a cubic lattice with a <001> orientation. The W-filament is heated by an additional power source, while the LaB_6 source is usually heated by a contact with a rhenium filament which is heated resistively.

Lenses

The theory behind electron microscopes is similar to that of optical microscopes, i.e. all the methods and formulas from light optics can be directly transferred to electron optics.

One of the most important characteristics of the lens is its resolution, i.e. the possibility to resolve closely spaced features of the specimen. In other words, the resolution of the objective lens is the minimal distance between two points of the object when these points of the image are resolved as two separate points. In spite of the fact that the wavelength of an 200kV accelerated electron is 0.0025nm, the resolution of a modern electron microscope, at its best, "only" reaches around 0.1nm. This is due to the lens aberrations and diffraction effects, which widens the diameter of the beam or the image of the object, and hence reduces the resolution. The limiting resolution of the lens is determined by the diffraction properties of the lens and can be written as:

$$\varepsilon = \frac{0.61\lambda}{A}$$

where λ is the wavelength of the light used to illuminate the object, and A is the numerical aperture of the objective lens.

Parameters of transmission electron microscopes used

In this work TEM experiments were carried out on transmission electron microscopes Philips CM20 and CM30 (LaB_6 filament: φ=2.5eV, T=2000K) with accelerating voltages 120kV and 150kV, respectively. For TEM measurements all samples were placed in an epoxy matrix and cross sections were cut with ultra microtom equipped with a diamond knife in 100nm thick slices. The slices were placed on Cu grids with a holey carbon film.

2.3 Small-angle neutron and X-ray scattering

Small-angle neutron (SANS) and X-ray (SAXS) scatterings are widely used diffraction methods for studying the spatial structure of matter at a scale of about 1 – 600nm (100nm for X-ray) [132].

In the diffraction theory proposed by W.L. and W.H. Bragg in 1912 a crystal is considered as a set of discrete reflection planes separated by a distance d. The incident monochromatic X-ray or neutron beam would produce a Bragg peak if its reflections off the various planes interfered constructively. This condition can be expressed by Bragg law:

$$n\lambda = 2d \sin\theta$$

where λ is the wavelength of the monochromatic beam, 2θ is the scattering angle and n is an integer. A visualization of Bragg's law is presented in Figure 2.27.

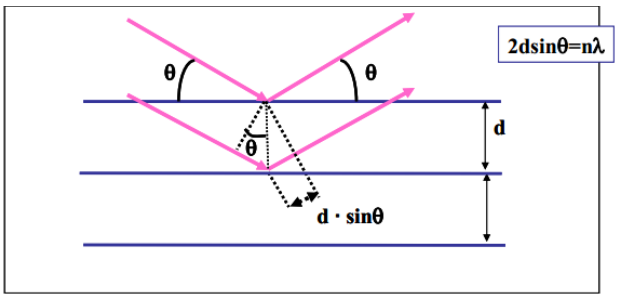

Figure 2.27. Scheme to derivate the Bragg law. Monochromatic beam (arrows) is reflected by crystallographic planes separated by a distance d [133].

When the investigated sample is a single crystal then the diffraction pattern consists of a series of spots any of them related to a particular plane in the crystal lattice [134]. In the case of a polycrystalline state the diffraction spots transform into circles due to the different orientation of the crystallites in the sample. A scheme of a neutron scattering experiment is shown in Figure 2.28.

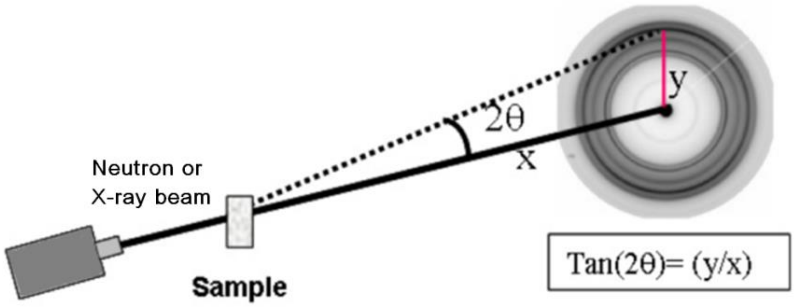

Figure 2.28. Scheme of a diffraction experiment. Knowing the sample to detector distance (x), the wavelength of the beam (λ) and the position of a given diffraction ring (y) the scattering angle can be calculated as the arc tan(y/x). The different diffraction maxima following a radius (y-direction) can be represented as plots of the intensity versus the q-vector [133].

When a beam reaches the sample the diffracted intensity is collected by a detector (photographic film, CCD camera etc). By knowing the experimental conditions (sample to detector distance, size of the detector, wave length of the beam) the diffraction pattern can be obtained as a graphic of the diffracted intensity versus the q-vector ($q=4\pi\sin(\theta)/\lambda$). The representation versus the q vector is suitable for two reasons. On the one hand, it allows one to represent the scattered intensity as a function of a wavelength independent magnitude. In this way diffraction patterns recorded by using radiation of different wavelength (X-ray, neutrons, light, etc.) can be easily compared. On the other hand, as derived from the Bragg law, those q values at which a peak in the intensity is observed should correspond to diffracting crystalline planes separated by a distance $d=2\pi/q$.

In typical crystalline substances the crystalline planes are separated by distances in the range of 0.1-1nm. However, soft condensed matter, in general, includes a great variety of complex materials which frequently present a hierarchical structure ranging from tenths to hundreds of nanometers. Depending on the sample to detector distance different length scales can be probed or, in other words, different scattering angles can be accessible. For $2\theta > 1°$ the diffraction experiment is referred to as wide-angle scattering. For $1°>2\theta >0.3°$ one speaks about medium-angle scattering and for $2\theta <0.3°$ of small-angle.

Figure 2.29 shows an example of a radial intensity profile of a pattern in one dimension for a MWNT [133]. One can see a peak corresponding to the ring appearing at $q=18nm^{-1}$ characteristic of the 002 reflection from the graphite layer structure. This value leads to a spacing value of $d=2\pi/q_{max}=0.35nm$ for the distance between the walls of the CNT.

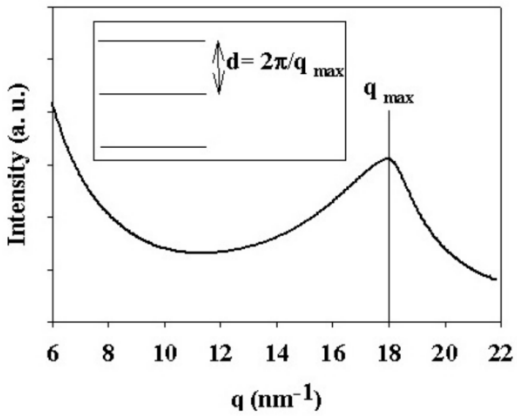

Figure 2.29. Radial intensity profile of the pattern in one dimension revealing the presence of the 002 reflection of the graphite layer structure [133].

A typical carbon nanotube sample consists of micron-size bundles, in which from some tens to some hundreds of single nanotubes self-assemble in a two-dimensional hexagonal lattice held together by van der Waals interaction. Figure 2.30a presents a TEM image of a characteristic bundle of SWCNTs [133]. The diffraction of such a hexagonal lattice of carbon nanotubes appears mainly due to the characteristic (1 0) planes schematized in Figure 2.30a. Figure 2.30b showed a diffractogram of such a bundle. The diffractogram exhibits a shoulder at $q\approx4.4nm^{-1}$ corresponding to the characteristic (1 0) reflection of a closely-packed two-dimensional hexagonal lattice and several maxima at higher q values corresponding to other reflections from the

hexagonal packing. The spacing value d=2π/q≈1.4nm is closely related to the tube diameter. However, the peaks are broad as fluctuations of the lattice constant induced by tube diameter polydispersity are expected. The (1 0) peak in the raw data is affected by a strong continuous scattering due to the contribution of nanoparticles of different carbonaceous species and of nanovoids.

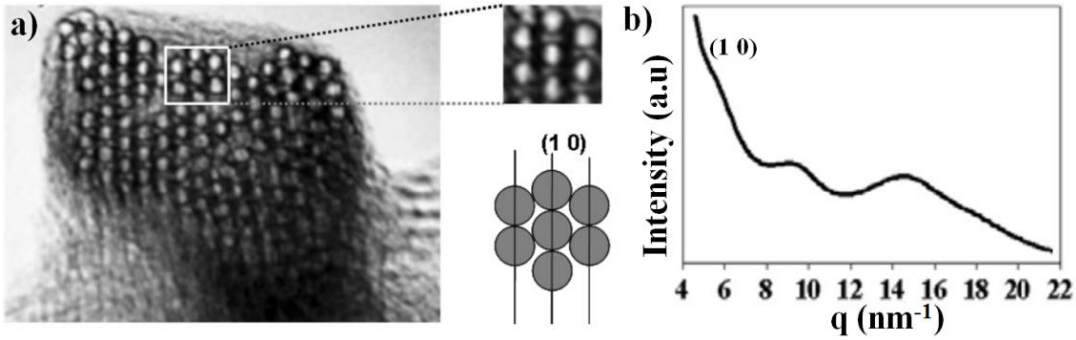

Figure 2.30. a) TEM image of a characteristic bundle of SWCNTs. Scheme shows the characteristic planes of the two dimensional hexagonal lattice
b) diffractogram of a SWNT bundle.

To probe the dispersion of CNTs in the polymer matrix small-angle scattering is used, since it gives access to larger scales. When carbon nanotubes are introduced into a polymer they form a branched network that can be regarded as a fractal object. A fractal is defined as a self-similar object over a range of sizes. Scattering experiments in fractals have shown that the scattering intensity follows a power law:

$$I(q) \propto q^{-\alpha}$$

Values of α=1, 2, 3 are expected when the scattering objects are rods, discs and spheres respectively [135]. Intermediate cases 2<α<3 are characteristic of objects possessing a fractal geometry. Accordingly, if one had individual carbon nanotubes, or individual rod-like bundles, then a scattering experiment should provide an exponent α=1 (Figure 2.31). The results are plotted in a double logarithmic scale to emphasize the power law behavior.

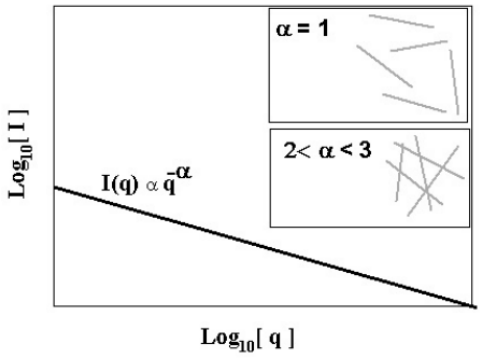

Figure 2.31. The scattered intensity by a fractal follows a potential law on q. Exponents α=1 are expected when the scatterers are individual rods. Exponents 2<α<3 are expected for rod aggregates [133].

Figure 2.32 represents a collection of model structures and the resultant small-angle scattering. R_g is the radius of gyration [135].

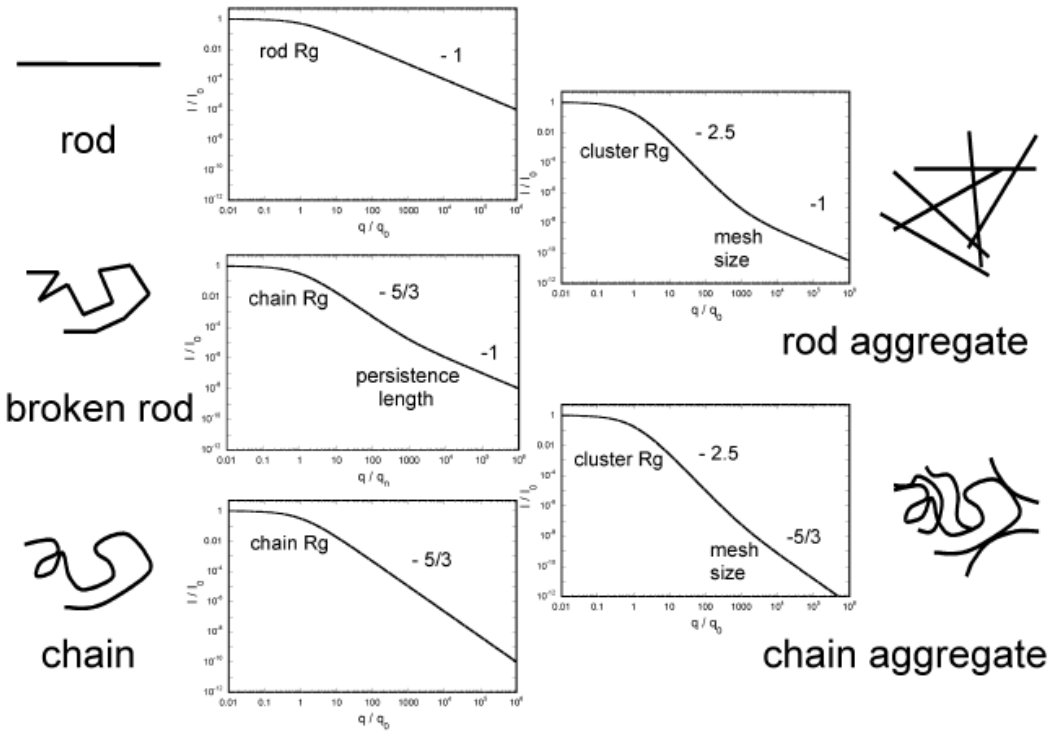

Figure 2.32. Power law scattering from fractal objects. I_0 is the maximum intensity, q_0 is a characteristic value of the intermolecular distance used to normalize the q-vector. [135].

For SWNTs dispersed in liquids values of $\alpha \approx 2\text{-}2.5$ were found by [135] [136] [137] indicating that SWNTs were not dispersed down to single nanotubes but formed a mass fractal consisting of CNT agglomerates.

To obtain information about CNT dispersion in a polymer composite one needs to perform two diffraction experiments: 1) from the composite 2) from the pure polymer. Subtraction of the second one from the first one will give the data corresponding to the nanotube network.

X-ray and neutron diffractions have a lot of features in common, but they also exhibit essential differences, such as [138]:

- Energy: of the order of 10keV for X-rays, of the order of 10meV for neutrons. This has an important consequence for the study of atomic motions.
- Magnetic moment: in contrast to X-rays, neutrons have a magnetic moment, allowing the use of neutrons to study magnetic structure of materials.
- Cross sections: whereas the X-ray atomic scattering factor increases smoothly with atomic number, the neutron cross section varies strongly among elements and isotopes. Thus hydrogen is almost invisible to X-rays and scattering from heavy atoms can often overwhelm the scattering from the rest of the material. This difficulty can be advantageously avoided with neutron diffraction. (Figure 2.33)

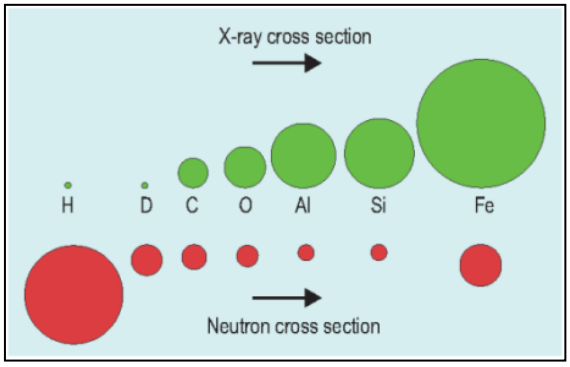

Figure 2.33. Neutron and x-ray scattering cross-sections [139].

In this work neutron scattering was chosen, since it gives an access not only to the dispersion of CNTs but also allows probing the polymer structure due to the presence of hydrogen atoms in PEEK.

Experimental conditions

SANS measurements were performed on the LOQ and SANS2D diffractometers at the ISIS Facility, Oxfordshire, UK [140]. These are 'white-beam' time-of-flight instruments covering scattering vector ranges of $0.009 \leq q \leq 1.2$ Å^{-1} (0.5m & 4m sample-detector distances, wavelengths $2.2 \leq \lambda \leq 10$ Å) and $0.0015 \leq q \leq 0.19$ Å^{-1} (12m sample-detector distance, 150 mm detector offset, wavelengths $1.5 \leq \lambda \leq 12.5$ Å), respectively, where $q = 4\pi/\lambda\sin(\theta/2)$ and θ is the scattering angle. Being a spallation neutron source, the instrument is not monochromatic. It is operated in time-of-flight mode, which means a polychromatic beam of neutrons is delivered to each instrument and then the wavelengths arriving at the detector are time-sorted. Each raw scattering data set was corrected for the detector efficiencies, sample transmission and background scattering and converted to scattering cross-section data ($\partial\Sigma/\partial\Omega$ vs. q) using the instrument-specific software [141]. The data were placed on an absolute scale (cm^{-1}) using the scattering from a standard sample (a solid blend of hydrogenous and perdeuterated polystyrene) in accordance with established procedures [142].

Chapter 3

Results and discussion

3.1 CNT@copper composite

Incorporation of DWNTs into copper was found to improve the mechanical properties of the metal, in particular, the wear resistance. In this part we perform a detailed Raman spectroscopy study outside and inside the wear tracks, in order to shed light on the role and the state of the CNTs.

3.1.1 Sample preparation

The DWNT/Cu composites were prepared at the Centre Inter-universitaire de Recherche et d'Ingénierie des Matériaux (CIRIMAT) by the group of Prof. Christophe Laurent. The CNT/Cu powder containing 5 vol.% of DWNTs was prepared by a rapid mixing route involving short-time sonication and freeze-drying. Oxidative acidic treatment or ball-milling were not used in order to avoid damaging of DWNTs. DWNTs were dispersed in deionized water with a sonotrode for a few seconds, after which the Cu powder was added. The ultrasonic agitation was then maintained for one minute. The vessel containing the DWNT/Cu suspension was immersed in liquid N_2 for

two minutes and was freeze-dried at -40°C (Christ alpha 2-4 LD, Bioblock Scientific) for 48h in a primary vacuum (12 Pa). The DWNT/Cu powder was densified by Spark Plasma Sintering (SPS) (Dr Sinter 2080, SPS Syntex Inc., Japan). It was loaded into a 20mm inner diameter graphite die. A sheet of graphitic paper was placed between the punch and the powder as well as between the die and the powder for easy removal. The powder was sintered in vacuum (residual cell pressure < 10Pa). A pulse pattern of twelve current pulses followed by two periods of zero current was used. A heating rate of 100°C/min from room temperature to 700°C, where six minutes dwell was applied. A uniaxial charge (corresponding to 100MPa) was gradually applied within the first minute of the dwell at 700°C and maintained during the remaining five minutes. We do not expect large interfacial reactions between copper and CNTs since the fabrication temperature is lower than that used in graphene and CNT synthesis (~1000°C) [143]. Natural cooling was applied down to room temperature. The uniaxial pressure was gradually released during cooling. The sintered specimen was in form of a pellet 20mm in diameter and about 2mm thick. The pellet was polished down to 0.25µm using diamond powder.

3.1.2 Microhardness and tribological testing

Microhardness and tribological tests were performed in collaboration with Dr. Christophe Guiderdoni at the CIRIMAT.

The indentation and friction tests revealed a higher microhardness and a lower friction coefficient for the DWNT/Cu composite than for pure copper (Table 3.1).

Wear tests were performed in rotary mode (constant speed equal to 2cm/s) using a 10N load. Flat-surfaces of Cu and DWNT/Cu samples 20mm in diameter were rubbed against a 100C6 steel ball 6mm in diameter. After wear tests were performed, the half-width r of the wear track was measured from white-light interferential rugosimetry images (Figure 3.1).

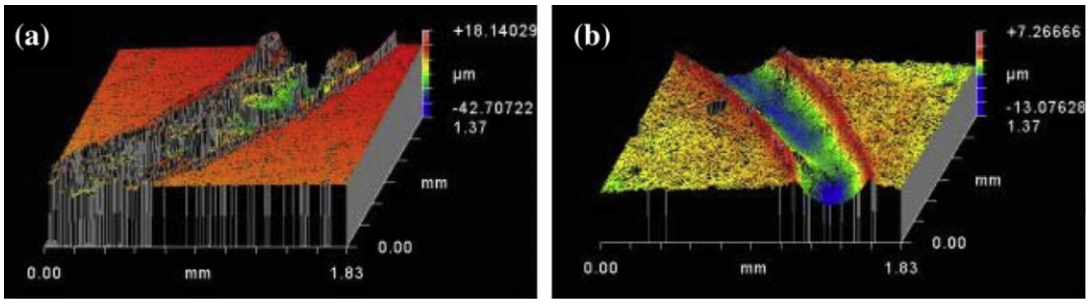

Figure 3.1. White-light interferential rugosimetry images of the wear track for a) Cu and b) DWNT/Cu composite [144].

The wear tracks on Cu (Figure 3.1a) reveal important wear, contrasting with what is observed for DWNT/Cu composite (Figure 3.1b). The outer radius of the circular track L is equal to 4mm. Dark areas in the images correspond to areas not accessible to the white-light beam and therefore are deeper than the areas colored in blue. This corresponds to Cu samples showing high wear volume.

The wear volume *Vw* was calculated for a half-ellipse track according to:

$$V_W(mm^3) = \frac{1}{2}\pi r d \cdot 2\pi L$$

where r = track half-width (mm), d = track depth (mm), L = outer radius of the circular track (4mm). The load-normalized wear rate W was calculated according to:

$$W\left(\frac{mm^3}{m}\cdot N\right) = V_W/(L\cdot F)$$

where L = sliding distance (15m), F = applied normal load (10N)

Table 3.1 summarizes the mechanical properties of DWNT/Cu composite and pure copper. One can see that DWNT/Cu composites present a higher microhardness, a lower friction coefficient and lower wear and wear rate against steel (by a factor of 10) compared to pure Cu.

Properties	Cu	DW/Cu
Vickers microhardness	50	82
Friction coefficient (for 5N load)	0.78	0.24
Wear volume (mm^3)	0.45	0.044
Wear loss (mg)	4.03	0.36
Load-normalazed wear rate (mg/m·N)	0.027	0.003

Table 3.1. Properties of Cu and DWNT/Cu composite.

A preliminary analysis of the worn surface of the steel ball found Cu and carbon transfered on the ball. Field Emission Scanning Electron Microscopy (FESEM) observation of the worn surface revealed grooves, scars and plastic deformation of Cu, suggesting abrasive and adhesive wear, reflecting that Cu grains wear out and that the subsurface is freshly exposed to the steel counter face. Similar results were reported by several authors [42] [43] [44] [45]. To reveal the modifications of the structure of the composite we studied the wear tracks by Raman spectroscopy.

3.1.3 Raman spectroscopy

The Raman spectra have been conducted on an Xplora spectrometer in backscattering geometry and using 632nm laser excitation. The laser power was fixed to 1mW and we used a ×50 objective. For Stokes/Anti-Stokes measurements, we have used a Dilor spectrometer with the same experimental conditions. Figure 3.2 shows two typical Raman spectra for the DWNT/Cu composite inside and outside the wear area. Outside the wear area, we observe a large background signal, while inside the wear area the background signal is considerably reduced and the CNT spectral bands are more intense.

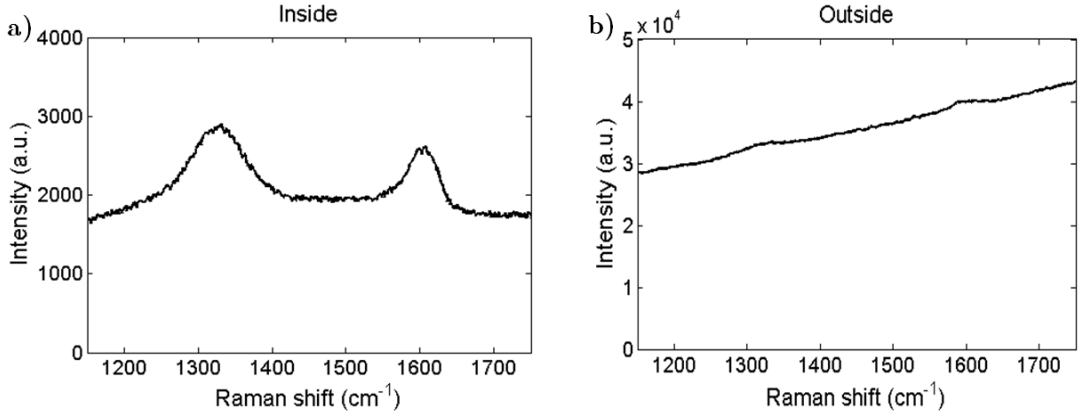

Figure 3.2. Typical Raman spectra without background subtraction a) inside and b) outside the wear area.

In order to understand the origin of the background signal and in particular to understand whether it is Raman signal, we have recorded the Raman Stokes and anti-Stokes spectra at different excitation wavelengths (Figure 3.3).

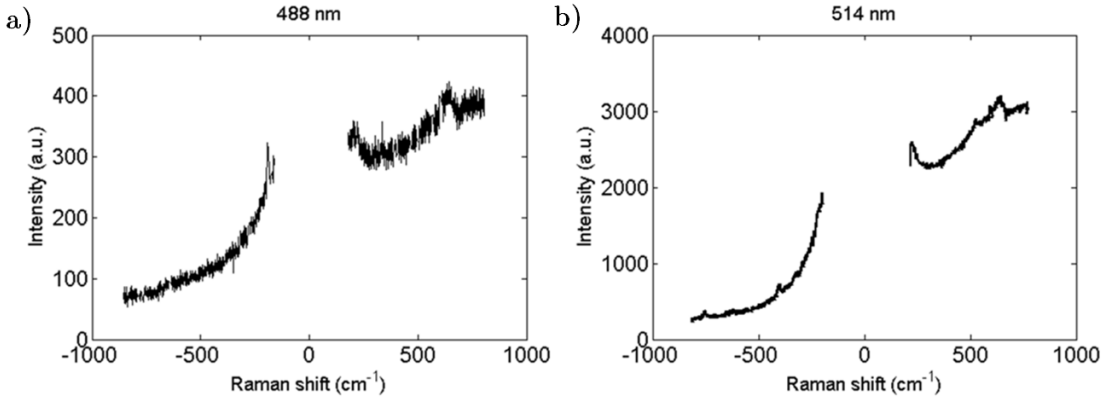

Figure 3.3. Raman Stokes and anti-Stokes spectra at different excitation wavelengths a) 488nm and b) 514nm.

The Stokes signal is proportional to n(ω)+1, while the anti-Stokes signal is proportional to n(ω):

$$\frac{I_S}{n+1} = \frac{I_{AS}}{n}$$

where $n(\omega, T) = \frac{1}{\exp\left(\frac{\hbar\omega}{k_B T}\right)-1}$ is the Bose-Einstein population factor. This relation is satisfied regardless of the order of the implied scattering process (Figure 3.4) [145].

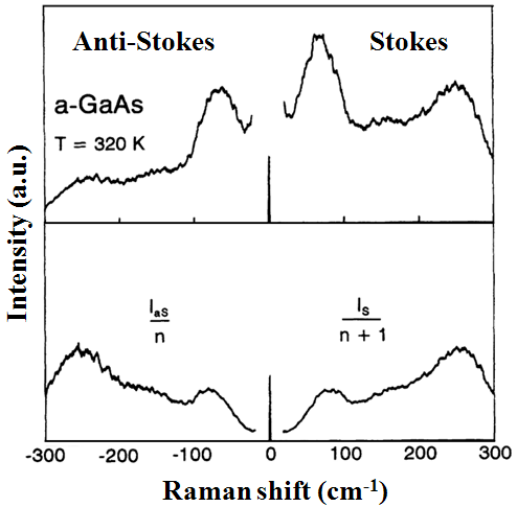

Figure 3.4. Low-frequency Raman spectrum of a-GaAs at T=320K a) Experimental Stokes and anti-Stokes spectra b) Reduced spectra [145].

The temperature can be estimated by taking the relative intensity of the Stokes and anti-Stokes spectra using the following equation [95]:

$$T = \frac{\hbar\omega}{k_B} \ln \frac{I_S}{I_{AS}}$$

For our sample we deduced the temperatures of 500-700K inside and outside the wear area depending on location when considering the 300-700cm^{-1} spectral range (Figure 3.5).

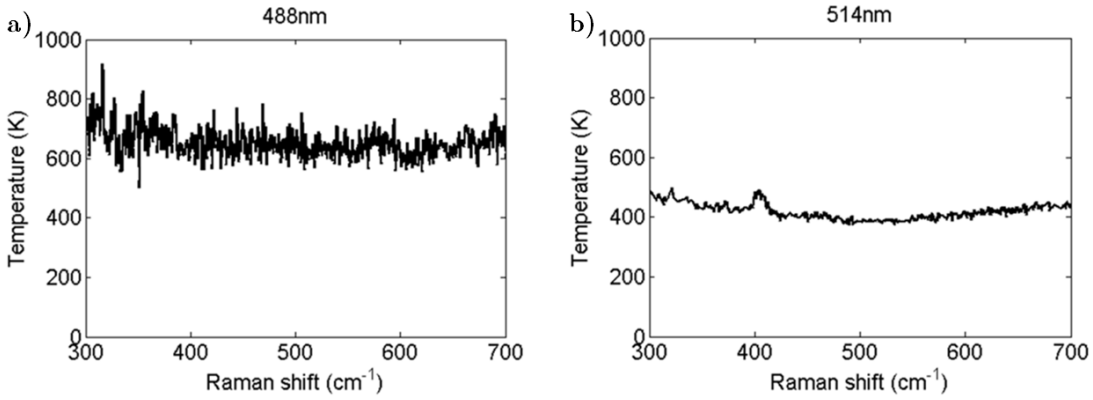

Figure 3.5. Temperatures deduced from Stokes/Anti-Stokes measurements with different wavelengths a) 488nm b) 514nm.

No change in the background signal is observed when using the 514nm and 488nm laser excitation. This shows that the background signal is not caused by luminescence but by inelastic scattering with phonons and electrons. The higher background signal in non-worn areas is attributed to the presence of a larger fraction of Cu. The smaller background signal and higher intensities of the Raman bands thus show that the fraction of CNTs is higher in the wear area.

DWNT have a characteristic G-band line shape due to inner and outer tubes [146]. The line width and intensity of the G-band in the friction wear area indicates that the CNTs are still intact and are not transformed in disordered forms of three folded carbon.

We noticed that when fitting the spectrum with a single Lorentzian line shape in the spectral range of the G-band, the spectrum shifts in a way inconsistent with spectral shifts of the D band. So we recall that pristine DWNTs show a G_i^+ band from the inner tube located at 1581cm^{-1} and a G_o^+ band from the outer tube located at 1592cm^{-1} (Figure 3.6). We took spectra with two different excitation wavelengths (532nm and 632nm) to understand the origin of the higher contribution to the G band.

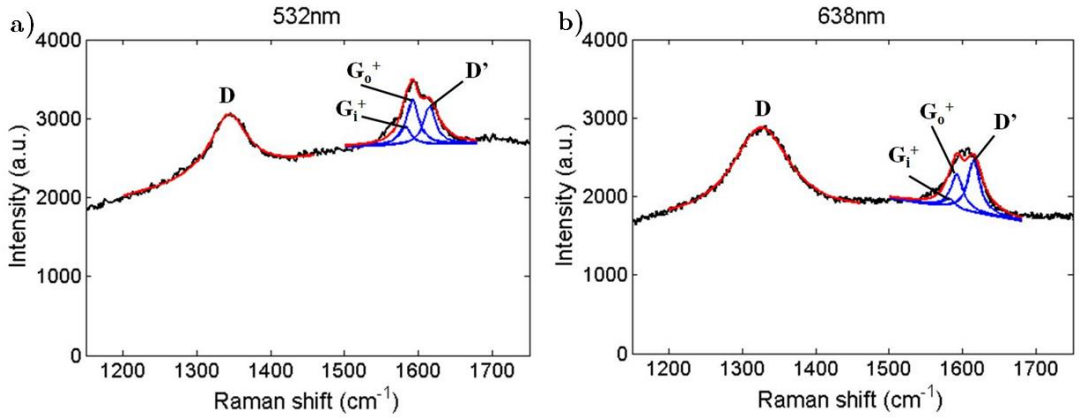

Figure 3.6. Raman spectra of DWNT/Cu composite inside the wear area taken with different wavelengths a) 532nm and b) 638nm.
The DWNT Raman signal is composed of the defect induced D and D' bands and the G-band. The G-band has contributions from both inner and outer tubes (G_i^+, G_o^+).

We find that the higher contribution, D', increases in intensity comparatively to the G band with exciting wavelength. Consequently, this band is not caused by the same process that the G band and should not be attributed to the G_o^+ contribution and large charge transfer.

We used a 638nm laser excitation wavelength, since the D and D' band intensities are larger when compared to those obtained with smaller wavelengths [147] which makes it easier to separate the D' band from the G^+ bands. Raman images of size 100μm×100μm were recorded on the surface area shown in Figure 3.7. Raman spectra were recorded every 5μm with focal spot size of 2μm. We have fitted all the Raman spectra obtained from a Raman map and decided to fix some parameters in order to reduce uncertainties. So, we fixed the line widths and the spectral positions. As a consequence, the fits are not perfect but the free parameters are reduced to the intensities of each contribution. Overall the whole shape is reproduced quite well.

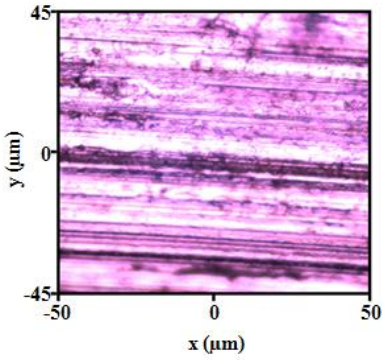

Figure 3.7. Optical image of the wear area where the Raman measurements were performed.

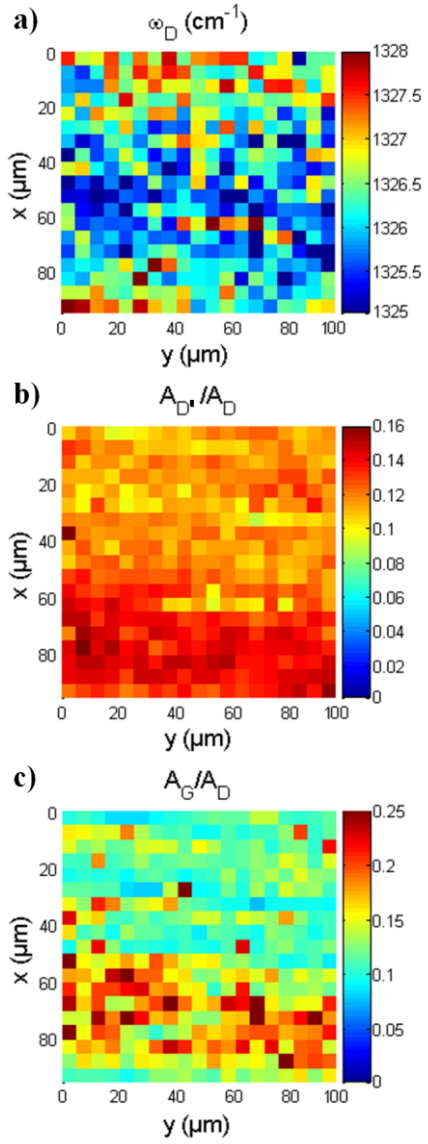

Figure 3.8. Raman maps (100×100 micrometers) within the wear area a) wavenumber position of the D band b) relative intensity of the D' band ($A_{D'}/A_D$, using integrated intensity) and c) the G-band (A_G/A_D, using integrated intensity).

As the D band is a simple Lorentzian, we can determine its spectral position and intensity. We finally can compare the integrated intensities. We have plotted the spectral position of the D band, the ratio of the D'/D integrated intensities ($A_{D'}/A_D$) and D/G integrated intensities (A_D/A_G) in Figure 3.8. Recently, it has been shown that the ratio of the integrated intensities $A_{D'}/A_D$ could be an indication of the type of defects. A small $A_{D'}/A_D$ ratio is due to sp^3-defects, an intermediate $A_{D'}/A_D$ ratio to vacancies and a large $A_{D'}/A_D$ to large structural defects [117].

When scanning the laser spot over the surface (100μm×100μm) we find that the D band shifts slightly inside the friction wear area indicating residual stress variations (Figure 3.8a) and the shift of the D band is correlated with the increase of the relative intensity of the D' band (Figure 3.8b).

We note that the D (D') can be explained by inter valley (intra valley) double resonant processes [148]. The D' intensity is believed to increase with stronger interlayer interaction (sp^3 versus edge). This small increase of the D' can thus be attributed to a reduction of the interlayer spacing consistent with a smaller residual stress (extension). The A_G/A_D is really small indicating a large number of defects (Figure 3.8c). Further work is required to confirm this interpretation.

3.1.4 Conclusions

Raman spectroscopy reveals that Cu is removed and the amount of carbon material is higher in the friction wear area. We conclude that this carbon material is still in the form of carbon nanotubes with intact cylindrical shape although intense wear increases the number of defects in the CNTs. Destroyed carbon nanotubes would show a much broader G band. Typically, the G band broadening increases for size domains lower than 10nm. If the nanotubes are broken, the size domain should be of the order of the circumference, i.e. around $2\pi r = 6$nm.

3.2 CNT@PEEK composite

In this part we investigate the origin of the mechanical modifications of a poly (ether ether ketone) beam electrically modified with multi-walled carbon nanotubes. We use differential scanning calorimetry, nano-indentation, extended Raman imaging, and small-angle neutron scattering to correlate rupture and hardness variations with the changes in carbon nanotube concentration. Statistical analysis of the relative spectral intensities in the Raman image is used to estimate local tube concentration and polymer crystallinity.

3.2.1 Sample preparation

The samples were prepared from poly (ether ether ketone) (PEEK) of grade 2000 supplied by Evonik Degussa GmbH in the form of fine powder (the properties of PEEK are summarized in Table 3.2).

Property	Value
$Density_{25°C}$ (g/cm)	1.2
Molar mass (g/mol)	25,000
T_m (°C)	340
T_g (°C)	155
Size of powder particles (μm)	500
Elastic limit (yield strength) (MPa)	100
Elastique modulus (MPa)	3700
Electrical conductivity (S/cm)	10^{-14}
Viscosity (Pa·s)	273

Table 3.2. Properties of PEEK Evonik (data from Evonik).

MWNTs Graphistrengh® were supplied by Arkema and used without further purification (the properties of the tubes are summarized in Table 3.3).

Property	Value
Purity (%)	90
Number of layers	5-15
Average diameter (nm)	10-15
Length (μm)	0.1-10
Young's modulus (GPa)	1200
Tensile strength (GPa)	150
Density (g/cm^3)	2.6
Thermal conductivity (W/m·K)	3000
Electrical conductivity (S/cm)	10^3-10^5

Table 3.3. Properties of Arkema MWNTs (data from Arkema).

CNTs are initially highly entangled as it can be seen in the TEM image (Figure 3.9).

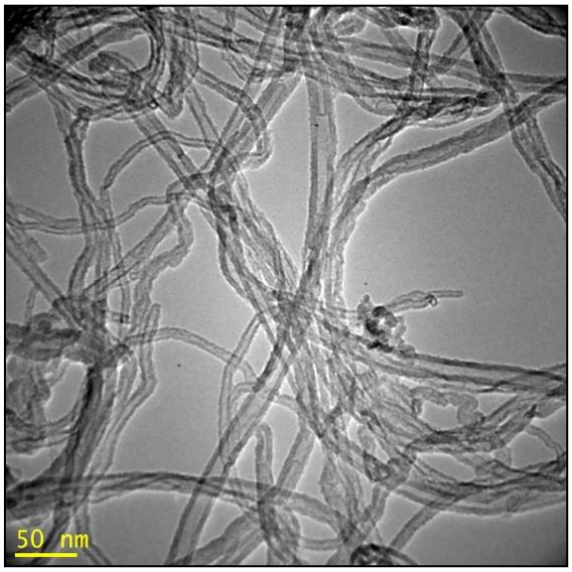

Figure 3.*9. Typical TEM image of Arkema MWNTs.*

A typical Raman spectrum of Arkema MWNTs is presented in Figure 3.10. The D band is relatively intense which indicates the presence of defects.

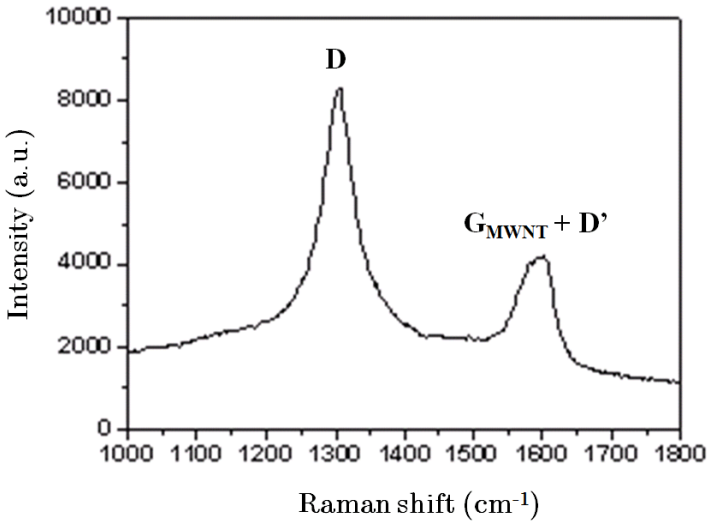

Figure 3.10. Typical Raman spectrum of Arkema MWNTs (λ=785nm).

The MWNT/PEEK composites were prepared by Dr. Matthieu Guehenec at the Institut Pluridisciplinaire de Recherche sur l'Environnement et les Matériaux (IPREM). The PEEK powder was at first dried in an oven at 140°C during 6 hours to remove moisture. It was then mixed with 0.5, 1 and 2wt% of MWNTs to form a homogeneous mixture. This mixture was placed into the volumetric hopper feeder specifically designed to contain aerosols. The melt compounding was performed in a co-rotating twin screw extruder from LABTECH engineering company LTD with a

ratio L/D equivalent to 40, a screw diameter of 16mm with 10 different heating zones and a die diameter of 2mm. The extruder screw profile is assembled from modular screw elements, including transporting elements, kneading and mixing elements. The screw design with a high shear screw profile is shown in Figure 3.11. The maximum temperature was set at 390°C, and an asymmetric temperature distribution was used. The temperature profile is shown in Table 3.4.

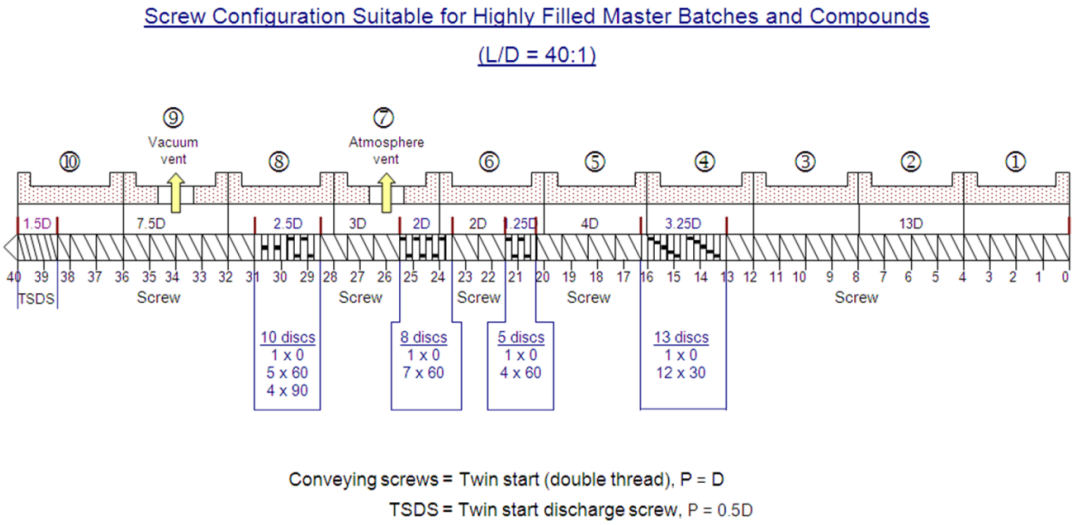

Figure 3.11. Screw profile with the mixing zone used for the study.

Zone	Die	9	8	7	6	5	4	3	2	1
Temperature (°C)	370	380	385	390	390	390	385	380	370	360

Table 3.4. Temperature Distribution in Twin Screw Extruder.

500g of PEEK with MWNTs were extruded at rotor speeds of 400 rotations per minute (rpm) with a constant throughput of 1kg/h. The material leaving the extruder was cooled down in a temperature regulated water bath and then pelletized. The extruded pellets were dried at 140°C in air. The pellets were molded for the rheological measurements by compression at 380°C to obtain disks with a diameter of 25mm and a thickness of 2mm. Samples for TEM, Raman, and nano-indentation where prepared from 3g of the extruded material in the form of dried pellets.

Scanning Electron Microscopy was performed on the surfaces of the samples. Figure 3.12 shows typical SEM images of PEEK only and PEEK with 0.5wt% of MWNTs. Some polymer filaments can be noticed in pure PEEK. It is important not to confuse them with CNTs.

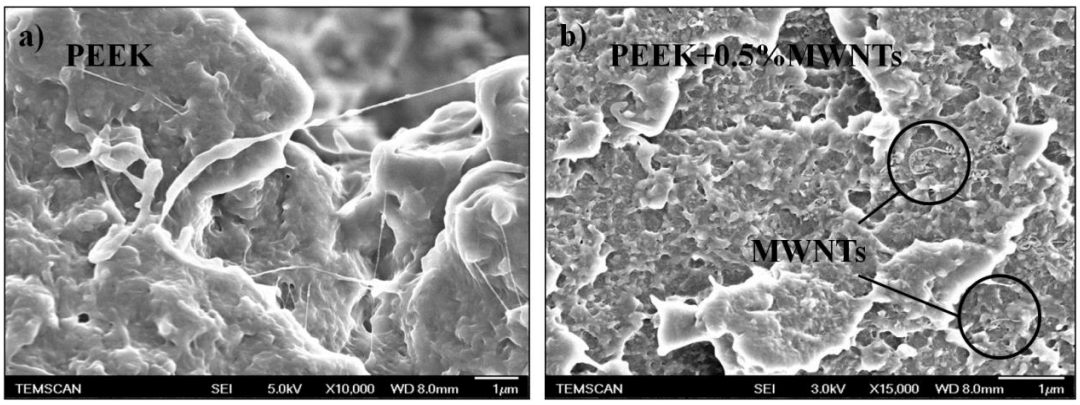

Figure 3.12. SEM images of a) PEEK only and b) PEEK+0.5wt% MWNTs taken at TEMSCAN with JEOL JSM 6700F. The images were obtained by Dr. François Boyer.

Figure 3.13 illustrates the electrical conductivity measurements done in collaboration with Dr. Matthieu Guehenec at the IPREM. These measurements were performed on thin films (average thickness 200μm). The electrical conductivity increases by more than eight orders at 0.5wt% of CNT and stabilizes at 2wt% indicating the percolation threshold at ~0.65wt%.

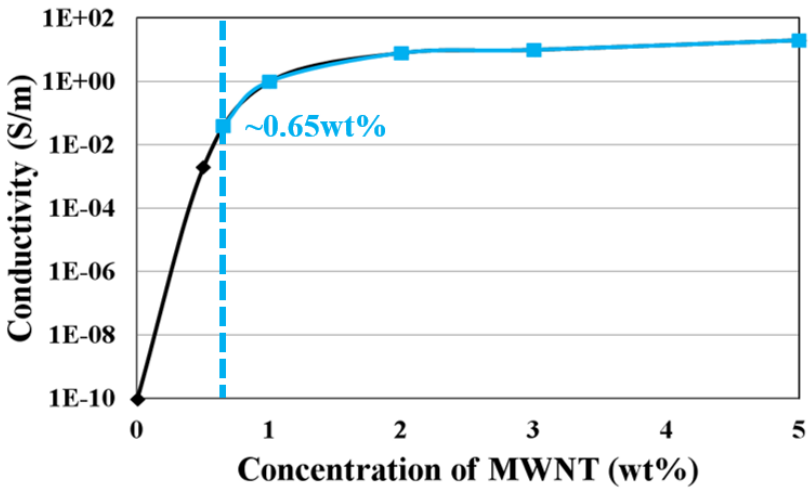

Figure 3.13. Dependence of the electrical conductivity on the content of MWNTs.

3.2.2 Tensile strain measurements

The tensile strain measurements have been carried out in collaboration with Dr. François Boyer at the Institut Clément Ader (ICA).

The beams after the tensile tests are shown in Figure 3.14.

Figure 3.14. Test beams after the tensile measurements a) PEEK b) PEEK with 1wt% of CNTs.

Figure 3.15 shows the stress strain curve for PEEK composites containing 0.5-3.0wt% of CNTs and the PEEK matrix without CNTs. The introduction of MWNTs into PEEK results in drastic change in the PEEK mechanical behavior.

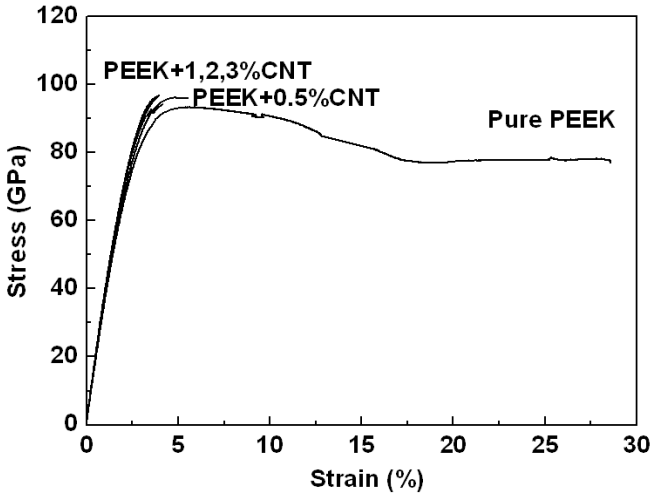

Figure 3.15. Stress/stain curves for MWNT/PEEK composites with different amounts of CNTs and for pure PEEK.

The behavior of PEEK changes from ductile ($\varepsilon_{fracture}$= 28.6%) with no tubes to semi-brittle ($\varepsilon_{fracture}$= 5%) when filled with 0.5wt% of MWNTs. The modification of the ductile regime with filler particles in PEEK have also been observed for CNF [149] and SiO_2 nanoparticules [150]. The tensile modulus (E) average value increases by 7% between PEEK without tubes and with 2wt% of MWNTs. The ultimate tensile stress value at sample break (σ_t^{ult}) goes up from 78MPa for PEEK without tubes to 96MPa with 0.5wt% of MWNTs. Once filled with MWNT the nanocomposites exhibit ultimate tensile stress values laying between 88 and 96MPa independent of the amount of MWNT present in the composite.

3.2.3 Differential scanning calorimetry

The DSC measurements have been carried out in collaboration with Dr. François Boyer at the Institut Clément Ader (ICA).

Table 3.4 shows the crystallization X_c calculated from the peak enthalpies normalized by the actual weight fraction of PEEK:

$$X_c = \frac{\Delta h_c}{\Delta h_c^0 \ W_{polymer}} \times 100$$

Δh_c^0 is 130 J/g [151] and $W_{polymer}$ is the weight fraction of the polymer-matrix. Experiments were conducted from a sample taken at the edge and the centre of the beam. The measurements show that the amount of crystallinity is about the same (32%), independently of CNTs content (Table 3.4). It has been shown that the presence of carbon fillers (i.e. short fibers) changes the mechanical behavior irrespective of the crystallinity of the PEEK matrix [152]. The measurements here show that the amount of crystallinity (32%) is the same in the volume of beam and between the core and the outer surface (edge) of the beam. This is consistent with reports which showed that the presence of CNTs increases the crystallization temperature of PEEK but does not influence the crystallinity [153]. We conclude therefore that the reduction of the ductile regime is not caused by any increased polymer crystallinity.

Sample	X_c (%) Centre	X_c (%) Edge
Pure PEEK	31.5±1.4	31.6±0.5
PEEK 0.5% CNT	33.1±1.8	32.9±1.9
PEEK 1% CNT	31.6±2.0	31.4±0.6
PEEK 2% CNT	33.7±1.1	31.0±1.2

Table 3.4. Degree of crystallinity of PEEK nanocomposite.

3.2.4 Nano-indentation

The nano-indentation measurements have been carried out in collaboration with Dr. François Boyer at the Institut Clément Ader (ICA).

The elastic reduced modulus, E_{IT}^*, is determined by:

$$E_{IT}^* = \frac{\sqrt{\pi}}{2} \cdot \frac{S}{\sqrt{A_p}} \quad \text{or} \quad \frac{1}{E_{IT}^*} = \frac{(1-\nu^2)}{E_{IT}} + \frac{\left(1-\nu_i^2\right)}{E_i}$$

where subscript i corresponds to the specific properties of the indenter, ν is the Poisson's ratio, A_p is the residual area and S is the stiffness of the contact. The manufacturer gives for the intender: $\nu_i = 0.07$ and $E_i = 1141$GPa.

To see whether fracture is caused by inhomogeneous distribution of CNTs in the polymer, we have carried out micro-indentation experiments at the edge and at the core of the samples (Figure 3.16).

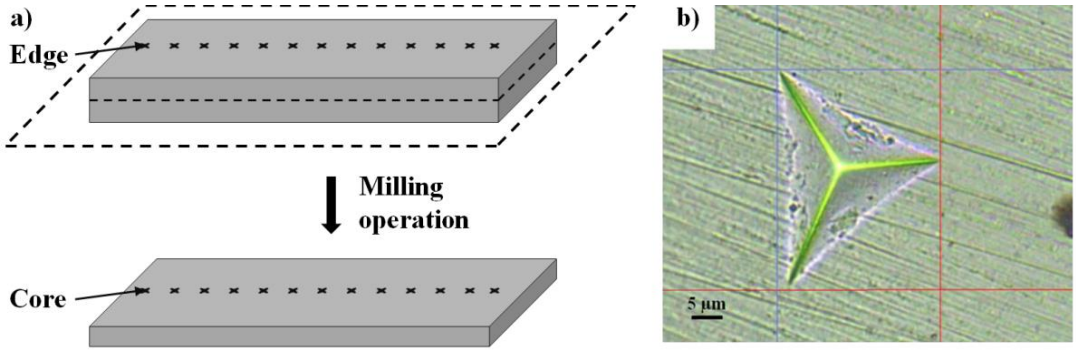

Figure 3.16. a) Locations on the beam where nano-indentation measurements were performed: at the edge and at the core
b) example of residual indent on sample surface.

The measured micro-hardness on the two sets of samples is shown in Table 3.5. The measurements reveal that the edges are less hard than the core of the composite. The micro-hardness varies by 10-15% between the core and the edge of the beam. We have verified that PEEK without CNTs shows no difference in hardness at the edge and the core of the beam. This result suggests that the variation in hardness is caused by variation in the CNT content within the beam.

Sample	Edge micro-hardness (GPa)	Core micro-hardness (GPa)
Pure PEEK	4.16±0.07	4.16±0.07
PEEK 0.5%	4.00±0.05	4.52±0.05
PEEK 1%	3.86±0.05	4.34±0.05
PEEK 2%	3.92±0.15	4.58±0.15

Table 3.5. Micro-hardness at two positions.

3.2.5 Raman spectroscopy

We have used Raman spectroscopy to determine directly the CNT content at different locations of the beam. Four samples with different amounts of nanotubes (0, 0.5, 1 and 2wt%) in a polymer matrix were cut parallel with respect to the direction of the extrusion. Figure 3.17 shows the locations where Raman images were recorded.

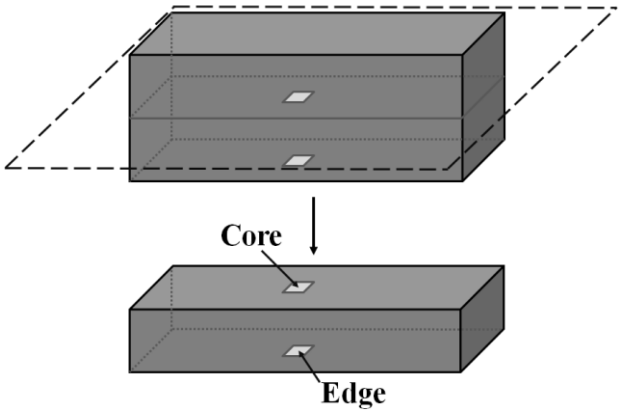

Figure 3.17. Locations on the beam where Raman measurements were performed: in the middle of the bar at the core and at the edge.

To determine the amount of CNTs at two different places, we recorded Raman images of size 400μm × 400μm. Raman spectra were recorded every 4.6μm with focal spot size of 1μm (84×84=7056 spectra). Figures 3.18a-b show examples of Raman spectra obtained for pure PEEK and PEEK with CNTs.

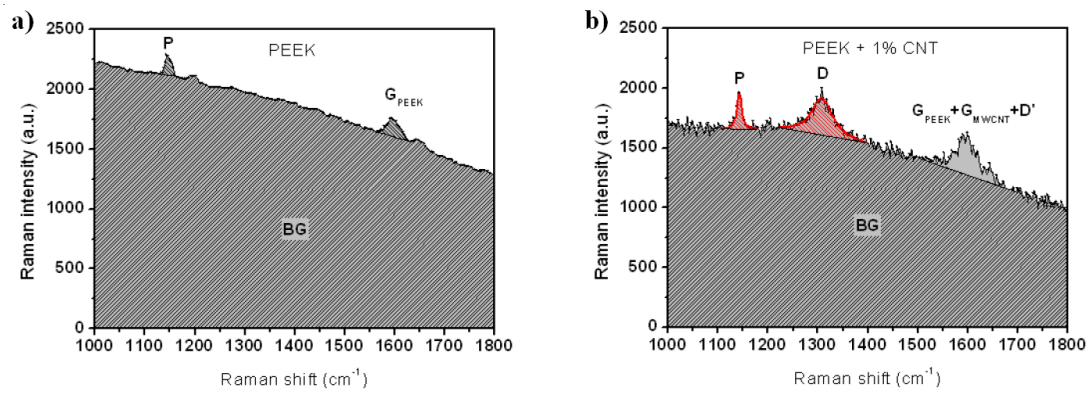

Figure 3.18. Reprehensive Raman spectra for a) PEEK only and b) PEEK with MWNT.

Three Raman bands are observed: the D and G coming from the CNTs [154] and a narrow band at 1144cm^{-1} coming from the polymer. It corresponds to the asymmetric C-O-C stretch vibration in the PEEK polymer [115] and is referred from here on as the P band. In pure PEEK one can also observe a less intense G band (we keep this name for simplicity) due to the presence of sp^2 bonded carbon in the benzene ring of the polymer. The background in the PEEK spectra is caused by luminescence of PEEK and by the Raman signal of the amorphous PEEK polymer. The line under the peak (Figure 3.18a-b) shows the limit of the background signal.

Statistical analysis

Since PEEK does not have any D band, we use the D band as an indicator of the presence of CNTs. For statystical analysis we fitted the D band and the P band with Lorentzian line shapes (red lines in Figure 3.18b) and calculated their integrated intensities as well as the background (BG) signal. The integrated intensities are represented as maps in Figure 3.19, were dark parts correspond to lower intensities, while brighter parts correspond to higher intensities.

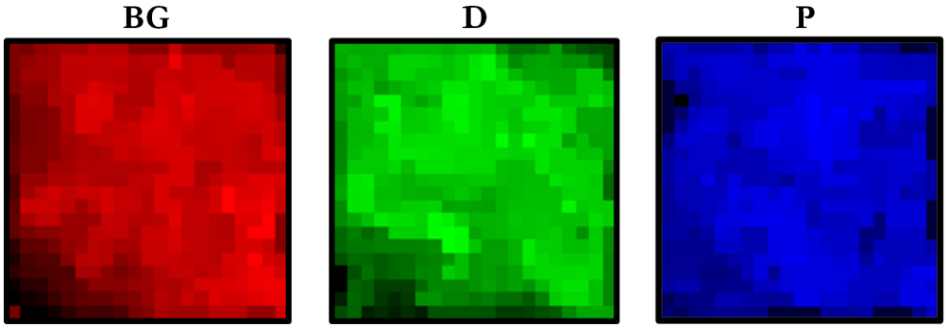

Figure 3.19. Raman map of the background (BG), the D band and the P band.

For each Raman map we have generated a histogram of the ratio of the D and PEEK band integrated intensities with respect to the background signal: A_D/A_{BG}, A_{PEEK}/A_{BG}. Figure 3.20 shows an example of such a histogram.

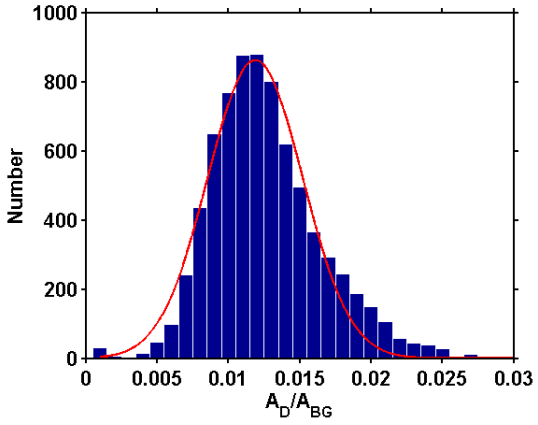

Figure 3.20. An example of a deduced histogram of relative intensity of the D band. The position of the maximum of the histogram measures the amount of CNTs and the standard deviation gives a measure of the dispersion of CNTs in the composite.

We recorded several Raman maps for each location and generated an averaged histogram of the relative band intensities. Even if each Raman spectrum is noisy, the statistical analysis reduces the uncertainty by a factor of 84 leading to perfectly interpretable data.

We fit the histograms with a Gaussian line shape (red line in Figure 3.20) to obtain the position of the maximum and the broadening (corresponding to a quantity proportional to the standard deviation). While the position of the maximum in the A_D/A_{BG} histogram gives a measure of the CNT content, the standard deviation gives a

measure of the dispersion of the tubes. Our statistical analysis assumes that the oscillation strength variation due to the tube surrounding and organization is sufficiently small and can be ignored. We note that standard deviation in Figure 3.20 should not be confused with the noise of one Raman spectrum. The standard deviation in the histogram of the Raman map is also referred to as image noise. We note that the statistical error, which limits the statistical analysis, is less than the extracted image noise.

From literature it is known that the P band does not change in amorphous and crystalline PEEK [155] (Figure 3.21a) but increases in intensity (×1.5) when approaching the melting temperature (300°C) (Figure 3.21b).

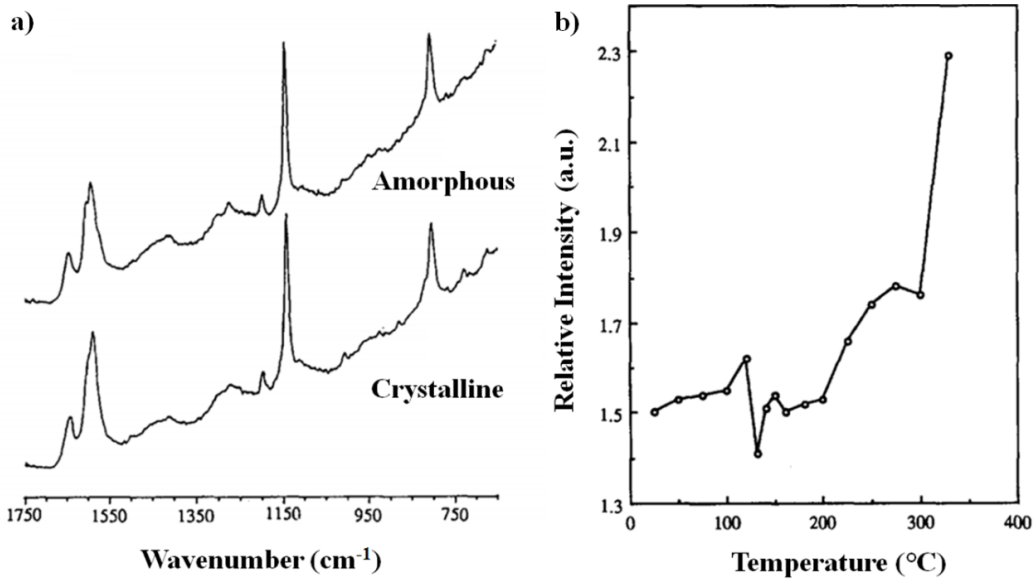

Figure 3.21. a) FT-Raman spectra of amorphous and semi-crystalline PEEK b) Relative intensity of the C-O-C stretching Raman mode of PEEK as a function of temperature [155].

The P band is therefore expected to be uniform across the Raman map. However, some variation in the ratio of the P band over the background signal were found which we attribute to be induced by the presence of CNTs. The presence of CNTs can modify the optical field and structure in their neighborhood and as a result change the intensity of the P band. The position of the maxima of histograms and standard deviations of the relative D band intensities as a function of CNT content are shown in Table 3.6.

Sample	$\langle A_D \rangle / \langle A_{BG} \rangle$ mean	$\langle A_D \rangle / \langle A_{BG} \rangle$ broadening/mean	$\langle A_P \rangle / \langle A_{BG} \rangle$ mean	$\langle A_P \rangle / \langle A_{BG} \rangle$ broadening/mean
Pure PEEK	0.0001	-	0.00093	0.26
PEEK 0.5%CNT	0.0064	0.31	0.00090	0.40
PEEK 1%CNT	0.0173	0.25	0.00212	0.30
PEEK 2%CNT	0.0494	0.16	0.00301	0.31

Table 3.6. Position of the maximum of the histogram of the relative Raman D and P band intensity and standard deviation as a function of CNT content.

We observe that the D band intensity increases with increasing amount of CNTs in the composite as expected but at the same time the D band histogram gets broader while the broadening/mean ratio remains constant showing clearly that the distribution of the tubes is homothetic with CNTs concentration. With an average diameter of 10nm and 10 walls, each MWNT absorbs roughly $1-(0.977)^{20}=0.4$ [156] of the incident light when assuming the refraction index of graphene (reduction of 2.3% after each layer). As a consequence, with a layer of 2µm with 1wt% of CNTs, the transmitted light represents 60% of the incident light. The Raman probe depth due to light path in the material (direct and return) is less than 2µm. As we do not use a confocal arrangement, the probe depth with our experiment is thus limited by the absorption of the nanotubes and is proportional to the concentration. As a consequence, we assume that the $<A_D>$ value is constant while the $<A_{BG}>$ is proportional to the measured volume (spot size multiplied by the Raman probe depth). Then, the $<A_D>/<A_{BG}>$ ratio is proportional to the CNT concentration. The broadening/mean value is a measurement of the distribution normalized by the volume (the mean value is proportional to the volume at a given concentration). Consequently, this value is nearly constant for all concentration as the mixing process is the same at all concentrations (same screw speed and same injection parameters). These behaviors are expected and confirmed by Raman mapping analysis. Interestingly the PEEK band increases with increasing amount of CNTs in the composite. CNTs are known to act as nano-antennas [157] and CNT absorption of the optical field is higher than the polymer matrix. This increases the local field around the CNTs and as a result the Raman signal of the surrounding matrix is intensified [158]. Furthermore the smooth surface of CNTs can lead to local ordering of the polymer molecules which can also increase the Raman signal of PEEK.

From the DSC measurements, we know that the average crystallinity does not change with the presence of CNTs but it is still possible that CNTs change the nature of the crystallization. This is reflected in the reduction of ductility with 15wt% of carbon nanofibers (CNF) and with 1wt% of CNTs discussed above. This suggests that the presence of CNTs changes the structural flexibility of the matrix due to a structuring of PEEK in contact with or near the CNTs. Brosse *et al.* [159] report epitaxial growth of polymer crystallites around CNTs but no large modification of the average crystallinity.

We carried out the same Raman analysis on maps at the core and the edge of the composite beam. Surface areas of 200µm × 200µm, in steps of 10µm for the PEEK+1wt% of CNTs sample were Raman mapped and histograms for the D band and the P band were deduced. The average values are shown in Table 3.7.

Sample	$<A_D>/<A_{BG}>$ mean	$<A_D>/<A_{BG}>$ broadening/mean	$<A_P>/<A_{BG}>$ mean	$<A_P>/<A_{BG}>$ broadening/mean
Core	0.0173	0.25	0.0021	0.30
Edge	0.0142	0.26	0.0016	0.37

Table 3 7. Result of statistical evaluation of relative Raman D and P band intensity for 1% CNTs in the core and the edge of the sample.

The statistical analysis of the intensity of the D band shows that the concentration of CNTs is higher in the core. That is consistent with the difference in hardness observed with the nano-indentation measurements. The micro-hardness was found to

be higher at the core than at the edge of the composite beam, which correlates with the amount of CNTs present in the two different locations ($<A_D>/<A_{BG}>$) (Table 7).

Two hypotheses can be made here: the tensile strain variations are either caused by a change in CNT concentration or a change in the agglomeration of CNTs. In both cases, it could lead to a decrease of the modulus and to a change in the ratio $<A_P>/<A_{BG}>$. Since the ratio of standard deviation and mean value of the histogram does not change much between the edge and the core, we suspect that this variation is linked to the concentration variation rather than to tube bundling. The higher CNT concentration at the core of the beam results in higher hardness at the core of the beam. Possibly the injection molding process and the temperature history of different parts of the beam influence local CNT dispersion resulting in variations in hardness.

3.2.6 Small-angle neutron scattering

SANS measurements were performed in collaboration with Stephen King and Richard Heenan at the ISIS Facility, Oxfordshire, UK.

Small-angle X-ray and neutron scattering (SAXS/SANS) are complementary techniques able to observe the distribution of CNTs in polymer composites. SAXS and SANS provide information about CNT bundling and the morphology of the polymer [133] [160].

We have conducted SANS measurements to probe the structural organization in the composite at intermediate length scales (~1nm – 400nm). Some representative SANS data are shown in Figure 3.22. The data between $0.2 \leq q \leq 1.2$ Å^{-1} is essentially a flat background, consistent with the persistence length of PEEK. The prominent crystal peaks are at $q > 1.2$ Å^{-1} [161].

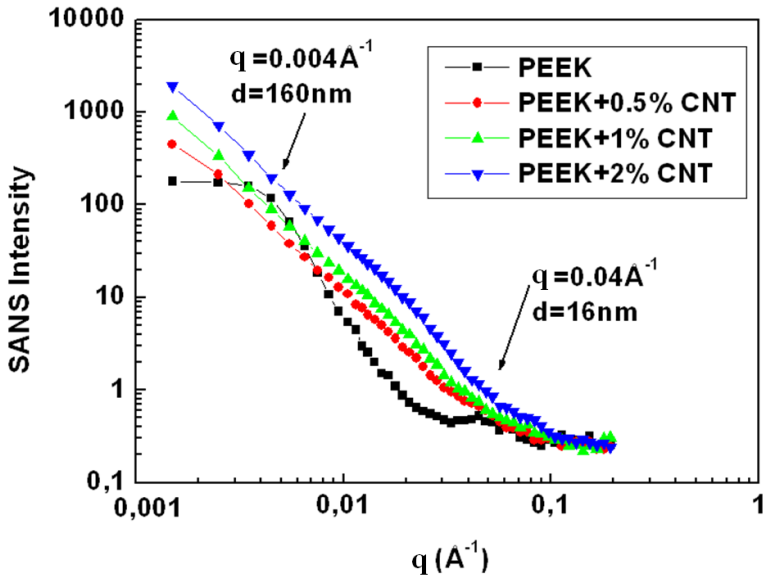

Figure 3.22. SANS intensity versus q for pure PEEK and nanocomposites with 0.5, 1 and 2wt% of CNTs.

In the pure PEEK sample the SANS primarily arises from the difference between the amorphous and crystalline regions. The broad peak centered at q=0.04 Å^{-1}, which corresponds to a length scale (d) of 16nm on applying the Bragg relation, $d=2\pi/q$, is

characteristic of the two-phase nature of the spherulite sub-structure in PEEK [161] [162]. The limiting behavior of these data at lower q values can probably be attributed to the size of the spherulites themselves; the data fits quite nicely to a model for polydisperse spheres of average radius 28 nm with 40% polydispersity, but *does not* fit to a model for Gaussian chains (fits not shown for clarity).

When CNTs are introduced into the PEEK matrix the SANS primarily arises from the CNTs rather than the polymer, and so the features discussed above are suppressed. Instead, power-law scattering manifests itself. The neutron scattering length density of the CNTs is ~4 – 5 and that of the hydrogenous PEEK is ~2 (in units of either 10^{-6} A^{-2} or $10^{10}cm^{-2}$. In the q range 0.002 – 0.02 $Å^{-1}$ the exponent characterizing this power law is ~2.2, consistent with a fractal, network-like, distribution of the CNTs [133]. The shoulder centered at q~0.02 $Å^{-1}$ is likely from the underlying form factor from the nanotubes. In the q range 0.05 – 0.1 $Å^{-1}$ the power law exponent is ~1, and this likely reflects the crossover from the aggregate structure to that of individual nanotubes. Applying the Bragg relation this time gives $d=2\pi/0.05=126$ Å or ~13nm. This is rather too short to be an estimate of the length of the nanotubes, but is typical of the overall diameter of MWNTs. The lower q limit of the q^{-1} region is therefore masked by the aggregate structure. Indeed, it can be seen that the SANS intensity approximately scales with the CNT loading of the matrix. Whilst these data cannot say anything definitive about the effect of the CNTs on the structure of the PEEK chains. The similar form of the SANS data for the CNT-loaded PEEK samples is evidence that the aggregate structure of the CNTs is similar at all three CNT concentrations studied.

3.2.7 Conclusions

Nano indentation measurements reveal hardness variations at the core and the edge of the beam while statistical evaluation of two Raman bands associated with PEEK and MWNTs indicates that the MWNT concentration is higher in the core as compared to the edge of the beam. We use histograms of the relative intensity of the D band across a Raman map to measure the amount of MWNTs and their dispersion. We find that variations in MWNT concentration lead to variations in hardness in MWNT/PEEK composites. While the average crystallinity of the polymer is not affected by low concentrations of MWNTs, they appear to influence organization of the polymer around the tube affecting the overall ductility of the composite beam. SANS measurements confirm this interpretation. Two peaks in the SANS spectrum disappear when CNTs are present even as low as 0.5wt% of CNT incorporated in PEEK revealing matrix structural changes at the nanometric scale.

3.3 Self diffusion of deposited CNTs

It has been recently discovered that annealing of carbon nanotubes on the surface of a thermoplastic polymer forms a composite surface layer with uniform tube dispersion at scales of ~10 micrometers [163]. This phenomenon is in relation with the dynamical percolation phenomenon in bulk nanocomposites that has been observed by several authors [67] [69] [68]. In this part we propose a strategy to define and characterize the modifications of the percolative network at micrometer and submicrometer scales. To get a better understanding of the self-dispersion process of CNT, we use transmission electron microscopy and Raman multi-spectral imaging. While transmission electron microscopy turns out to be limited when observing small diameter nanotubes in a polymer matrix, Raman spectroscopy can be used to monitor the tube dispersion at different scales (>1 micrometer).

3.3.1 Sample preparation

The dispersion experiments were carried out at identical conditions. Solutions of known amount (4, 8, 12, 20, 30, 40 and 50 drops where 1drop: 0.4 10^{-6}g of CNTs) of DW and MW CNTs were dropped on a PEEK sheet supplied bv Victrex Technology Center, UK (Figure 3.23a and 3.24a). We have used MWNTs from Arkema (Graphistrength 100) and FutureCarbon (FutureCarbon GmbH, Bayreuth); and DWNTs from CIRIMAT (E. Flahaut and Ch. Laurent), as received.

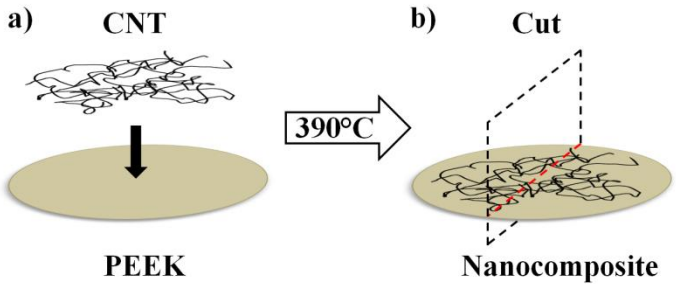

Figure 3.23. Schematic presentation of sample preparation
a) agglomerated CNTs are deposited on PEEK sheet and annealed in argon atmosphere
b) resulting nanocomposite.

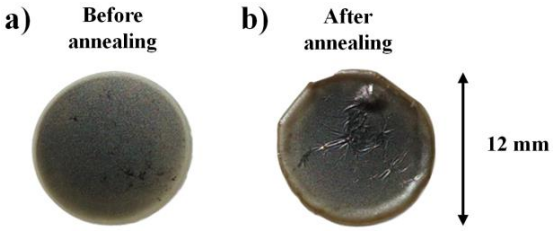

Figure 3.24. Photos of the sample a) before and b) after annealing.

We have used N-Méthyl-2-Pyrrolidone (NMP) as a solvent since it is a good nanotube dispersant and it has an excellent wettability of PEEK surface (Figure 3.25).

Figure 3.25. Droplets water and NMP on the surface of PEEK.

The samples were annealed in Argon atmosphere. Argon was pumped through the oven (size: 1m × 2.5cm) prior to annealing process for 90 minutes (Argon flux = 0,16 L/min) to avoid oxidation of the samples. The samples were annealed above the melting temperature of the thermoplastic polymer (at 390°C) for 15 minutes (Figure 3.23b and 3.24b).

3.3.2 Electrical measurements

Electrical measurements, i.e. I(V), with a maximum tension of 5V and a step of 0.1V (1 second per point) were performed using an electrometer from Keithley (model 6517B/E). For these measurements, two silver electrodes were deposited at a distance of 11 mm (Figure 3.26).

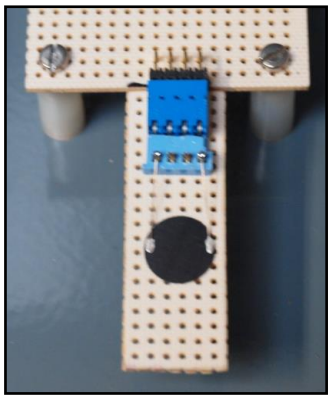

Figure 3.26. Two probe Keithley setup for electrical measurements.

Electrical measurements were performed as a function of the number of droplets of MW and DW CNTs in NMP evaporated on a given surface (3.5mg/m^2 droplet). We performed the measurements before and after annealing.

The resistance decreased with the amount of nanotubes deposited. In the case of MWNTs before the annealing we can see that the resistance decreases rapidly at low concentrations and reaches a plateau at 75mg/m^2 (black line in Figure 3.27a). In the case of DWNT when increasing the number of droplets of the NMP carbon nanotube solution on the PEEK surface the resistivity did not necessarily increase before annealing (black line in Figure 3.27b). We assume that the drying process is agglomerating the tubes on the surface in a non-uniform way.

The annealing has the effect that the resistance decreased by one or two orders of magnitude (red line in Figure 3.27a and b).

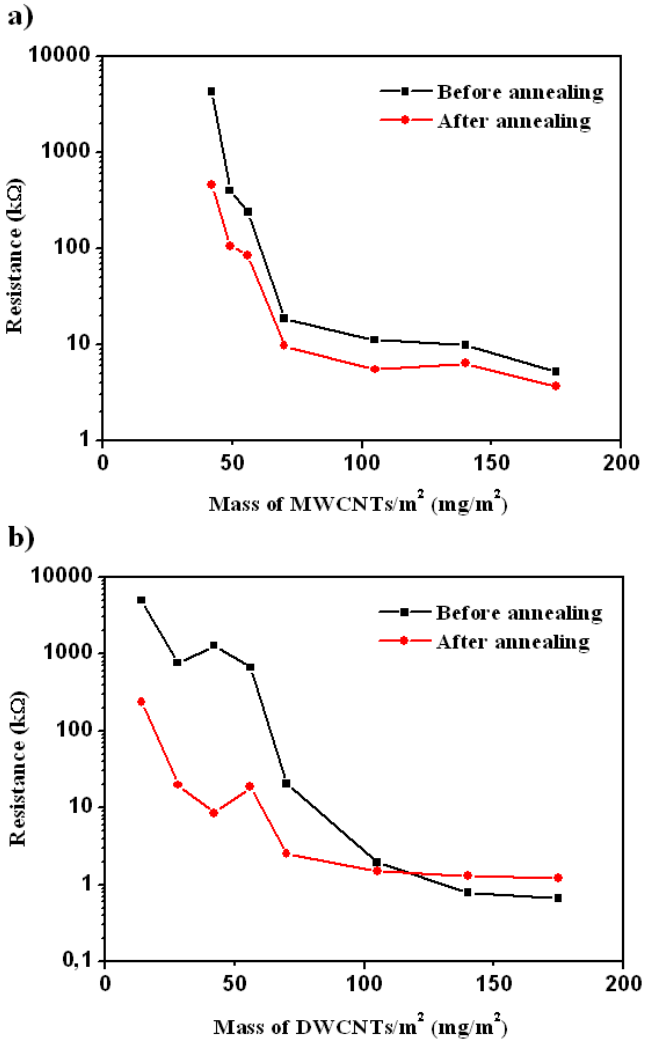

Figure 3.27. The effect of annealing on Resistance for a) MWNTs b) DWNTs.

This decrease arises from two effects. The first one is the evaporation of the insulating solvent at the temperature around 200°C, which increases the conductivity by approximately five times. The second one is the increase in number of conducting paths. This means annealing has the effect to spread larger agglomerates and to increase the amount of smaller agglomerates multiplying the number of connecting paths.

For DWNTs at high loadings we observe that annealing does not lead to the decrease in resistance of the samples. On the contrary, it increases the resistance with respect to the unannealed samples. We do not observe this effect with MWNTs at the same mass loadings. We assume that when the concentration of CNTs on the surface of PEEK is large enough all tubes are connected into a network and annealing leads only to the incorporation of the insolating polymer between the CNTs. We do not observe this effect with MWNTs probably because the amount of MWNTs at the same mass loading is less [48], thus they do not yet have a complete network.

3.3.3 *Insitu* annealing

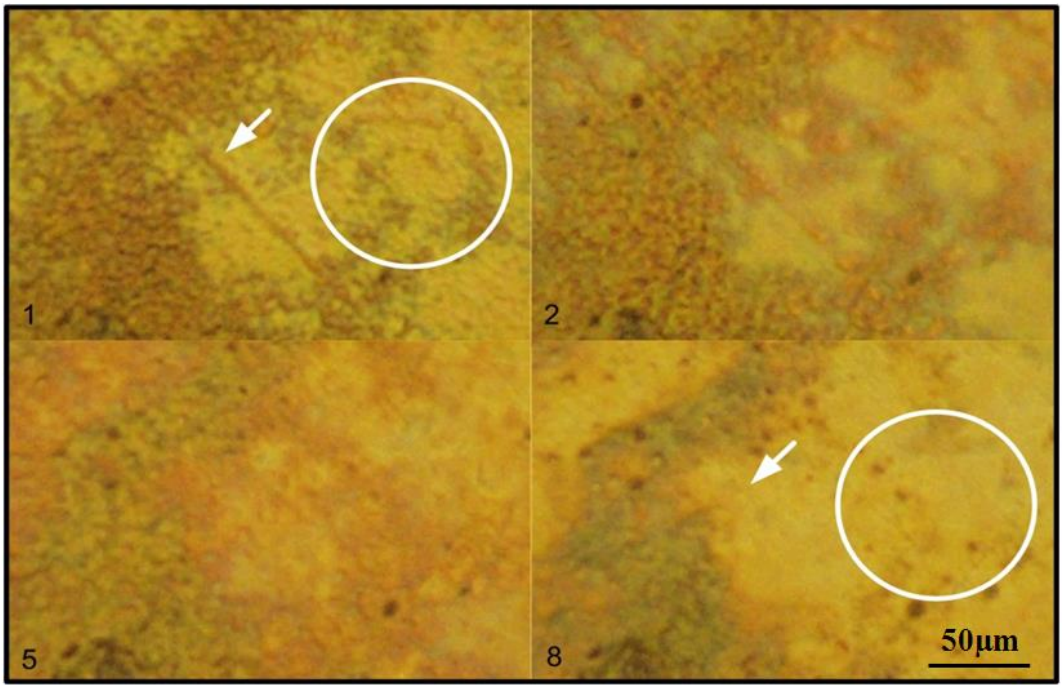

Figure 3.28. Annealing agglomerated tubes on the surface of PEEK. Before (frame 1), during (frame 2, 5) and after annealing (frame 8).

To see the effect of the dispersion of the tubes at larger scales we have annealed *insitu* (390°C) samples with CNT deposited on the surface of PEEK in vacuum under an optical microscope. Figure 3.28. shows a region before (frame 1), during (frame 2, 5) and after annealing (frame 8). The circle shows a region before and after annealing. The contrast from agglomerated tubes at the surface is reduced after annealing. This is attributed to the diffusion of the tubes into the PEEK substrate. The arrow shows a line from a scratch on the surface before melting on the surface which disappears once the PEEK melts.

3.3.4 Transmission electron microscopy

Figure 3.29 shows SEM images of MWNTs on the surface of PEEK. Before annealing one can see agglomerated tubes. After annealing it is observed that PEEK is wetting the CNTs and they become incorporated into the polymer.

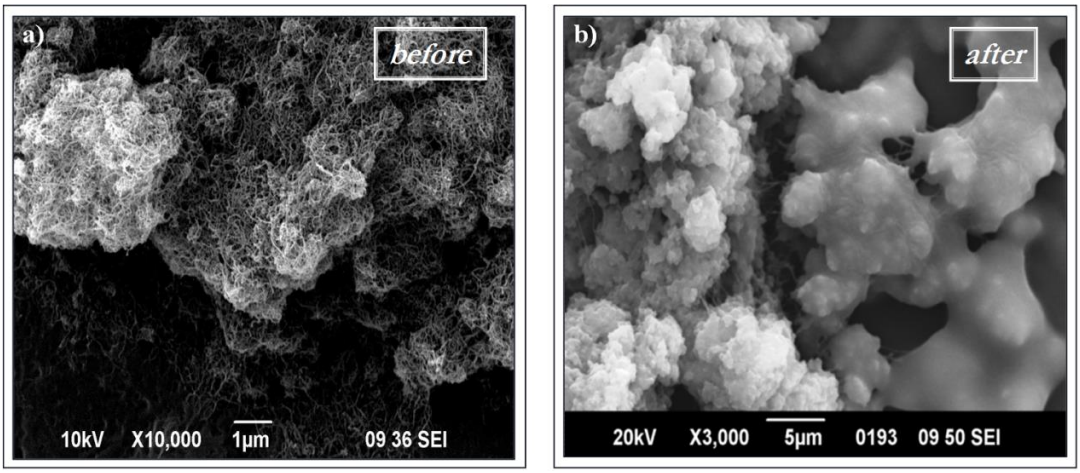

Figure 3.29. SEM images of PEEK film with MW CNTs a) before annealing MWNTs on the surface of PEEK b) after annealing PEEK is wetting MWNTs. The images were obtained by Dr. Victoria Tishkova.

PEEK contains oxygen groups which can interact with the nanotube surface. It is known that molecular oxygen binds to single walled CNTs with adsorption energy of 0.25eV [164]. Furthermore it is known that the interaction of oxygen with the nanotube surface leads to hole doping and quenching of the luminescence in SWNTs. The phenol rings in PEEK are compatible with the honeycomb lattice of the tube surface. Both these effects contribute that PEEK is wetting CNTs.

To assess the structure and morphology of composite materials formed at the surface of PEEK after annealing we use TEM and Raman spectroscopy. For TEM measurements all samples were placed in an epoxy matrix and cross sections were cut with ultra microtom equipped with a diamond knife in 100nm thick slices. The slices were placed on Cu grids with a holey carbon film. TEM experiments were carried out on a transmission electron microscope Philips CM20 with accelerating voltage 120kV. TEM micrographs provide a detailed view over several micrometers regions. Figure 3.30 shows a TEM cross section at the interface between the diffusion layer and the PEEK matrix.

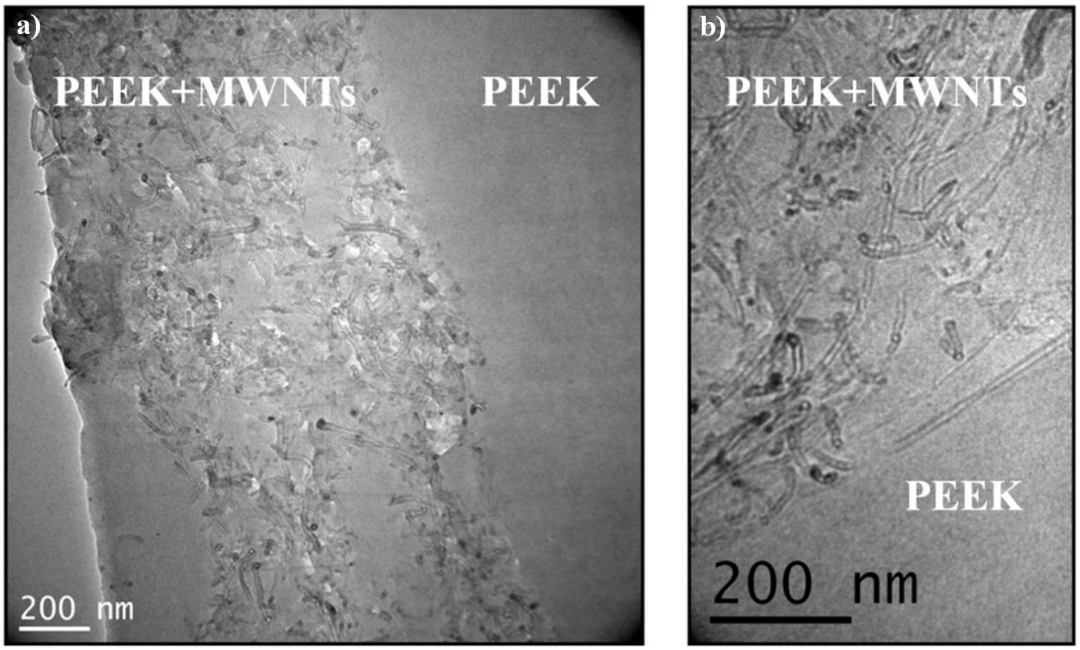

Figure 3.30. TEM images of MWNT/PEEK composite at different resolutions. 15 minute annealing at 390°C of agglomerated CNTs on surface of PEEK. MWNTs tend to be oriented parallel to the interface.

The MWNTs are found to be uniformly distributed and no large agglomerations are observed. A clear interface is formed between the composite and bulk PEEK. We also observe that CNTs align along the interface of the composite layer and the bulk PEEK (Figure 3.30b).

Interestingly no concentration changes are observed in the vicinity of the diffusion layer or at scales larger than the mean distance between the tubes. In general the diffusion of nanoparticles in a polymer matrix depends on size and shape of the nanoparticle. While the diameter of carbon nanotubes is comparable or smaller than the chain length of the polymer, the tube length is several orders of magnitude longer. For individual nanotubes with different mobility depending on diameter and length, one would expect a gradual reduction of the concentration with increasing distance from the surface. However, the fact that the tubes were agglomerated when the solvent evaporated on the surface of the PEEK film indicates that tubes remain connected in a loose network after annealing acting as a single phase. The mobility of the CNTs in the polymer matrix is expected to be much smaller due to its large mass compared to the polymer molecule. Given the large length of CNTs they inevitably are bent depending on the local structure of the polymer and the presence of small crystallites in the vicinity of the CNT. Structural variations along the tube imply and its larger mass has the effect that vacancies are formed between the polymer matrix and the CNTs. The surface of CNTs is atomically smooth increasing diffusion of polymer molecules on its surface as long as the interaction with the CNT surface is small enough. The surface adsorption energy is about one order of magnitude larger than the thermal energy at room temperature. Since the PEEK molecules are chains they have the tendency to align with the CNT axis favoring diffusion along the tube axis. It has been shown through numerical simulations that the diffusion of polymer molecules along the tube axis is larger than in directions perpendicular to it [165]. This means that the tube

surface represents a preferential diffusion path for the matrix molecules. With the TEM we observe PEEK covering the tubes on the surface of the composite layer (Figure 3.31).

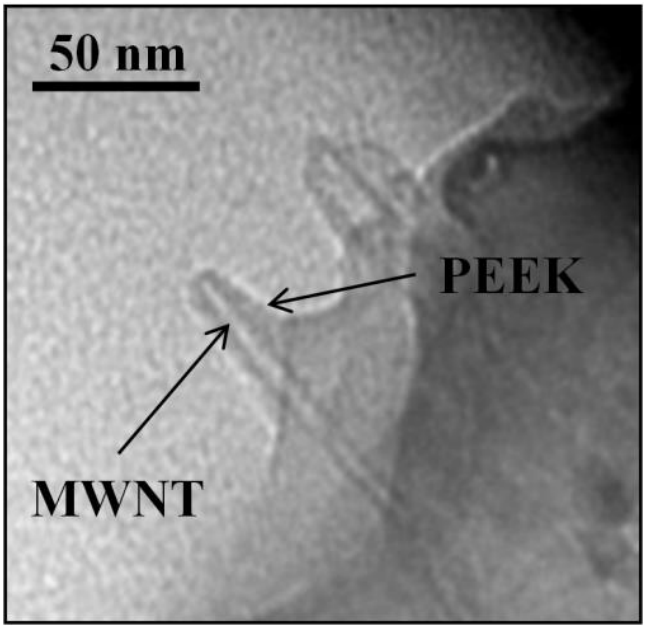

Figure 3.31. TEM image of the surface of the composite layer. PEEK covers the tubes.

The diameter and length distribution of CNTs and the presence of other forms of carbon have the effect that the CNT agglomeration is disordered with frequent vacancies and gaps between the tubes. PEEK molecules have the tendency to diffuse into these vacancies limiting the bending of the tubes. When neighboring tubes leave a vacancy behind, induced by bending motions, the vacancy gets filled in with PEEK having the effect of separating the tubes. The high temperature stability of PEEK makes it possible to keep the temperature of the polymer at elevated temperature favoring the effect of diffusion into the CNT agglomerate.

Multi-walled CNTs are conductors or small gap semiconductors (E_{11}^{S} (eV) = 0.8/d (nm), leading to a band gap of 0.08eV (d=10nm, Infra-Red) for the outer tube) and are excellent absorbers of electromagnetic radiation. The singularities in the electronic density of the quasi one dimensional nanotubes and the large range of diameters of the concentric walls make MWNTs excellent broad band infrared and optical absorbers. The absorbed heat is, however not well dissipated. Heat conduction in carbon nanotubes is mediated through phonons and is inefficient between CNTs. The small diameter of CNTs implies that effects of quantization of phonons perpendicular to the axis are strongly reducing heat conduction. In contrast the insulating polymer matrix has a much smaller optical absorption, several orders of magnitude smaller. The high absorption of electromagnetic radiation at the nanotube leads therefore to a heat backlog or imbalance and a heat gradient is formed around tube agglomerations. In addition the annealing process also implies exposure to higher infrared radiation and as a result higher radioactive heating. The higher temperature in the proximity of the tubes is correlated with a higher diffusion of the polymer molecules near and on the tubes. This means the action of diffusion is large where there tube agglomerates are. This contributes in making the dispersion more uniform.

To understand the influence of the time of annealing and the type of CNTs on the structure of the diffusion layer we conducted the annealing experiments with two kinds of commercially available multi-walled carbon nanotubes: FutureCarbon CNT-MW (FutureCarbon GmbH, Bayreuth, Germany) and Graphistrength® C100 (Arkema, Colombes, France). Properties of the raw CNTs are summarized in Table 3.8.

MWNT supplier/grade	Arkema Graphistrength	Future Carbon GmbH
Carbon purity (%)	90	98
Diameter (nm)	9-30	8-17
Length (μm)	0.1-10	1-10
Number of layers	5-15	5-9
Density (kg/m^3)	50-150	28

Table 3.8. Properties of nanotubes supplied by Arkema and Future Carbon [166].

According to this table we can see that carbon purity of Future Carbone nanotubes (98%) is greater than for Arkema tubes (90%). The variation of diameter, length and number of layers is smaller for Future Carbon nanotubes. Furthermore Arkema tubes have a higher bulk density as compared to Future carbon tubes. We can also see that the aspect ratio is greater for Arkema tubes. It means that they tend to agglomerate more than Future Carbone tubes. TEM image of the two types of nanotubes are presented in Figure 3.32.

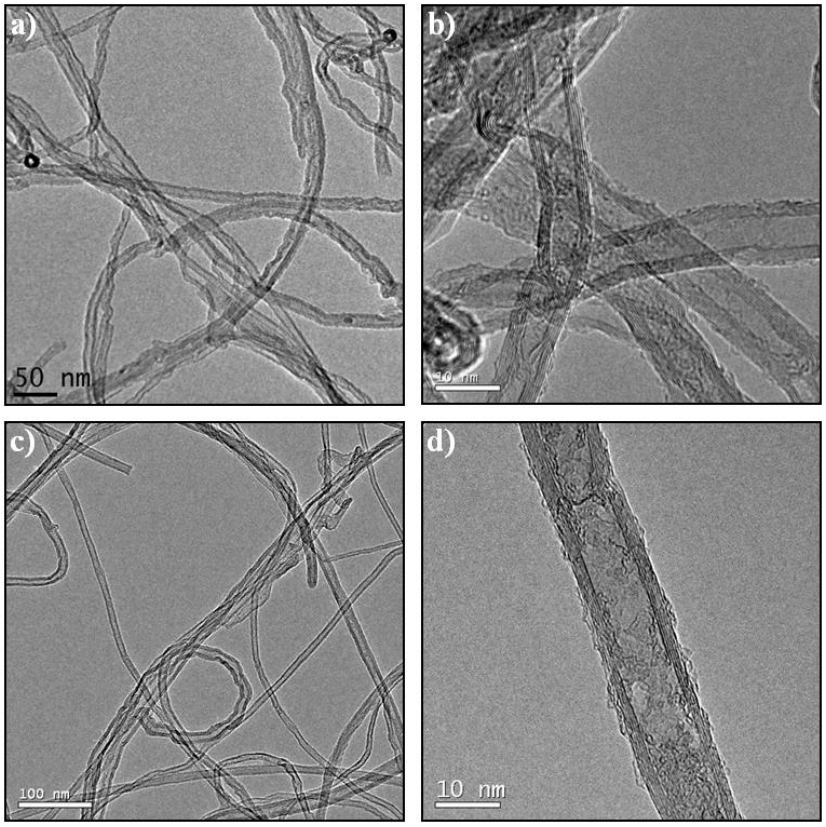

Figure 3.32. TEM images of raw MWNTs at different magnifications a) and b) Arkema c) and d) Future Carbon

TEM images of raw nanotubes show that the tubes produced by Arkema contain more defective and more catalytic particles compared with Future Carbon CNTs. To estimate the quality of CNTs we carried out a Raman experiment. Raman spectra taken from Arkema and Future carbon MWNTs (excitation wavelength 488nm) are presented in Figure 3.33.

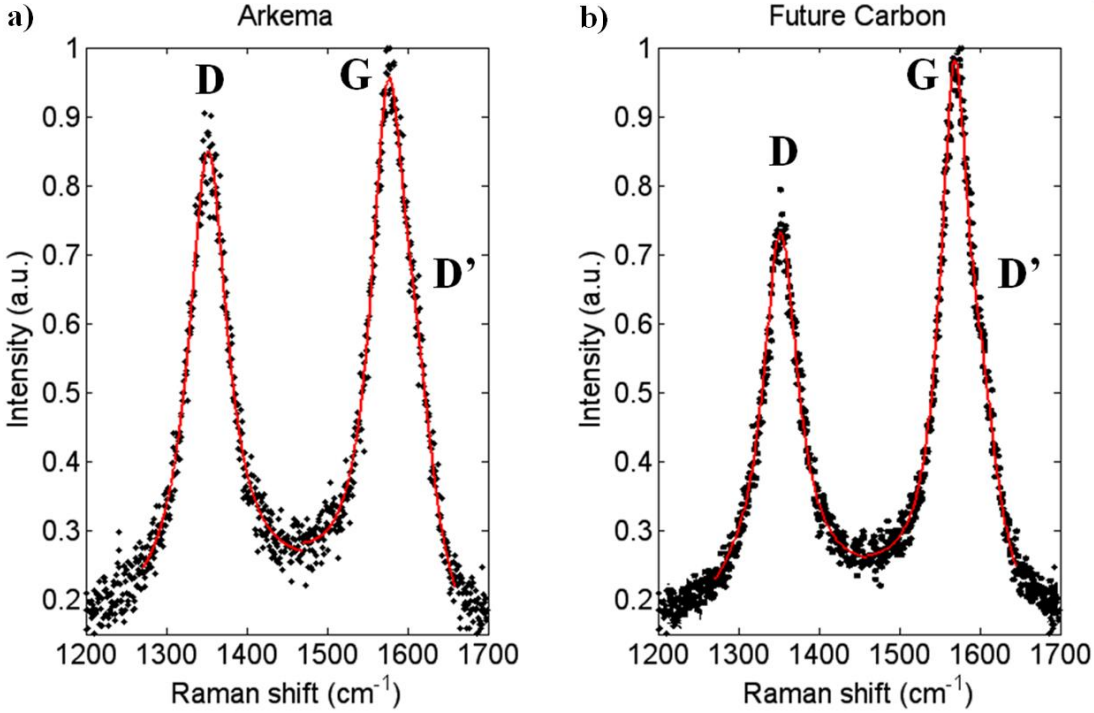

Figure 3.33. Raman spectra of multi wall carbon nanotubes a) Arkema and b) Future carbon, measured on an XY Dilor spectrometer (excitation wavelength 488 nm).

The spectra in both pictures present the disorder induced D band and the tangential mode G with the defect induced shoulder at the higher energy side (D' band).

A ratio of the intensities of the D band over the G band ($\rho = I_D/I_G$) is a good indicator of quality of bulk samples. The relative intensity of D and G bands was calculated for both types of tubes:

$$\rho_{\text{Arkema}} = 0.92$$

$$\rho_{\text{Future Carbon}} = 0.66$$

Future Carbon spectrum is the one that shows a lower ration, consequently the tubes have a lower quantity of structural defects. This is coherent with the differences seen in the TEM images in Figure 3.32.

TEM images of the cross sections of the diffusion layers for samples with both types of tubes annealed for 15 and 30 minutes are presented in Figure 3.34.

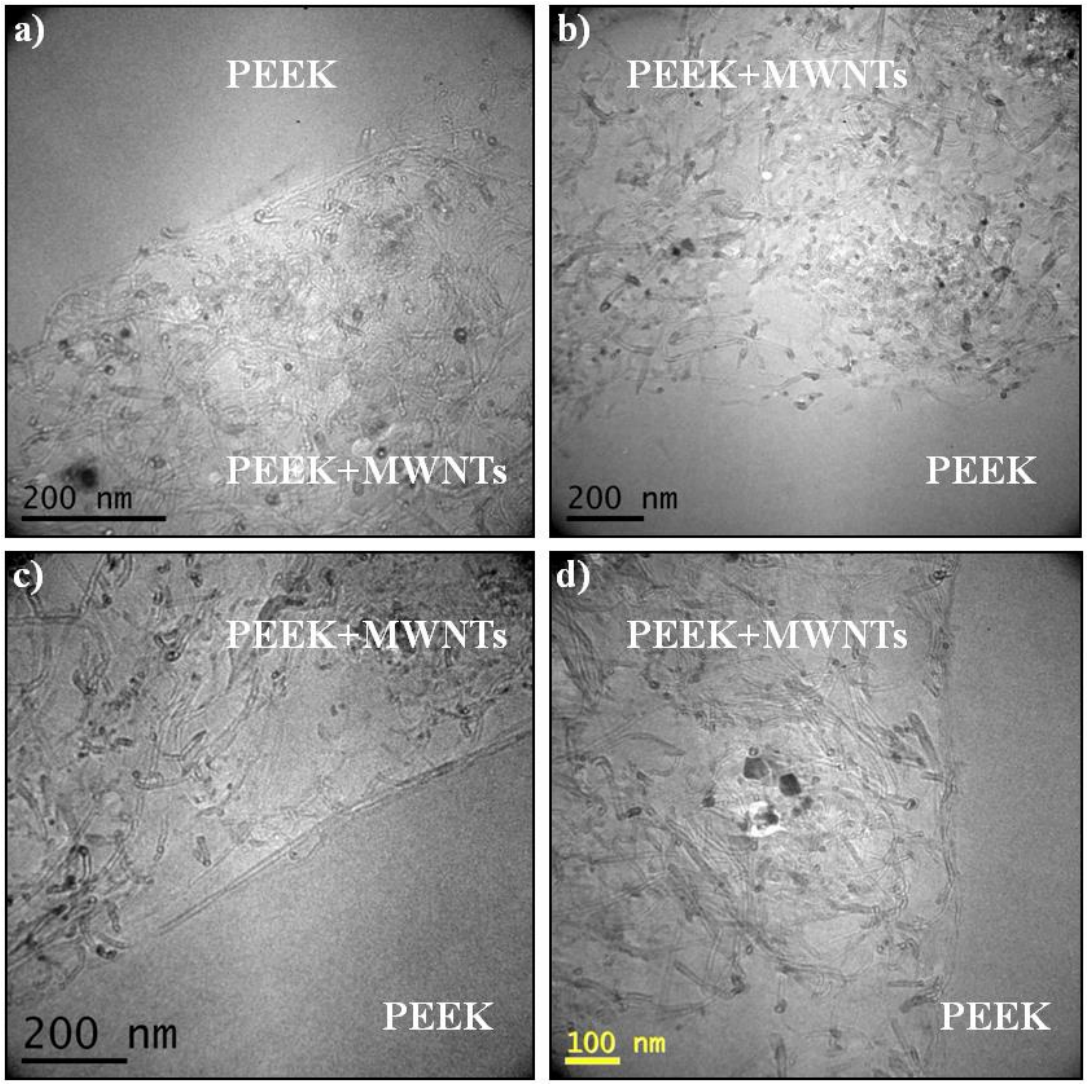

Figure 3.34. TEM images of the cross sections of the diffusion layers of CNT/PEEK composites with different MWNTs. a) and b) Arkema MWNTs annealed for 15 and 30 minutes, respectively c) and d) Future Carbon MWNTs, annealed for 15 and 30 minutes, respectively.

In the TEM images one can see pure PEEK and the diffusion layer. A uniform distribution with a well-defined strait interface between the polymer matrix and the composite layer is seen for all samples. Despite the properties of raw nanotubes are different we see an equal uniform dispersion of Arkema and Future Carbon MWNTs in the polymer matrix. The diffusion layer is also uniform when increasing the annealing time to 30 minutes. So we conclude that the structural quality of carbon nanotubes does not affect the process of the uniform dispersion.

Using TEM allows estimating the length of the MWNT diffusion layer. Figure 3.35 shows the MWNT/PEEK diffusion layer. Amorphous carbon that was initially on the TEM grid to better attach the sample can also be seen in the image. The thickness of composite layer appears to be correlated with the initial density of tubes on the surface of PEEK. For this particular sample that is further used in Raman experiments we estimate the thickness of the diffusion layer to be between 2.5-3μm.

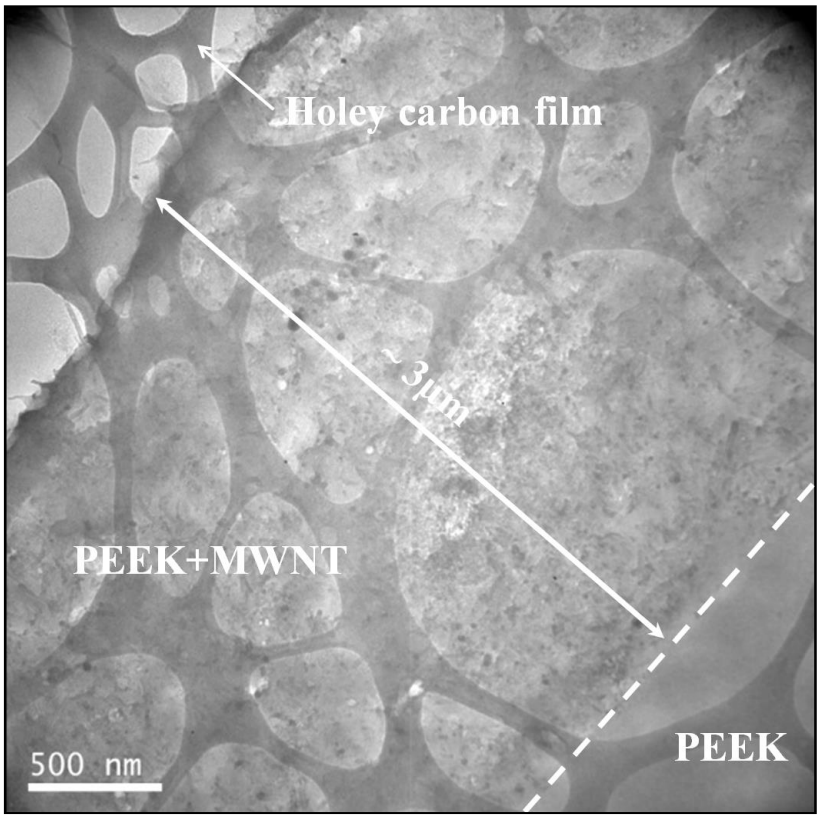

Figure 3.35. TEM image of a MWNT/PEEK cross sectional slice of the composite layer after annealing at 390°C for 15 minutes of agglomerated CNTs on the surface of a sheet of PEEK.

When using DWNTs it is much harder to distinguish the tubes compared to the structural fluctuations of the polymer (Figure 3.36). Double wall carbon nanotubes have a small diameter (2-3nm) and give often not enough contrast against the polymer matrix at low concentration to make them visible.

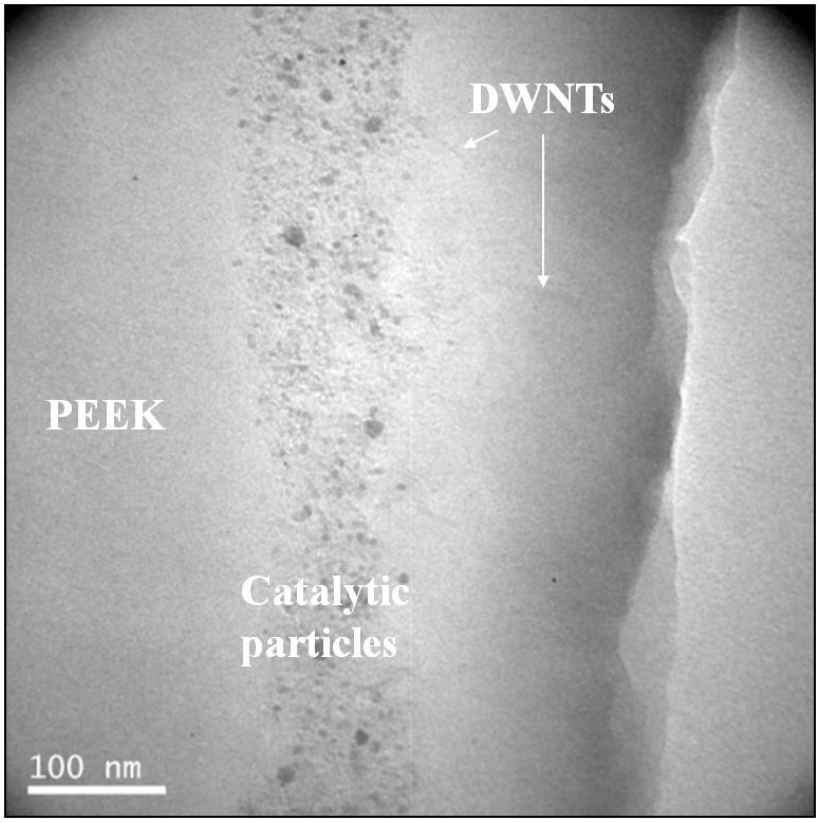

Figure 3.36. TEM image of a DWNT/PEEK composite.
15 minute annealing at 390°C of agglomerated CNTs on surface of PEEK.

We observe some spherical particles that are either disordered forms of carbon or remaining particles from the catalyst when growing the double wall carbon nanotubes. One can see that the catalytic particles are not dispersed in the composite layer. This shows indirectly the importance of PEEK interacting with the tubes and enhanced diffusion on the tube surface. We can also see that some tubes are extending into the right part of the image, but the TEM does not allow making a conclusion about the diffusion layer.

To estimate the thickness and homogeneity of the diffusion layer we use Raman spectroscopy as a complimentary technique to TEM.

3.3.5 Raman spectroscopy

For Raman measurements we used the same samples as used for TEM. Raman spectra were measured on an Xplora Horiba spectrometer using the 785nm excitation wavelength to reduce luminescence.

Raman imaging was performed on the surfaces of the samples that were previously cut for the TEM with a diamond microtom, since the smoothness was better than that provided by polishing with abrasives. Figure 3.37 shows an example of typical Raman spectra obtained for a) MW and b) DW CNT/PEEK composites. Figure 3.37c represents the luminescence signal coming from the PEEK polymer and Figure 3.37d represents the signal from the Epoxy.

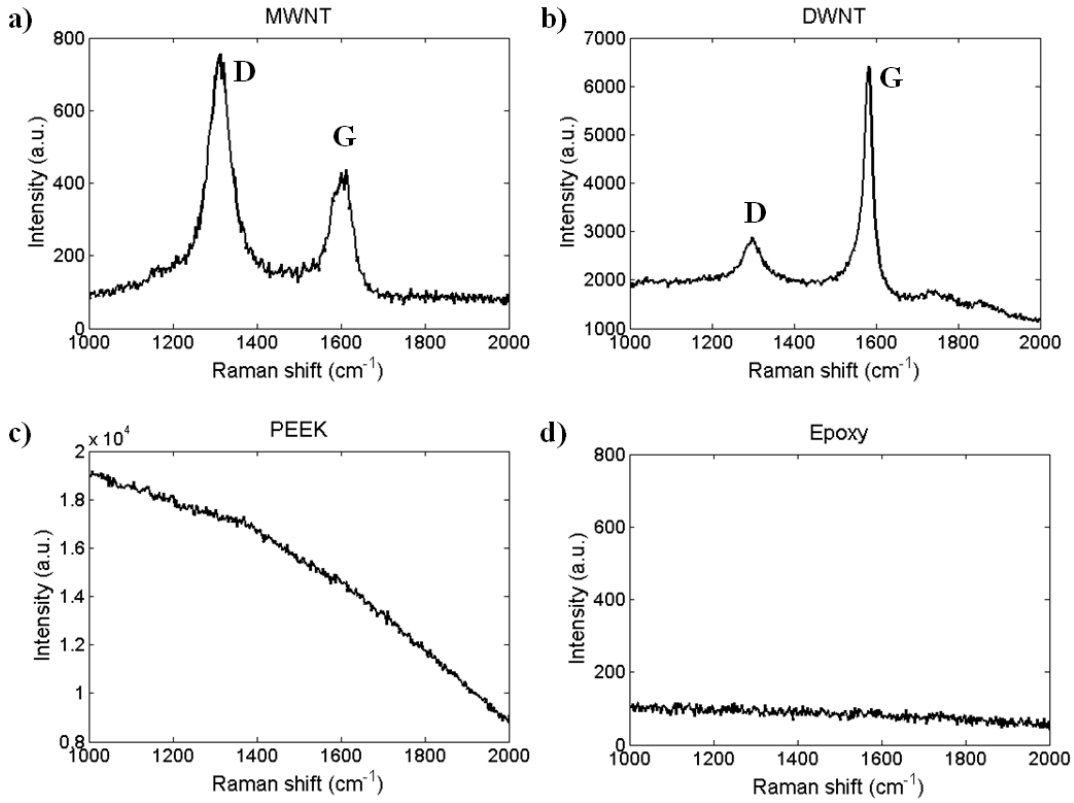

Figure 3.37. Typical Raman spectra for a) MWNT/PEEK composite b) DWNT/PEEK composite c) PEEK d) Epoxy.

In Figure 3.37 one can clearly see differences in relative intensity and spectral line for the spectra of DWNTs and MWNTs. For MWNTs the D band is more intense and both bands are broader. For DWNTs the G-band is more intense and the bands are narrower. This means the DWs contain considerable less defects.

We recorded spectra along a line of 12μm, in steps of 0.02μm across the diffusion layer to analyze its homogeneity. Far from the electronic resonances the intensity of the band is proportional to the amount of CNTs sensed by the focal spot. The amorphous phase and luminescence give rise to a wide background signal. We record Raman maps by varying the step size between 1-10 micrometers to record the uniformity of the tube dispersion at different length scales.

Figure 3.38a shows an optical image of the diffusion layer of MWNTs in PEEK. In Figure 3.38b we see the results of the Raman line scan. The Raman spectra are plotted in horizontal direction and the intensity corresponds to the color in the image.

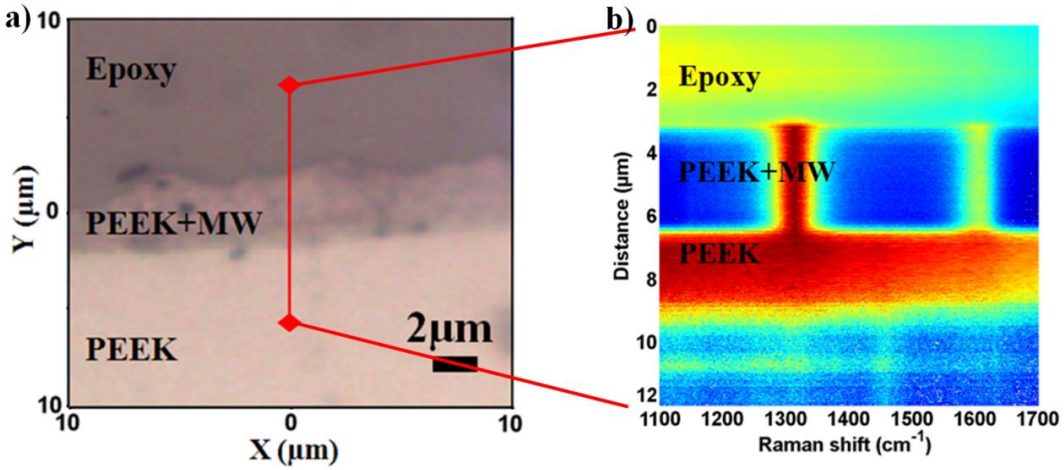

Figure 3.38. a) Optical image of diffusion layer of MWNT/PEEK composite layer b) Raman spectral line across the diffusion layer: the intensity and line width of G and D bands are uniform across the layer and the background signal caused by luminescence is reduced in the composite layer.

The two lines seen in the diffusion layer correspond to the Raman D and G-band. The uniform intensity of the G-band across the composite layer shows that the tubes are homogeneously dispersed in the polymer matrix. This demonstrates that polymer diffusion and anisotropic heat absorption has the effect to disperse the tubes and lead to homogeneous dispersions from high agglomerated tube agglomerates. The thickness of the diffusion layer can be estimated to be 2.5-3µm. This is coherent with what we observe in the transmission electron microscope (Figure 3.35). We notice that the Raman background signal is larger where there are no CNTs. The background signal is due to broadband luminescence in PEEK. The fact that the luminescence signal drops in the composite layer indicates that photo excited charge carriers are efficiently quenched by the presence of the CNT network. This shows that we can use Raman spectroscopy to estimate the thickness and uniformity of the diffusion layer of MWNTs in PEEK.

Figure 3.39 shows a similar Raman line scan when DWNTs were dispersed in PEEK.

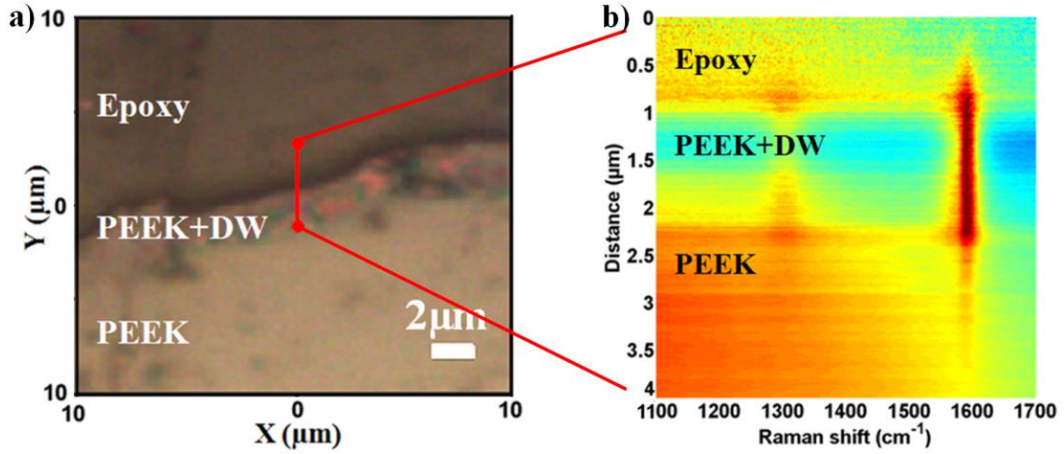

Figure 3.39. a) Optical image of diffusion layer of DWNT/PEEK composite b) Raman line across the diffusion layer: the intensity and line width of G-bands are uniform across the layer. The D band is more intense near the two interfaces.

For DWNTs the G-band is more intense and the D band is less uniform. From the uniform G-band intensity across the layer we conclude that DWNTs are homogeneously dispersed within the spot size of an optical objective and deduce a thickness of the diffusion layer (1-1,5μm). The D band intensity is less intense in the middle of the layer. It is not clear why there are more defects near the two interfaces. It could be that the tubes are more constrained near the surface. Its origin is not clear and needs further investigation. The further extension of the G band in the bulk of PEEK can be attributed to the asymmetric C-O-C stretch vibration in the PEEK polymer [115].

3.3.6 Conclusions

We have shown using SEM that PEEK is wetting CNTs powders. This is qualitatively explained by the presence of oxygen groups interacting with the CNT surface. Using TEM and Raman spectroscopy we show that a uniform composite layer and a clear interface are formed between the composite layer and the bulk. The formation of a clear interface between the composite layer and the bulk indicates that the polymer is diffusing into the CNT agglomerates. The formation of vacancies and very different optical and diffusion properties of the CNTs and the polymer are believed to have the effect to increasing diffusion in the proximity of CNTs and to separate the tubes leading to a homogeneous dispersion. The thickness of the composite layer has been determined by cross sectional TEM for a MWNT/PEEK surface layer. While TEM from DWNTs in PEEK is challenging due to their small diameter, Raman spectroscopy has been able to map the uniform distribution of the CNTs across the layer and estimate the thickness of the composite layer. Electronic transport measurements show that annealing increases the conductivity by one to two orders of magnitude depending on the number of tubes deposited on the surface.

Conclusions

Using Raman spectroscopy I was able to extract information about the interaction of DWNTs with the surrounding sulfuric acid molecules. The inner tube is a strain probe while the outer tube which is in contact with the environment, is sensitive to strain and charge transfer. DWNTs can be used as a molecular sensor, in particular, to study nanocomposites. DWNTs were studied in PEEK to monitor the dispersion of the tubes in the polymer. Using micro-Raman mapping information could be accessed at the millimeter and micrometer scale which cannot be revealed by optical microscopy. So far Raman spectroscopy, when applied to nanocomposites as such, is considered not informative enough. Indeed, one simple Raman spectrum is not sufficient to characterize a composite material. But considering an accurate Raman mapping, I developed a statistical analysis that opens new opportunities in nanocomposite characterization. Statistical analysis requires thousands of spectra recorded at different scales. Each spectrum needs to be fitted appropriately by selecting the right set of parameters. That means the results do not depend on the model and starting values of the fit. At the same time the number of parameters needs to be kept as low as possible which requires prior testing and developing of fitting routines. To interpret the data correctly previous theoretical and experimental findings in graphene and nanotubes have to be considered carefully. By combining the Raman results with TEM and electrical transport or nano-indentation measurements as well as elastic neutron scattering, allows to go further in data interpretation. In this work I was able to study two specific nanocomposites: CNTs in a polymer and a metallic matrix.

For DWNTs in copper, the choice of the Raman band to characterize the nanotubes in a composite has been not trivial. Both D and G bands can be analyzed to obtain information about the sample. The G band was analyzed through three contributions G_o^+, G_i^+ and D'. When all parameters of the bands (frequency, line width, intensity) are left free, one finds that the histogram of the G_o^+ band frequency is narrow indicating no spectral shift. This means there is no charge transfer. This statistical analysis allowed to fix the frequencies and line widths of the G^+ bands of the inner and outer tubes and the D' band increasing the accuracy of the fitted intensity distribution across the Raman map. The ratio of intensities of the D' over the D band in association with the ratio of the intensities of the D over the G band was used to obtain information about the state of the tubes. It could finally be concluded that the interlayer spacing between the inner and outer tubes is reduced after the wear tests. It was shown that the tubes are not transformed into amorphous carbon although intense wear did increase the number of defects.

In the case of a polymer composite the G band was usually used to indicate the presence of CNTs. But in this work I find that at low CNT concentration the G band is masked by the inelastic scattering from the PEEK polymer. In contrast the D band frequency is located in a range where no other vibrations of the polymer are present. Furthermore, its frequency can be adjusted by changing the exciting energy. I chose the near infrared excitation of the D band to reduce overheating of the sample. The average value and the standard deviation of the histogram of the ratio of the D band over the background provide information about the concentration and the homogeneity

of CNT dispersion. An important step in the analysis was to utilize the background signal as an indicator for the matrix which can be used in the statistical analysis.

Annealing experiments on the surface of PEEK show that the tubes self-disperse in the PEEK polymer. With TEM we observe that the PEEK polymer covers the tubes at the surface and the CNT diffusion layer has a sharp interface with the polymer. This is also seen in Raman maps across the composite layer. The self-dispersion of the tubes has been verified on different types of CNTs. It is proposed that high infrared absorption of CNTs leads to enhanced diffusion of PEEK in the vicinity of the tubes enhancing diffusion of the polymer into the CNT agglomerates. This mechanism of self-diffusion provides a possible explanation of the dynamic percolation phenomenon. The self-dispersion of CNTs when annealing is a promising method to make thin electrically conducting composite surface layers and opens an interesting perspective to repair surfaces by infrared laser heating.

Résumé

Cette partie en français est un résumé du manuscrit précédent rédigé en anglais. Il ne comporte pas d'information nouvelle.

Introduction

Un matériau composite est un système multi-composants dans lequel les composants de nature très différente sont mélangés pour former un nouveau matériau avec des propriétés améliorées. Il existe deux grandes catégories de matériaux constitutifs des composites: la matrice et la charge. La matrice entoure et soutient la charge tandis que la charge modifie ses propriétés mécaniques et ses propriétés physiques particulières (résistance, rigidité, conductivité, etc) afin d'améliorer la matrice.

Les composites à matrices organiques (CMO) sont intéressants pour les industries aéronautiques et de transports en raison de leur légèreté et de leur résistance mécanique. L'utilisation de matériaux composites à la place d'alliages métalliques permet de réduire la consommation de carburant et les coûts de fabrication. Mais la plupart des polymères à haute performance utiles pour des applications aérospatiales sont des isolants électriques. L'incorporation d'une petite quantité de nanotubes de carbone (NTC) bien dispersés peut augmenter significativement la conductivité du polymère. Le seuil de percolation (conductivité électrique) aussi bas que 0.002% en poids a été observé avec une matrice époxy. Actuellement, les CMO sont le plus grand domaine d'application des NTC. Combiner les propriétés de la matrice et de la charge est recherché lors de la conception d'un nanocomposite. Cependant, les propriétés de la charge sont fonction de l'état d'agglomération des particules. Les NTC ont tendance à s'agglomérer à cause de leur rapport d'aspect important et d'une grande surface spécifique rendant la dispersion difficile. En outre l'incorporation de charges dans un polymère thermoplastique augmente sa viscosité rendant la dispersion encore plus difficile.

La stabilité thermique des NTC permet de les introduire dans une matrice métallique. La ténacité élevée des nanotubes de carbone dans un composite de métal peut être utilisée pour réduire les pertes matérielles causées par le frottement et l'usure, l'un des défis d'ingénierie dans les systèmes mécaniques actuellement. Nous avons pu montrer dans le cadre de ce travail que l'incorporation d'une petite quantité de nanotubes double-paroi (abrégé sous le sigle DWNT) dans le cuivre conduit à une amélioration significative des propriétés tribologiques telles que les micro dureté et la lubrification conduisant à une réduction du volume d'usure. Établir une relation entre les caractéristiques du NTC et le comportement macroscopique de composites est également crucial pour le renforcement mécanique de fils de cuivre pour les bobines de champ magnétique élevé.

Pour avoir une meilleure compréhension au niveau fondamental, il faut étudier le nanocomposite à des échelles microscopiques et macroscopiques. Le comportement macroscopique, comme la conductivité électrique ou la déformation à la traction, dépend de la structure à l'échelle du micromètre. Cependant, il est souvent difficile d'imager les nanoparticules dans une matrice et de surveiller leur interaction. Les outils de recherche élaborés tels que la diffusion de neutrons, les installations de rayonnement

synchrotron et de microscopie électronique avancée sont très coûteux, tandis que la spectroscopie Raman est un outil polyvalent et simple. La spectroscopie Raman offre plusieurs avantages pour l'analyse microscopique. Comme il s'agit d'une technique de diffusion, les spécimens n'ont pas besoin de préparation primaire telle que la coupe, le traitement de surface ou d'amincissement. Les spectres Raman peuvent être recueillis à partir d'un volume très faible (<1 μm de diamètre). Les bandes spectrales permettent l'identification d'un composé présent dans un endroit spécifique de la surface et du volume.

La spectrométrie Raman est également largement utilisée dans la caractérisation de nanomatériaux de carbone. La spectroscopie Raman peut être très sensible permettant d'observer un seul NTC de 1,2 nm de large avec seulement 10^5 atomes. Les NTC ont un fort signal Raman avec plusieurs bandes spectrales caractéristiques qui peuvent être utilisées pour indiquer les modifications du NTC lorsqu'il est soumis à une influence extérieure. Les NTC peuvent à leur tour être utilisés comme un outil pour sonder leur environnement. Un tube mono-paroi (abrégé sous le sigle SWNT) ne peut pas servir de capteur local puisque tous les atomes sont situés sur la surface, un NTC multi-parois (abrégé en MWNT) non plus en raison du fait que la plupart des atomes sont à l'intérieur et n'interagissent pas directement avec l'environnement. Dans le cas du DWNT, le tube extérieur est exposé à l'environnement tandis que le tube intérieur ne l'est pas. A partir des signatures des tubes intérieur et extérieur, nous pouvons considérer que les DWNTs sont des capteurs moléculaires.

Dans cette thèse, j'ai d'abord étudié les DWNTs comme capteurs moléculaires puis leurs utilisations possibles dans des nanocomposites. Deuxièmement, j'ai étudié l'usure des composites NTC/cuivre et dans la troisième partie j'ai étudié la dispersion des NTC dans une matrice de polymère et la modification induite du polymère en raison de la présence des NTC.

1. Matériaux composites

La conductivité électrique des composites NTC / PEEK

Le polyether ether cétone (abrégé sous le sigle PEEK) est un polymère thermoplastique semi-cristallin intéressant pour les applications aéronautiques. Le PEEK pur est un polymère isolant (σ ~10^{-15}-10^{-13} S/cm [70]), qui devient conducteur électrique avec l'incorporation de NTC. Avec l'augmentation de la concentration de NTC, le nombre de contacts entre les NTC augmente et l'épaisseur du film de PEEK entre NTC adjacents diminue, ce qui se traduit par une conductivité électrique plus élevée. En continuant d'augmenter la concentration de NTC, le seuil de percolation est atteint, la conductivité électrique augmente alors rapidement et peut être décrite par une équation de percolation classique:

$$\sigma = \sigma_0 (p - p_c)^t$$

où σ_0 est le facteur d'échelle de la conductivité lié à la conductivité intrinsèque de la matière de remplissage, p représente la concentration de la charge conductrice, p_c est le seuil de percolation et t est l'exposant critique reflétant la dimensionnalité du système du composite [70].

Selon la théorie de la percolation, pour une répartition aléatoire des NTC avec un rapport d'aspect typique $\eta = 1000$, la notion de volume exclu donne un seuil de percolation statistique $p_c \sim 0.7/\eta \sim 0.07\%$ en poids [72]. Des seuils de percolation

inférieurs de manière significative à cette valeur sont attribués à la percolation dynamique [73], ce qui permet un mouvement de particules et une réagrégation.

Les conditions de traitement - en particulier le temps et la température - peuvent fortement modifier les valeurs de seuil de percolation de la conductivité et de composite [67] [68]. Ce phénomène résulte de l'aptitude des charges à "l'auto assemblage" [68] dans la matrice en fusion ou dans la matière thermodurcissable, avant le durcissement [69], et est connu dans la littérature comme "percolation dynamique".

Combessis *et al.* [67] ont rapporté un cas d'une composite de polypropylène de très faible densité. Avec le temps de recuit, la conductivité électrique σ du composite augmente graduellement, tandis que le seuil de percolation p_c efficace diminue (Figure A.1.1).

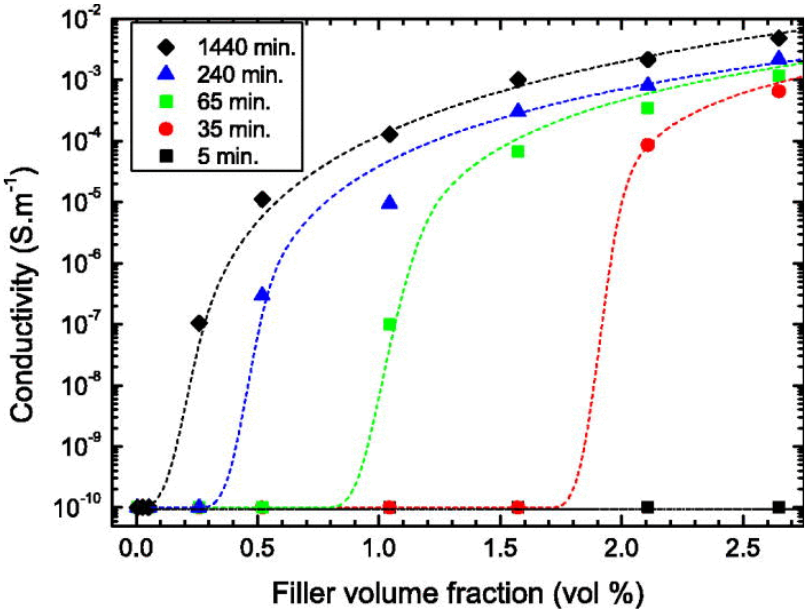

Figure A.1.1. Conductivité en fonction de la quantité de charge mettant en évidence la transition de percolation après chaque étape de recuit (5, 35, 65, 240, 1440 min). La fraction de la charge critique ("seuil de percolation") est réduite par un facteur d'au moins dix, tandis que la conductivité électrique a gagné plus de sept ordres de grandeur [67].

L'augmentation de la conductivité a été associée à une réorganisation de la charge à l'état fondu, et la formation et la croissance d'un réseau de percolation. L'auto-organisation a été observée pour induire une divergence de l'exposant critique *t*. La valeur de *t* a été trouvée généralement plus élevée que la valeur universelle 2, en particulier pour les systèmes avec de faibles p_c. Les valeurs qui s'écartent de la valeur universelle de 2 ont été proposées pour être un indicateur du degré d'achèvement du processus de l'organisation [67].

La percolation dynamique peut être considérée comme une transition d'un système métastable obtenu par mélange à un système thermodynamiquement plus stable, dans lequel les tensions internes ou les énergies libres de l'ensemble sont réduites.

Dans la littérature, il a été rapporté que le seuil de percolation se trouve dans une vaste gamme de pourcentages en poids de NTC, en fonction du type de polymère, de la technique de traitement et du type de NTC utilisés. Les systèmes thermoplastiques percolent généralement autour de 1-5% en poids [49].

Pour le composite SWNT@PEEK, Diez-Pascual *et al.* [76] ont observé un faible seuil de percolation (moins de 0,1% en poids) et la conductivité électrique à température ambiante de 10 à 2S·cm^{-1} pour 1% en poids de nanotubes.

Le seuil de percolation de nanocomposites DWNT@PEEK a été trouvé aux alentours de 0,25% en poids pour les composites préparés avec une extrudeuse bi-vis (Figure A.1.2a) [77]. La conductivité maximale du composite à la température ambiante pour 2% en poids de DWNTs était d'environ 3×10^{-2}S·cm^{-1}.

Pour les composites MWNT@PEEK fabriqués en utilisant le mélange en fusion, Bangarusampath *et al.* [49] ont observé une percolation à 1,3% en poids avec une conductivité de 10^{-2}S·cm^{-1} pour 2% en poids de MWNTs (Figure A.1.2b). La valeur de conductivité de 1S·cm^{-1}, requise pour les applications électrostatiques, a été atteinte avec un chargement de 17% en poids.

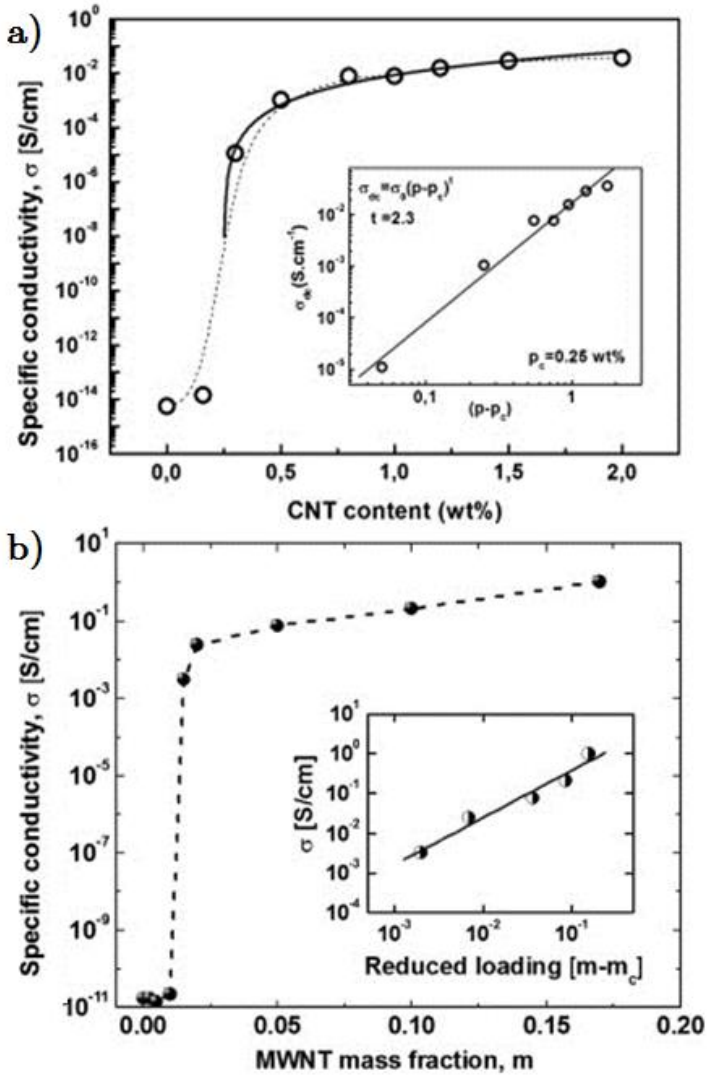

Figure A.1.2. Conductivité électrique de a) DWNT @ PEEK [77] *b) MWNT@PEEK* [49] *en fonction de la fraction en poids de NTC.*

Les défis de la dispersion et la quantification

Une répartition homogène des NTC dans un composite est essentielle, car elle est responsable des propriétés isotropes du composite. Mais les dimensions nanométriques, le grand rapport d'aspect et la flexibilité élevée des NTC font de la dispersion un défi. Les NTC sont agglomérées avec une énergie de liaison de van der Waals de ~500 eV par micromètre de contact tube-tube [81]. Lors de la fabrication d'un composite le grand rapport d'aspect de NTC induit une viscosité élevée du polymère à l'état fondu, qui à son tour affecte leur dispersion uniforme [80]. Dans les matériaux composites les NTC ont une forte tendance à se réunir et former des agglomérats micrométriques, ce qui affecte négativement les propriétés mécaniques des nano-composites.

Outre la difficulté d'obtenir des dispersions de NTC stables et homogènes, une autre complication est de trouver une méthode efficace pour évaluer et quantifier l'état de dispersion. Une caractérisation complète aux échelles nano(micro)-scopiques et macroscopiques est fondamentale pour obtenir des informations sur les changements induits dans le polymère avec l'ajout de NTC. Cependant, il n'y a guère d'études sur la quantification de la dispersion dans les composites à base de NTC. La plupart des chercheurs ont mentionné une dispersion uniforme des NTC dans les composites qui se fonde sur l'examen visuel de la microstructure. La quantification du degré ou la qualité de la dispersion des NTC sont importantes car elles permettent de comparer différentes microstructures et l'efficacité des différentes méthodes de dispersion des NTC dans les composites.

Récemment, Tishkova *et al.* [77] ont proposé d'utiliser la spectroscopie Raman pour accéder à l'état de dispersion de DWNTs dans une matrice de polymère PEEK. Plusieurs cartes Raman à différentes échelles et de différentes régions ont été réalisées. L'interaction entre le tube extérieur avec la matrice a été évaluée à partir de la forme de la bande G Raman. Cela a permis aux auteurs de distinguer les régions où les nanotubes sont bien dispersés et les régions où les nanotubes sont agglomérés.

2. Méthodes expérimentales

Spectroscopie Raman de nanotubes de carbone

La diffusion Raman est une diffusion inélastique du rayonnement électromagnétique incident sur les phonons du matériau. Deux fréquences qui n'étaient pas présentes dans la lumière incidente apparaîtront dans la lumière diffusée. Les nouveaux composants peuvent être calculés à la fréquence de la lumière incidente plus (Anti-Stokes shift) ou moins (Stokes shift) la fréquence du phonon. Les fréquences des phonons sont spécifiques pour chaque matière et dépendent de sa structure et de sa composition. Ainsi, la spectroscopie Raman est très sélective, ce qui permet d'identifier et de différencier les molécules et les espèces chimiques qui sont très similaires.

Les spectres Raman de NTC ont un certain nombre de bandes spectrales qui permettent de distinguer les spectres mesurés sur les échantillons vierges (qui idéalement sont exempts de défauts, non dopés, sans contrainte) et ceux mesurés sur des échantillons soumis à des perturbations externes comme les champs électrique et magnétique ou contiennent des défauts. Les spectres Raman typiques de faisceaux de NTC mono-paroi, double-paroi et multi-parois sont présentés dans la Figure A.2.1.

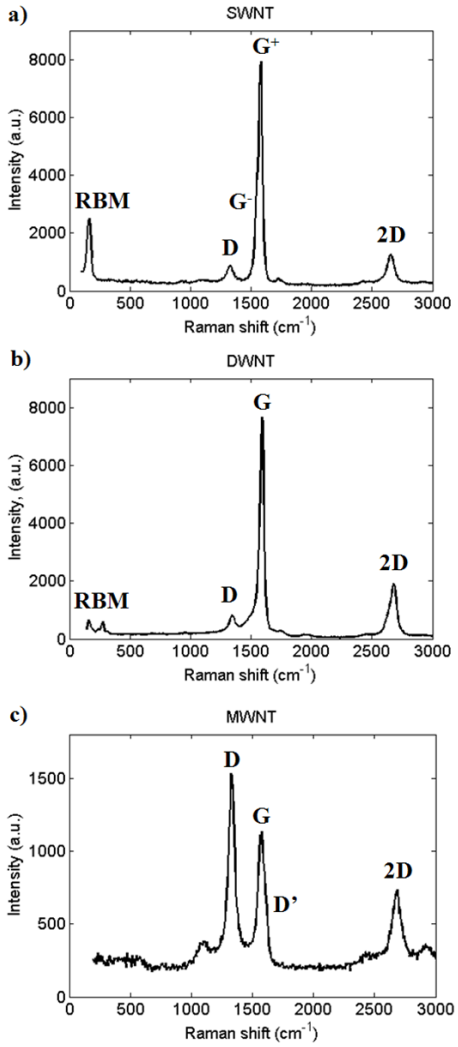

Figure A.2.1. Spectres Raman typique de CNT en faisceaux excité avec λ = 532nm a) mono-paroi b) double-paroi et c) multi-parois.

Mode de respiration radiale

Les modes de respiration radiale (en abrégé RBM) sont présents dans les NTC et ils sont visibles sur les spectres dans les basses fréquences (entre 120 et 350cm^{-1}). Ils correspondent à des oscillations radiales des atomes de carbone (Figure A.2.2).

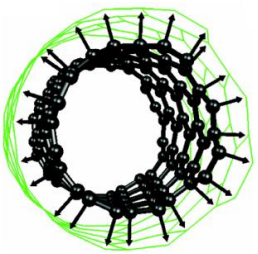

Figure A.2.2. Mode de respiration radiale d'un nanotube (8, 4). Les flèches indiquent le déplacement des atomes de carbone au cours de la vibration [96].

Les RBM peuvent être utilisés pour obtenir des informations sur le diamètre (d_t) des nanotubes mono-paroi (SWNT) par leur fréquence (ω_{RBM}):

$$\omega_{RBM} = \frac{A}{d_t} + B$$

où A et B sont des paramètres déterminés expérimentalement. Pour un ensemble typique des NTC mono-paroi avec une gamme de diamètre 1,5 ± 0,2nm, A = 234cm^{-1}, B = 10cm^{-1} [97]. Le paramètre B est attribué à l'interaction tube-tube. Pour un SWNT isolé sur un substrat en Si, A = 248cm^{-1} et B = 0 [98].

Bande Raman G

L'une des principales caractéristiques des bandes de NTC est la bande G, qui est la bande la plus intense et qui est située entre 1570 et 1600cm^{-1}.

A la différence de la bande G du graphène, qui présente un seul pic lorentzien à 1582cm^{-1} dû aux vibrations tangentielles des atomes de carbone, la G-bande de SWNT se divise en deux sous-groupes: la bande G^+ (~ 1590cm^{-1}) et la bande moins intense G^- (~ 1530-1570cm^{-1}).

Pour les DWNTs, il y a deux contributions principales attribuées aux deux modes G^+ qui sont situés à 1592cm^{-1} pour le nanotube externe et à 1581cm^{-1} pour le nanotube interne. Les bandes G^+ se chevauchent à la pression normale et se divisent quand la pression augmente [107]. Les G^- modes sont plus faibles en intensité et sont situés aux plus basses fréquences.

Alors que la division G^+ - G^- est grande pour les tubes de petit diamètre, la division de la bande G pour les grands diamètres de MWNT est à la fois petite et masquée par l'élargissement des bandes en raison de la distribution de diamètres et un grand nombre de défauts. Par conséquent, la bande G présente une forme de ligne caractéristique faiblement asymétrique, avec un pic apparaissant à la fréquence de graphite à 1580cm^{-1}.

Il y a plusieurs effets qui peuvent être vus avec la bande G. Les principaux effets sont les suivants: contrainte (conduisant à un déplacement de la bande G), dopage (conduisant à un décalage qui dépend des espèces en interaction avec le tube et aussi du déplacement du niveau de Fermi [109], [107]) et du changement de température (ce qui conduit à un déplacement, avec un taux de -0,024cm^{-1}/K, à l'exception des phonons hors-équilibre) [110].

Bandes Raman D et D'

L'origine de la bande D dans le graphite et des nanotubes de carbone est attribuée à un processus de double résonance impliquant un défaut. La diffusion de l'électron entre deux points K inéquivalents (inter-vallée) de la zone de Brillouin du graphène, K et K', conduit à la bande D, tandis que la diffusion à proximité du même point K (intra-vallée) conduit à la bande D' (~ 1610-1620cm^{-1}) (Figure A.2.3).

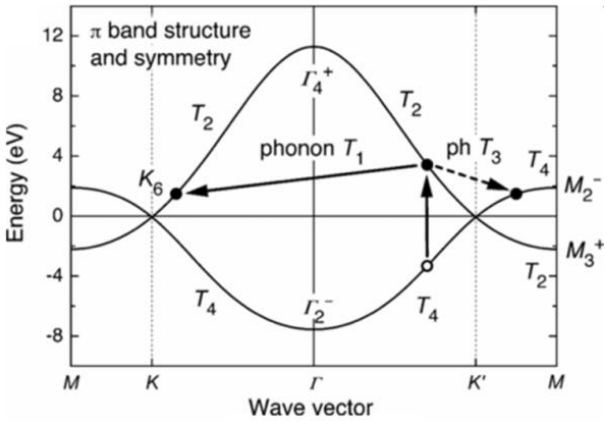

*Figure A.2.3. Bandes π et π * électroniques du graphène le long de Γ-K-M. La symétrie des bandes est donnée* [111].

La bande D dans le spectre Raman est présente à la fréquence $\omega_D = 1350cm^{-1}$ à $\lambda =$ 515nm (2.41eV) et est elle dispersive avec l'énergie du laser d'excitation [112]:

$$\frac{\Delta\omega_D}{\Delta E} = \frac{60cm^{-1}}{eV}$$

La spectroscopie Raman permet de sonder la nature du défaut dans le graphène par des pics de défauts activés D et D'. Eckmann *et al.* [117] ont présenté une analyse détaillée des spectres Raman du graphène contenant différents types de défauts. Ils ont trouvé que le rapport d'intensité $I_D/I_{D'}$ est maximal (~ 13) pour des défauts sp^3, il diminue pour des défauts lacunaires (~ 7), et il passe par un minimum pour les bords (~ 3,5).

Bande Raman 2D

La première harmonique de la bande D provient d'un processus de double résonance impliquant maintenant 2 phonons et est observée dans la région de 2450 - 2650cm^{-1}. Pour l'activation de la bande 2D, il n'est pas nécessaire d'avoir des défauts. Les règles de sélection Raman fondamentales sont satisfaites si la somme des deux vecteurs d'onde des phonons est égale à zéro.

Dans le cas de nanotubes de carbone, la structure de la bande 2D est fortement dépendante du nombre de parois. Les SWNT montrent un pic 2D fortement semblable à celui mesuré pour le graphène [121]. Pour les DWNT, les contributions internes et externes ne sont pas situées au même endroit menant aux changements globaux de forme. L'interaction électronique entre les couches peut aussi jouer un rôle.

DWNT comme capteur moléculaire

La bande G d'un DWNT est relativement large grâce aux contributions des tubes intérieurs et extérieurs. En utilisant une pression élevée, il est possible d'observer le dédoublement de la large bande G en au moins deux bandes G^+ provenant des tubes intérieurs et extérieurs. Lorsque les positions spectrales des tubes intérieurs et extérieurs sont bien séparées, les petites variations de la bande G^+ du tube extérieur peuvent alors être bien détectées. Les contributions supplémentaires sont attribuées

aux bandes G^-. Elles sont plus faibles en intensité et leurs positions respectives sont affectées par le couplage entre les tubes.

Le tube intérieur n'estime que la déformation transmise par le tube extérieur tandis que la bande G^+ du tube extérieur est influencée à la fois par la variation de la longueur de la liaison (déformation) et la position du niveau de Fermi (couplage électron-phonon). En comparant les variations spectrales du tube intérieur et extérieur, on peut détecter le transfert de charge du tube avec son environnement. Ainsi les DWNTs peuvent être considérés comme des capteurs moléculaires.

Nous avons utilisé ce nano-capteur idéal dans le cas de superacide pour déterminer la relation entre le transfert de charge f_C et le décalage Raman de la bande G^+. Au début, on déduit la contrainte induite du déplacement du tube extérieur à partir du déplacement du tube intérieur à l'aide de l'équation suivante [107]:

$$\Delta\omega_{externe} = 1.7\,\Delta\omega_{interne}$$

Ensuite, en utilisant la haute pression [125] et des expériences de neutrons [126] nous avons déduit le transfert de charge à partir de la déformation du tube extérieur. Le décalage de la bande G pour le nanotube extérieur, $\Delta\omega$, comme une fonction linéaire de transfert de charge de trous par atome de carbone, f_C, s'est révélé être:

$$\Delta\omega\ (\mathrm{cm}^{-1}) = (350 \pm 20) f_C + (101 \pm 8)\sqrt{f_C}$$

Le décalage restant est dû au couplage électron-phonon.

Ce résultat a également été utilisé par Tishkova *et al.* [77] pour sonder la dispersion de DWNT dans une matrice de polymère.

3. Résultats et discussion

3.1 Composite CNT @ cuivre

L'incorporation de DWNT dans le cuivre améliore les propriétés mécaniques du métal, en particulier, la résistance à l'usure. Le Tableau A.3.1 présente les propriétés mécaniques de DWNT@Cu et de cuivre pur. On peut voir que les composites DWNT@Cu présentent une microdureté supérieure, un plus faible coefficient de frottement et une plus faible usure par rapport au Cu pur.

Propriétés	Cu	DWNT@Cu
Microdureté Vickers	50	82
Coefficient de frottement (pour une charge de 5N)	0.78	0.24
Perte de volume (mm^3)	0.45	0.044
Perte de masse (mg)	4.03	0.36
Taux d'usure normalisé (mg/m·N)	0.027	0.003

Tableau A.3.1. Propriétés de Cu et DWNT@Cu composite.

Afin de faire la lumière sur le rôle et l'état des NTC, nous procédons à une étude Raman détaillée à l'extérieur et à l'intérieur des zones d'usure. La Figure A.3.2 montre deux spectres Raman caractéristiques pour le composite DWNT@Cu à l'intérieur et à l'extérieur de la zone d'usure par frottement. En dehors de la zone d'usure par

frottement, on observe un fort signal de fond, tandis qu'à l'intérieur de la zone d'usure par frottement le signal de fond est considérablement réduit et les bandes spectrales des NTC sont plus intenses.

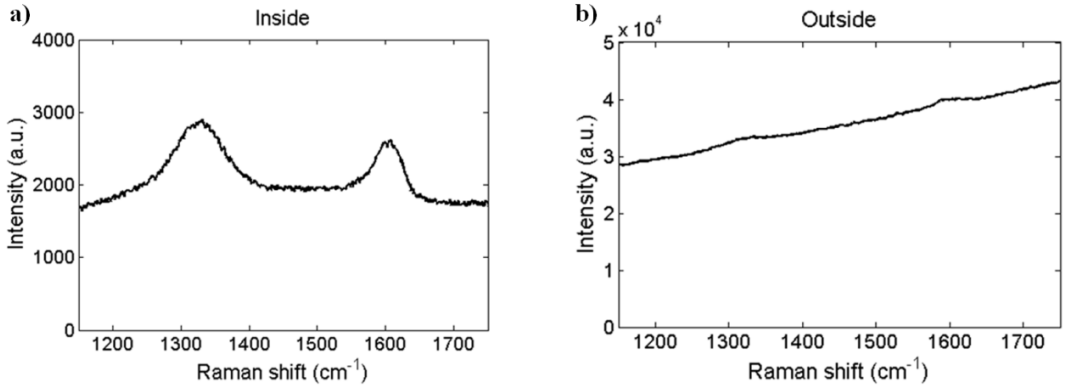

Figure A.3.2. Les spectres Raman typiques sans soustraction du fond a) à l'intérieur, et b) à l'extérieur de la zone d'usure par frottement.

Pour bien comprendre l'origine du signal de fond et en particulier pour comprendre si c'est du signal Raman, on a enregistré les spectres Raman Stokes et anti-Stokes à différentes longueurs d'onde d'excitation. La température peut être estimée en prenant l'intensité relative des spectres Stokes et anti-Stokes en utilisant l'équation suivante [95]:

$$T = \frac{\hbar\omega}{k_B} \ln \frac{I_S}{I_{AS}}$$

Pour notre échantillon, nous avons déduit les températures de 500-700K à l'intérieur et à l'extérieur de la zone d'usure par frottement en fonction du lieu.

Aucun changement dans le signal de fond n'est observé lors de l'utilisation des longueurs d'onde 514nm et 488nm du laser d'excitation. Cela montre que le signal de fond n'est pas causée par la luminescence mais par la diffusion inélastique de phonons et d'électrons. Le signal de fond élevé dans les zones sans usure par frottement est attribué à la présence d'une plus grande quantité de cuivre. Le signal de fond plus faible et les bandes Raman plus élevées montrent donc que la fraction de NTC est plus élevée dans la zone d'usure par frottement.

Les signaux des DWNTs ont une forme caractéristique de la bande G due aux tubes interne et externe [146]. La largeur à mi-hauteur et l'intensité de la bande G dans la zone d'usure par frottement indiquent que les NTC sont encore sous forme cylindrique et ne sont pas transformés en carbone désordonné.

Nous avons remarqué que lorsque l'on ajuste le spectre avec une seule lorentzienne dans la gamme spectrale de la bande G, les changements du spectre sont incompatibles avec les décalages spectraux de la bande D. Nous rappelons que les DWNTs bruts montrent une bande G_i^+ du tube intérieur situé à 1581cm^{-1} et une bande G_o^+ du tube extérieur situé à 1592cm^{-1} (Figure A.3.3).

Nous avons pris des spectres avec deux longueurs d'onde d'excitation différentes (532 et 632nm) pour comprendre l'origine de la plus forte contribution à la bande G.

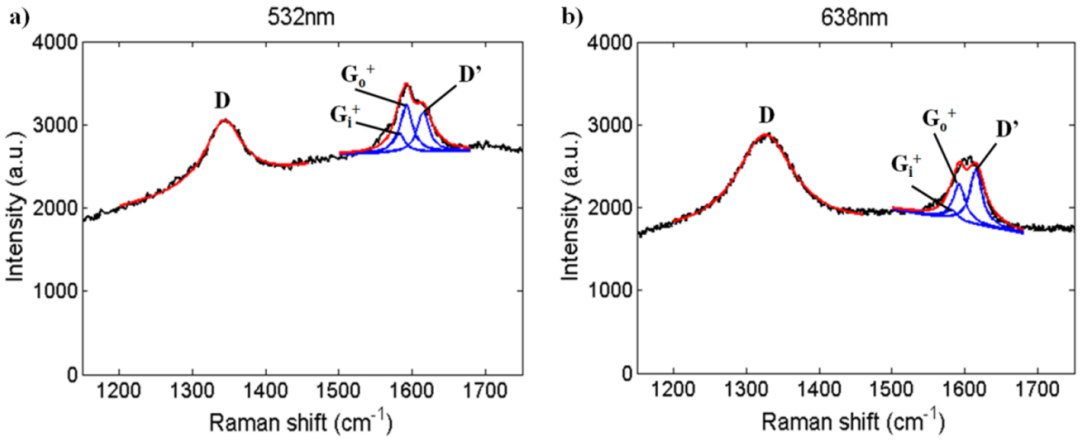

Figure A.3.3. Les spectres Raman de composite DWNT/Cu à l'intérieur de la zone d'usure par frottement pris avec différentes longueurs d'onde a) 532nm b) 638nm. Le signal Raman des DWNT est composés de la bande D induite par les défauts et de la bande G. La bande G possède à la fois les contributions des tubes interne et externe (G_i^+, G_O^+). La bande D' est également causée par les défauts.

Nous constatons que la contribution, D', augmente en intensité relativement à la bande G avec la longueur d'onde d'excitation. Par conséquent, ce groupe n'est pas causé par le même processus que la bande G et ne doit pas être attribué à la contribution G_o^+ et à un transfert de charge important.

Nous avons utilisé une longueur d'onde d'excitation de laser de 638nm, puisque les intensités des bandes D et D' sont plus larges par rapport à celles obtenues avec des plus petites longueurs d'ondes [147], ce qui rend plus facile de séparer la bande D' des bandes G^+.

Les images Raman de taille 100µm × 100µm avec un pas de 5µm ont été enregistrées sur la zone d'usure par frottement. Nous avons ajusté tous les spectres Raman obtenus à partir d'une carte Raman et décidé de fixer certains paramètres afin de réduire les incertitudes. Donc, nous avons fixé les largeurs des raies et les positions spectrales.

Alors que la bande D est une simple lorentzienne, nous pouvons déterminer la position et l'intensité spectrale. Nous pouvons enfin comparer les intensités intégrées.

Nous avons tracé la position spectrale de la bande D, et les rapports des intensités intégrées ($A_{D'}/A_D$) et (A_D/A_G) sur la Figure A.3.4.

Récemment, il a été montré que le rapport de l'intensité intégrée $A_{D'}/A_D$ pourrait être une indication de la nature des défauts. Un petit rapport $A_{D'}/A_D$ est dû à des défauts sp^3, un rapport $A_{D'}/A_D$ intermédiaire à des lacunes et un grand rapport $A_{D'}/A_D$ à de gros défauts structurels [117].

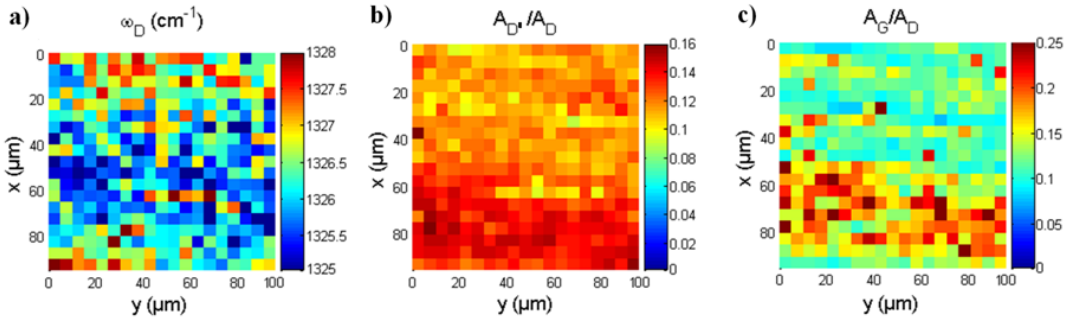

Figure A.3.4. Cartes Raman (100×100 micromètres) dans la zone d'usure par frottement a) la position de la bande D b) l'intensité relative de la bande D' ($A_{D'}/A_D$, utilisant l'intensité intégrée) et c) de la bande G (A_G/A_D, utilisant l'intensité intégrée).

Lors du balayage du spot laser sur la surface (100µm × 100µm), nous constatons que la bande D se déplace légèrement à l'intérieur de la zone d'usure par frottement indiquant des variations de contraintes résiduelles (Figure A.3.4a) et le décalage de la bande D est corrélé avec l'augmentation de l'intensité relative de la bande D' (Figure A.3.4b).

Nous notons que le D (D') peut être expliqué par les processus de double résonance inter(intra) vallées [148]. L'intensité de la bande D' est supposée augmenter lorsque l'interaction entre les couches est forte. Cette légère augmentation de la D' peut donc être attribuée à une diminution de l'espacement entre les couches compatibles avec une contrainte résiduelle plus faible. Cela est conforme au plus élevé rapport A_D/A_G indiquant un plus grand nombre de défauts (Figure A.3.4c). Des travaux complémentaires sont nécessaires pour confirmer cette interprétation.

La spectroscopie Raman révèle que le cuivre est retiré et la quantité de matériau de carbone est plus élevée dans la zone d'usure par frottement. Nous concluons que ce matériau de carbone est encore sous la forme de nanotubes de carbone de forme cylindrique intacts bien que l'usure intense augmente le nombre de défauts dans les NTC. Si les NTC étaient détruits, la bande G serait beaucoup plus large. En général, l'élargissement de la bande G augmente lorsque la taille caractéristique des domaines est inférieure à 10nm. Si les nanotubes sont cassés, le domaine de taille doit être de l'ordre de la circonférence, i. e. autour de $2\pi r = 6$nm.

3.2 Composite CNT @ PEEK

Dans cette partie, nous étudions les modifications mécaniques d'un faisceau polyéther éther cétone modifié électriquement avec des nanotubes de carbone multi-parois. Nous utilisons la calorimétrie différentielle à balayage (DSC), la nano-indentation, l'imagerie Raman étendue, et la diffusion de neutrons aux petits angles pour corréler la rupture et les variations de la dureté avec les changements dans la concentration de nanotubes de carbone. L'analyse statistique des intensités spectrales Raman est utilisée pour estimer la concentration locale du tube et de la cristallinité du polymère.

La Figure A.3.5 illustre les mesures de conductivité électrique faites en collaboration avec l'IPREM. La conductivité électrique augmente de plus de huit ordres à 0,5% en poids de NTC et se stabilise à 2% en poids indiquant un seuil de percolation à environ 1%.

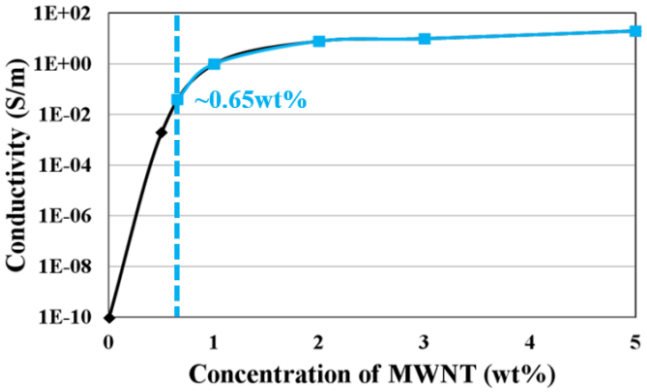

Figure A.3.5 Dépendance de la conductivité électrique avec la teneur en MWNTs.

L'introduction de MWNTs en PEEK induit un changement radical dans le comportement mécanique du PEEK. Il change de ductile ($\varepsilon_{fracture}$ = 28,6%) sans tubes à semi-fragile ($\varepsilon_{fracture}$ = 5%) quand il contient 0,5% en poids de MWNT (Figure A.3.6).

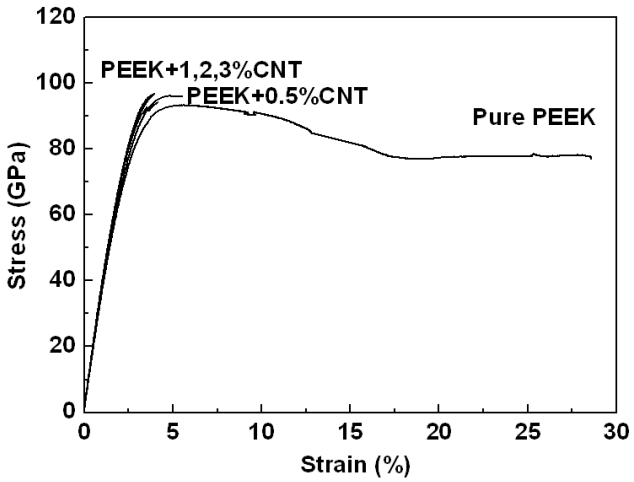

Figure A.3.6. Courbe d'élongation avec différentes quantités de NTC dans le PEEK et comparaison avec la matrice de PEEK pur.

Les mesures de DSC montrent que le taux de cristallinité est sensiblement le même (32%), dans le volume de la poutre et entre le cœur et la surface extérieure (bord) de la poutre de manière indépendante du contenu des NTC. Nous concluons donc que la réduction du régime de ductilité n'est pas causée par une augmentation de la cristallinité du polymère.

Pour voir si la rupture est provoquée par la distribution non homogène des nanotubes de carbone dans le polymère, on a effectué des expériences de micro-indentation sur le bord et au centre des échantillons. Les mesures montrent que les bords sont moins durs que le centre du composite. La micro-dureté varie de 10 à 15% entre le centre et le bord de la poutre. Nous avons vérifié que le PEEK sans NTC ne montre aucune différence de dureté au niveau du bord et le centre de la poutre. Ce résultat suggère que la variation de la dureté est due à une variation dans le taux de NTC dans la poutre.

Nous avons utilisé la spectroscopie Raman pour déterminer directement le contenu de NTC à différents endroits du faisceau. Les images Raman de taille 400µm × 400µm

avec un pas de 4.6µm ont été enregistrées (84×84 = 7056 spectres). Les Figures 3.7a-b montrent des exemples de spectres Raman obtenus pour le PEEK pur et le PEEK avec NTC.

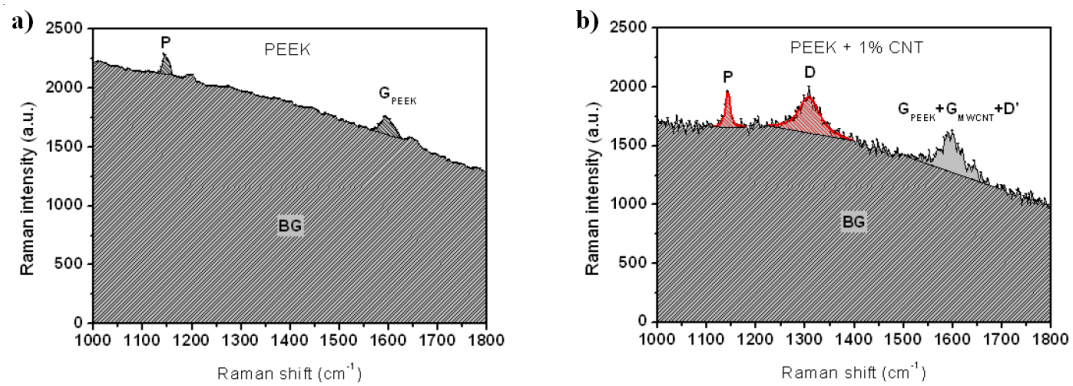

Figure A.3.7. Spectres Raman typiques pour un a) PEEK pur b) PEEK avec MWNT.

Trois bandes Raman sont observées: les bandes D et G provenant du NTC [154] et une bande étroite à 1144cm^{-1} provenant du polymère. Cette dernière correspond à la vibration d'étirement C-O-C asymétrique dans le polymère PEEK [115] et est dénommée dans la suite la bande P. Dans le PEEK pur, on peut également observer une bande G moins intense (nous gardons ce nom pour plus de simplicité) en raison de la présence de sp^2 liés carbone dans le cycle de benzène du polymère. Le signal de fond dans les spectres de PEEK est causé par la luminescence du PEEK et par le signal Raman du polymère PEEK amorphe. La ligne sous le pic (Figure A.3.7a-b) indique la limite du signal de fond.

Puisque le PEEK n'a pas de bande D, nous utilisons la bande D comme indicateur de la présence de NTC. Pour l'analyse statistique, nous avons ajusté la bande D et la bande P avec des lorentziennes (lignes rouges dans la Figure A.3.7b) et calculé leurs intensités intégrées ainsi que le signal de fond (BG). Les intensités intégrées sont représentés sur les cartographies de la Figure A.3.8. Les parties sombres correspondent aux intensités plus faibles tandis que les zones les plus claires correspondent aux intensités plus élevées.

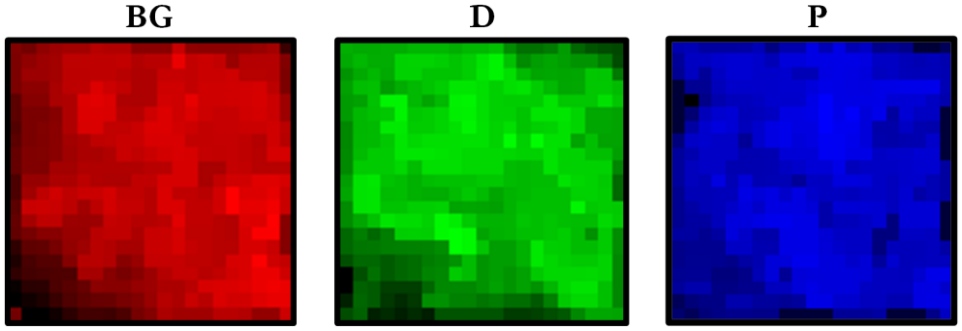

Figure A.3.8. Cartographie Raman du signal de fond (BG), de la bande D et P.

Pour chaque cartographie Raman, nous avons généré un histogramme du rapport des intensités intégrées de la bande D et PEEK par rapport au signal de fond: A_D/A_{BG}, A_{PEEK}/A_{BG}. La Figure A.3.9 représente un exemple d'un tel histogramme.

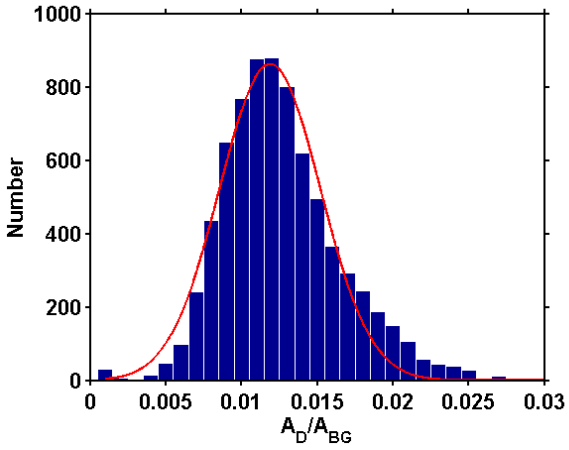

Figure A.3.9. Un exemple d'un histogramme de l'intensité relative de la bande D. La position du maximum de l'histogramme mesure la quantité de nanotubes de carbone et l'écart type donne une mesure de la dispersion de nanotubes de carbone dans le composite.

Nous avons ajusté les histogrammes avec une gaussienne (ligne rouge sur la Figure A.3.9) afin d'obtenir la position du maximum et l'élargissement (correspondant à une quantité proportionnelle à l'écart type). La position du maximum dans l'histogramme A_D/A_{BG} donne une mesure de la teneur en NTC et l'écart-type donne une mesure de la dispersion des tubes. Notre analyse suppose que l'erreur statistique propre aux tubes est suffisamment petite et peut être ignoré. Nous notons que l'écart type de la Figure A.3.9 ne doit pas être confondu avec le bruit d'un spectre Raman. L'écart-type de l'histogramme de la carte Raman est également appelé bruit de l'image. Nous notons que l'erreur statistique, ce qui limite l'analyse statistique, est plus faible que le bruit de l'image extraite.

De la littérature, on sait que la bande P ne change pas entre le PEEK amorphe et cristallin [155], mais on observe une augmentation en l'intensité (×1.5) à l'approche de la température de fusion (300°C). La bande P est donc censée être uniforme à travers la carte Raman. Toutefois, une certaine variation dans le rapport de la bande P sur le signal de fond a été trouvée que nous attribuons à être induite par la présence de nanotubes de carbone. La présence de nanotubes de carbone peut modifier le champ optique et la structure dans leur voisinage et, par conséquent, modifier l'intensité de la bande P. La position des maxima des histogrammes et les écarts types des intensités de la bande D par rapport au contenu en NTC sont présentés dans le Tableau A.3.2.

Echantillon	$\langle A_D/A_{BG}\rangle$ moyenne	$\langle A_D/A_{BG}\rangle$ élargissement /moyenne	$\langle A_P/A_{BG}\rangle$ moyenne	$\langle A_P/A_{BG}\rangle$ Élargissement /moyenne
Pur PEEK	0.0001	0.08	0.00093	0.26
PEEK 0.5% CNT	0.0064	0.32	0.00090	0.40
PEEK 1% CNT	0.0173	0.40	0.00212	0.30
PEEK 2% CNT	0.0494	0.63	0.00301	0.31

Tableau A.3.2. Position du maximum de l'histogramme du rapport de l'intensité Raman de la bande D et P et l'écart type en fonction du contenu en NTC.

On observe que l'intensité de la bande D augmente avec la quantité de nanotubes de carbone dans le composite comme prévu, mais en même temps l'histogramme de la bande D est plus large tandis que l'élargissement/moyenne reste constant démontrant clairement que la distribution des tubes est homothétique de la concentration des nanotubes de carbone. Avec un diamètre moyen de 10nm et 10 parois, chaque MWNT absorbe environ $1-(0.977)^{20} = 0.4$ [156] de la lumière incidente en utilisant comme l'hypothèse l'indice de réfraction de graphène (réduction de 2.3% après chaque paroi). Par conséquent, avec une couche de 1μm à 1% en poids NTC, la lumière transmise représente 40% de la lumière incidente. La profondeur de la sonde Raman en raison de trajet de la lumière dans le matériau (directe et retour) est inférieure à 1μm. Comme on n'utilise pas un dispositif confocal, la profondeur de la sonde avec notre expérience est donc limitée par l'absorption des nanotubes et est proportionnelle à la concentration. En conséquence, nous supposons que la valeur $<A_D>$ est constante alors que la valeur $<A_{BG}>$ est proportionnelle au volume de mesure (taille de spot multipliée par la profondeur de la sonde Raman). Ensuite, le rapport $<A_D/A_{BG}>$ est proportionnel à la concentration de NTC. L'élargissement/valeur moyenne est une mesure de la distribution normalisée par le volume (la valeur moyenne est proportionnelle au volume à une concentration donnée). Par conséquent, cette valeur est à peu près constante pour toutes les concentrations car l'opération de mélange est la même pour toutes les concentrations (même vitesse de la vis et les mêmes paramètres d'injection). Ces comportements sont attendus et confirmés par l'analyse Raman de la cartographie. Fait intéressant, le groupe de PEEK augmente avec la quantité de nanotubes de carbone dans le composite. Les NTC sont connus pour agir en tant que nano-antennes [157] et l'absorption du champ optique par les NTC est supérieure à celle de la matrice polymère. Cela augmente le champ local autour des NTC et, par conséquent le signal Raman de la matrice environnante est intensifié [158]. En outre, la surface de nanotubes de carbone peut conduire à un réarrangement local de molécules de polymère qui peuvent également augmenter le signal Raman du PEEK.

A partir des mesures de DSC, nous savons que la cristallinité moyenne ne change pas avec la présence de nanotubes de carbone, mais il est toujours possible que des NTC changent la nature de la cristallisation. Ceci se reflète dans la diminution de la ductilité à 15% de nanofibres de carbone (CNF) et avec 1% de nanotubes de carbone discutés ci-dessus. Ceci suggère que la présence de nanotubes de carbone modifie la flexibilité structurale de la matrice, effet dû à une structuration du PEEK en contact avec ou à proximité des nanotubes de carbone. Brosse *et al.* [159] rapporte une croissance épitaxiale de cristallites de polymère autour de NTC mais aucune grande modification de la cristallinité moyenne.

Nous avons effectué la même analyse sur les cartes Raman au centre et au bord du faisceau de composite. Surfaces de 200μm × 200μm, avec le pas de 10 microns pour l'échantillon du PEEK +1% en poids de NTC cartographiés ; des histogrammes pour la bande D et la bande de P ont été déduits. Les valeurs moyennes sont indiquées dans le Tableau A.3.3.

Echantillon	$<A_D/A_{BG}>$ moyenne	$<A_D/A_{BG}>$ élargissement /moyenne	$<A_P/A_{BG}>$ moyenne	$<A_P/A_{BG}>$ élargissement /moyenne
Centre	0.0173	0.25	0.0021	0.30
Bord	0.0142	0.26	0.0016	0.37

Tableau A.3.3. Résultats de l'évaluation statistique de rapport de l'intensité des bandes D et P de 1% NTC dans le centre et le bord de l'échantillon.

L'analyse statistique de l'intensité de la bande D montre que la concentration des nanotubes de carbone est plus élevée dans le centre. Cela est conforme avec la différence de dureté observée avec les mesures de nano-indentation. La microdureté a été trouvée être plus élevée au centre que sur le bord de la poutre en composite, ce qui est en corrélation avec la quantité de nanotubes de carbone présents dans les deux endroits différents ($<A_D/A_{BG}>$) (Tableau A.3.3).

Deux hypothèses peuvent être faites ici: les variations de contraintes de traction sont soit dues à une variation de la concentration de NTC ou un changement de l'agglomération des NTC. Dans les deux cas, cela peut conduire à une diminution du module et à un changement dans le rapport $<A_P/A_{BG}>$. Puisque le rapport de l'écart type et de la valeur moyenne de l'histogramme ne change pas beaucoup entre le bord et la partie centrale, nous pensons que cette variation est liée à la variation de concentration plutôt qu'à l'agglomération. La concentration plus élevée de NTC dans le centre du faisceau induit une dureté supérieure dans le centre de la poutre. Peut-être le procédé de moulage par injection et l'historique de la température des parties différentes de la poutre influence la dispersion locale des NTC résultent-ils des variations de la dureté.

3.3 Auto diffusion de NTC

Il a été récemment découvert que le recuit de nanotubes de carbone sur la surface d'un polymère thermoplastique forme une couche de surface composite avec une dispersion uniforme du tube à l'échelle de ~ 10 micromètres [163]. Ce phénomène est en relation avec le phénomène de percolation dynamique dans les nanocomposites en vrac qui a été observé par certains auteurs [67] [69] [68]. Dans cette partie, nous proposons une stratégie pour définir et caractériser les modifications du réseau de percolation à des échelles micrométriques et submicroniques. Pour obtenir une meilleure compréhension du processus d'auto-dispersion de NTC, nous utilisons la microscopie électronique à transmission et l'imagerie Raman multi-spectrale. Bien que la microscopie électronique à transmission révèle être limitée lors de l'observation des nanotubes de petit diamètre dans une matrice de polymère, la spectroscopie Raman peut être utilisée pour contrôler la dispersion du tube à différentes échelles ($>$ 1 micromètre).

Les solutions de DW (CIRIMAT) et MW (Arkema) NTC ont été déposées sur une feuille de PEEK. Les échantillons ont été recuits sous atmosphère d'argon au-dessus de la température de fusion du polymère thermoplastique (à 390°C) pendant 15 minutes (Figure A.3.10a-b).

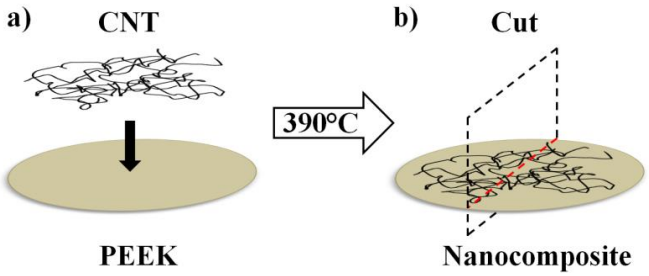

Figure A.3.10. Représentation schématique de la préparation des échantillons a) NTC agglomérés déposés sur une feuille PEEK et recuits sous atmosphère d'argon b) nanocomposite résultant.

Les mesures électriques (I(V), V_{max}=5V) ont été effectuées en fonction du nombre de gouttelettes de MW et DW NTC. Nous avons effectué des mesures avant et après recuit. La résistance diminue avec la quantité de nanotubes déposés (ligne noire sur les Figures 3.11a-b). Le recuit a l'effet que la résistance diminue d'un ou de deux ordres de grandeur (ligne rouge sur les Figures 3.11a-b).

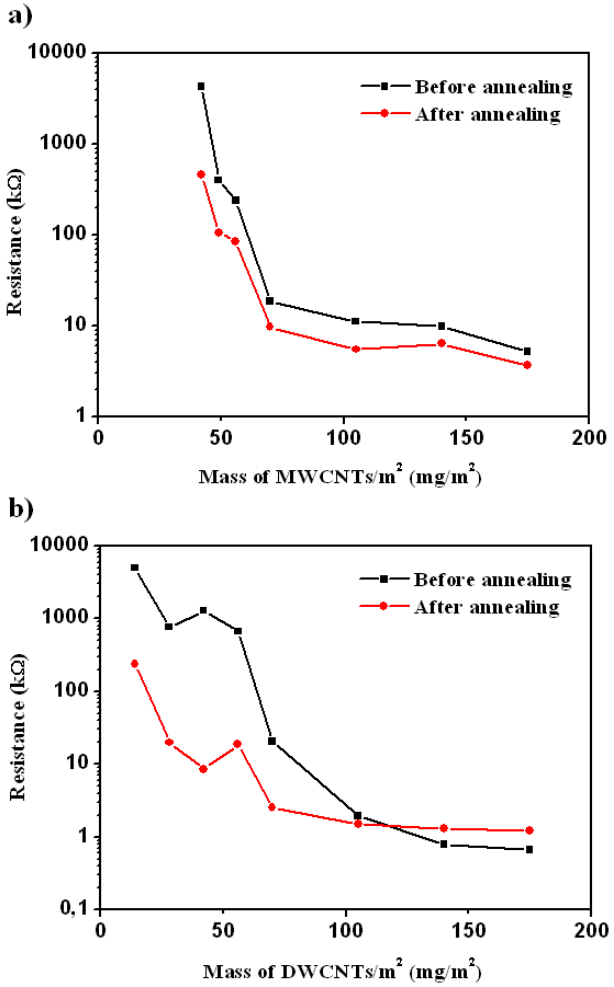

Figure A.3.11. L'effet de recuit sur la résistance pour a) MWNTs b) DWNTs

Cette diminution a pour origine deux effets. Le premier effet correspond à l'évaporation du solvant non conducteur à la température d'environ 200 °C, ce qui augmente la conductivité d'un facteur cinq environ. Le second effet est du à l'augmentation du nombre de Chemins de conduction. Cela signifie que le recuit induit la dispersion des agglomérats les plus grands et ainsi conduit à une augmentation de la quantité de petits agglomérats multipliant de ce fait le nombre de connexions et donc de chemins de conduction.

Pour DWNT à des charges élevées, on constate que le recuit ne provoque pas de diminution de la résistance des échantillons. Au contraire, elle augmente la résistance par rapport aux échantillons non recuits. Nous n'observons pas cet effet avec les MWNT de même charge en masse. On suppose que, lorsque la concentration de nanotubes de carbone sur la surface de PEEK est suffisamment grande, tous les tubes sont connectés et le recuit conduit uniquement à l'incorporation du polymère d'insolation entre les NTC. Nous n'observons pas cet effet avec les MWNTs probablement parce que le nombre de MWNTs à même charge en masse est inférieur [48], ainsi, il ne s'agit pas encore d'un réseau complet.

La Figure A.3.12 montre des images MEB des MWNTs à la surface du PEEK. Avant le recuit, on peut voir des tubes agglomérés. Après le recuit, on observe que le PEEK mouille les NTC et ils deviennent incorporés dans le polymère.

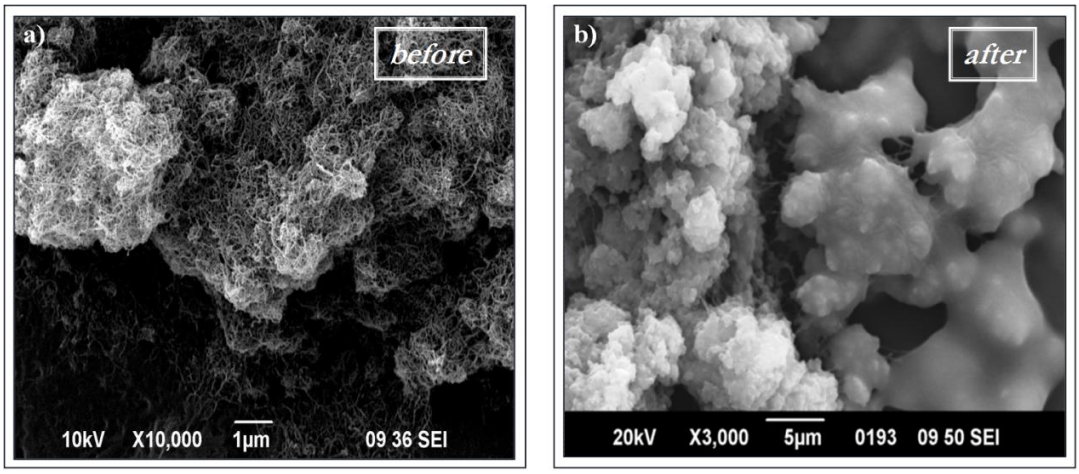

Figure A.3.12. Images MEB le film de PEEK avec des nanotubes de carbone
a) avant le recuit les MWNTs sont sur la surface du PEEK
b) après le recuit, le PEEK mouille les NTC. Dr. Victoria Tishkova

Le PEEK contient des groupes oxygène qui peuvent interagir avec la surface des nanotubes. Il est connu que l'oxygène moléculaire se lie aux SWNT avec une énergie d'adsorption de 0.25eV [164]. En outre, il est connu que l'interaction de l'oxygène avec la surface des nanotubes conduit à un dopage de trou et à la suppression de la luminescence des SWNT. Les cycles phénoliques du PEEK sont compatibles avec le réseau en nid d'abeilles de la surface du tube. Ces deux effets contribuent au fait que le PEEK mouille les NTC.

Afin d'évaluer la structure et la morphologie des matériaux composites formés à la surface après le recuit du PEEK, on utilise la spectroscopie Raman et le MET. La Figure A.3.13 représente une coupe transversale de MET à l'interface entre la couche de diffusion et la matrice PEEK.

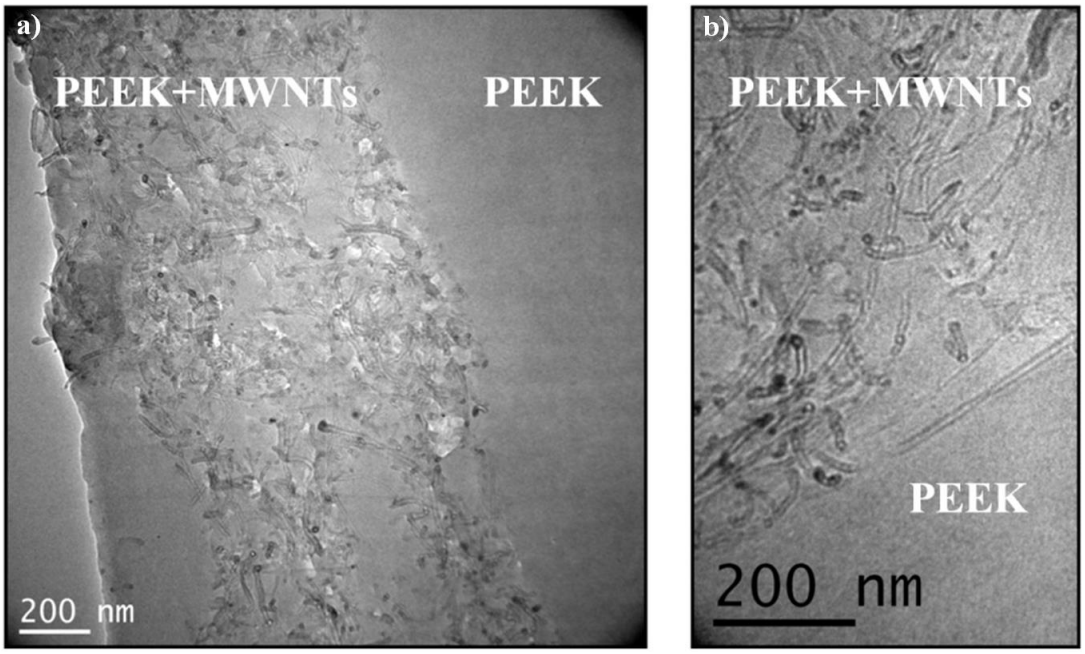

Figure A.3.13. Images MET de composite MWNT / PEEK à différentes résolutions. 15 minutes de recuit à 390°C pour des NTC agglomérés à la surface de PEEK. Les MWNT ont tendance à être orientées parallèlement à l'interface.

On observe la distribution uniforme des MWNTs et l'absence de grandes agglomérations. Une interface claire est formée entre le PEEK massif et le composite. Nous observons également que les NTC sont alignés le long de l'interface de la couche composite et du PEEK massif (Figure A.3.13b). Il est intéressant de voir qu'aucun changement de concentration n'est observé au voisinage de la couche de diffusion ou à des échelles plus grandes que la distance moyenne entre les tubes. Le fait que les tubes ont été agglomérés lorsque le solvant s'est évaporé sur la surface du film de PEEK indique que les tubes restent connectés dans un réseau après le recuit se comportant comme une seule phase. La mobilité des NTC dans la matrice de polymère devrait être beaucoup plus faible du fait de sa masse importante par rapport à la molécule de polymère. Étant donné que les molécules sont des chaînes de PEEK, elles ont tendance à s'aligner avec l'axe de la NTC favorisant la diffusion le long de l'axe du tube. La surface du tube constitue un trajet de diffusion préférentielle pour les molécules de la matrice.

Les MWNTs sont d'excellents absorbeurs infrarouges et optiques. La température plus élevée dans la proximité des tubes est en corrélation avec une plus grande diffusion de molécules de polymère à proximité de et sur les tubes. Cela signifie que l'action de diffusion est grande là où sont les agglomérats de tubes. Cela contribue à rendre la dispersion plus uniforme.

L'utilisation du MET permet d'estimer la longueur de la couche de diffusion de MWNT. Lors de l'utilisation de DWNT il est beaucoup plus difficile de distinguer les tubes par rapport aux fluctuations structurales du polymère (Figure A.3.14). Les DWNT ont un petit diamètre (2-3nm) et donnent souvent pas assez de contraste à faible concentration pour les rendre visibles par rapport à la matrice de polymère.

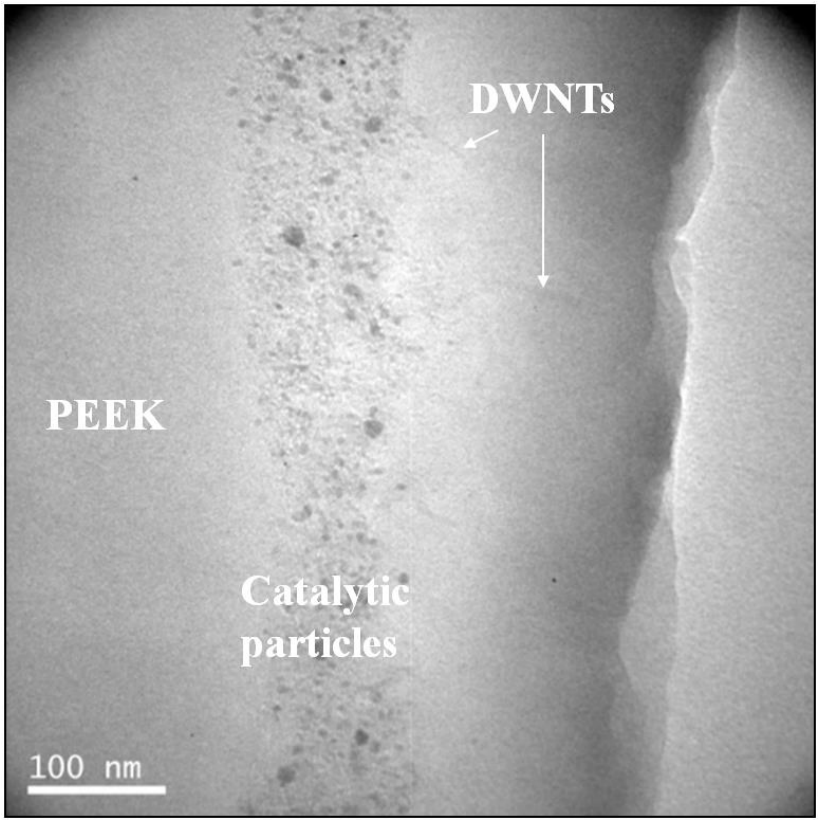

Figure A.3.14. Image MET de composite DWNT/PEEK.
15 minutes de recuit à 390°C pour les NTC agglomérés à la surface du PEEK.

On observe des particules sphériques qui sont soit des formes désordonnées de carbone ou d'autres particules de catalyseur lors de la croissance des nanotubes de carbone à double paroi. On peut voir que les particules catalytiques ne sont pas dispersées dans la couche composite. Cela montre indirectement l'importance de l'interaction du PEEK avec les tubes et la diffusion accrue sur la surface du tube. Nous pouvons également voir que certains tubes s'étendent dans la partie droite de l'image, mais le MET ne permet pas de tirer une conclusion au sujet de la couche de diffusion.

Pour estimer l'épaisseur et l'homogénéité de la couche de diffusion, nous utilisons la spectroscopie Raman comme une technique complémentaire au MET. Nous avons enregistré les spectres le long d'une ligne de 12µm, avec le pas de 0,02µm, à travers la couche de diffusion pour analyser son homogénéité. La Figure A.3.15a montre une image optique de la couche de diffusion des DWNT dans le PEEK. Sur la Figure A.3.15b, nous voyons les résultats de l'analyse de la ligne Raman. Les spectres Raman sont tracés dans le sens horizontal et l'intensité correspond à la couleur de l'image.

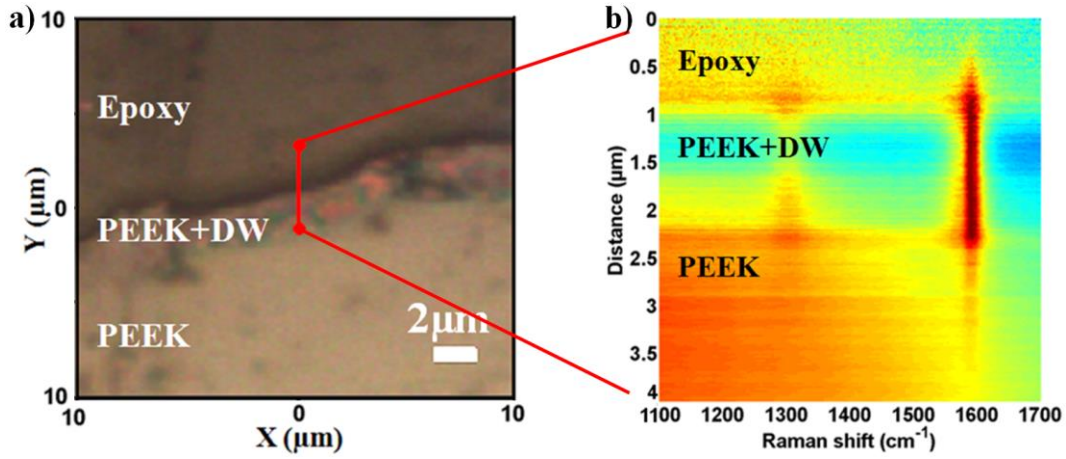

Figure A.3.15. a) Image optique de la couche de diffusion de composite DWNT@PEEK b) ligne Raman à travers la couche de diffusion: l'intensité et la largeur de la bande G sont uniformes à travers la couche. La bande D est plus intense à proximité des deux interfaces.

Les deux lignes vues dans la couche de diffusion correspondent aux bande Raman D et G. Pour les DWNTs, la bande G est plus intense et la bande D est moins uniforme. A partir de l'intensité uniforme de la bande G à travers la couche, nous concluons que les DWNT sont dispersés de façon homogène à l'échelle de la taille du spot d'un objectif optique et nous en déduisons l'épaisseur de la couche de diffusion (1-1,5µm). L'intensité de la bande D est moins forte dans le milieu de la couche. Il n'est pas facile d'expliquer pourquoi il y a plus de défauts près des deux interfaces. Cet aspect doit être approfondi.

Conclusion

En utilisant la spectroscopie Raman, j'ai pu obtenir des informations sur l'interaction de DWNTs avec les molécules d'acide sulfurique environnantes. Le tube interne est une sonde de contrainte tandis que le tube extérieur est en contact avec l'environnement, c'est-à-dire est sensible à la déformation et au transfert de charge. Le DWNT peut être utilisé comme un capteur moléculaire, en particulier, des nanocomposites à étudier. Les composites DWNT@PEEK ont été étudiés pour contrôler la dispersion des tubes dans le polymère. En utilisant la cartographie micro-Raman, des informations de l'échelle millimétrique à micrométrique ont été obtenues, informations qui ne peuvent pas être révélées par la microscopie optique. Jusqu'à présent, la spectroscopie Raman, lorsqu'elle était appliquée à des nanocomposites en tant que tels, n'était pas considéré comme assez informative. En effet, un spectre Raman simple n'est pas suffisant pour caractériser un matériau composite. Mais grâce à l'examen d'une cartographie Raman précise, j'ai développé une analyse statistique qui ouvre de nouvelles perspectives dans la caractérisation des nanocomposites. L'analyse statistique nécessite des milliers de spectres enregistrés à différentes échelles. Chaque spectre doit être ajusté de manière appropriée en sélectionnant le bon ensemble de paramètres. Cela signifie que les résultats ne dépendent pas des valeurs d'initialisation de l'ajustement. Dans le même temps, le nombre de paramètres doit être maintenu aussi petit que possible, ce qui nécessite des tests préalables et le développement de

routines d'ajustement. Pour interpréter correctement les données précédentes, les résultats théoriques et expérimentaux du graphène et des nanotubes doivent être considérés avec précaution. En combinant les résultats Raman avec MET et les mesures de transport électrique ou de nano-indentation ainsi que la diffusion élastique de neutrons, on peut aller plus loin dans l'interprétation des données. Dans ce travail, j'ai pu étudier deux nanocomposites spécifiques: NTC dans les matrice polymère et métallique.

Pour les DWNT dans le cuivre, le choix de la bande Raman pour caractériser les nanotubes dans un composite n'a pas été trivial. Les deux bandes D et G peuvent être analysées pour obtenir des informations sur l'échantillon. La bande G a été analysée à travers trois contributions G_o^+, G_i^+ et D'. Lorsque tous les paramètres des bandes (fréquence, largeur de ligne, intensité) sont laissés libres, on constate que l'histogramme de la fréquence G_o^+ de la bande est étroit indiquant l'absence de décalage spectral. Cela signifie qu'il n'y a pas de transfert de charge. Cette analyse statistique a permis de fixer les fréquences et les largeurs des bandes G^+ des tubes interne et externe et d'analyser l'augmentation de bande D' au travers de la cartographie Raman. Le rapport des intensités de la bande D' sur D en association avec le rapport des intensités de la D sur la bande G a été utilisée pour obtenir des informations sur l'état des tubes. Il a enfin pu être conclu que l'espacement intercouche entre les tubes intérieur et extérieur est réduit après les essais d'usure. Il a été montré que les tubes ne sont pas transformés en carbone amorphe, bien que l'usure intense ait augmenté le nombre de défauts.

Dans le cas d'un composite polymère, la bande G est habituellement utilisée pour indiquer la présence de nanotubes de carbone. Mais dans ce travail, je trouve qu'à faible concentration de NTC la bande G est masquée par la diffusion inélastique du polymère PEEK. En revanche, la fréquence de la bande D est située dans un endroit dans lequel aucune autre vibration du polymère n'est présente. En outre, la fréquence peut être réglée en modifiant l'énergie d'excitation. J'ai choisi l'excitation dans le proche infrarouge de la bande D pour réduire la surchauffe de l'échantillon. La valeur moyenne et l'écart-type de l'histogramme du rapport de la bande D sur le fond fournissent des informations sur la concentration et l'homogénéité de la dispersion de NTC. Une étape importante dans l'analyse était d'utiliser le signal de fond comme un indicateur de la matrice qui peut être utilisée dans l'analyse statistique.

Les expériences de recuit sur la surface de PEEK montrent que les tubes auto-dispersent dans le polymère PEEK. Avec le MET, nous observons que le polymère PEEK recouvre les tubes à la surface et la couche de diffusion de NTC a une interface forte avec le polymère. Ceci est également vu dans les cartographies Raman à travers la couche de composite. L'auto-dispersion des tubes a été vérifiée sur les différents types de nanotubes de carbone. Nous pensons que l'absorption d'infrarouge par des NTC conduit à une meilleure diffusion de PEEK dans le voisinage des tubes en améliorant la diffusion du polymère dans les agglomérats de NTC. Ce mécanisme d'auto-diffusion fournit aussi une explication possible du phénomène de percolation dynamique. L'auto-dispersion des NTC lors d'un recuit est une méthode prometteuse pour rendre électriquement conductrices des fines couches de surface composites et ouvre une perspective intéressante pour réparer les surfaces par chauffage.

Bibliography

1. Gibson Ronald F. Principles of composite material mechanics. CRC Press, 2011

2. Cairns Douglas S. "ME 463 Design, Analysis, and Manufacturing Project Fall Semester, 2009."http://www.coe.montana.edu/me/faculty/cairns/Composites/MSUComposites2009.pdf

3. Malaval Philippe, and Christophe Bénaroya. Aerospace marketing management. Springer Internat. Publ., 2013

4. Jar P. Y., H. H. Kausch, W. J. Cantwell, P. Davies, and H. Richard. "The effect of annealing on the short and long term behavior of PEEK." Polymer bulletin 24, no. 6 (1990): 657-664

5. Cebe Peggy, and Su-Don Hong. "Crystallization behaviour of poly (ether-ether-ketone)." Polymer 27.8 (1986): 1183-1192

6. Verma Ravi, Herve Marand, and Benjamin Hsiao. "Morphological changes during secondary crystallization and subsequent melting in poly (ether ether ketone) as studied by real time small angle X-ray scattering." Macromolecules 29.24 (1996): 7767-7775

7. Margolis ed. Engineering thermoplastics: properties and applications. Vol. 8. Taylor & Francis, 1985

8. Matthews Frank L., and Rees D. Rawlings. Composite materials: engineering and science. Elsevier, 1999

9. Rosso Mario. "Ceramic and metal matrix composites: Routes and properties." Journal of Materials Processing Technology 175, no. 1 (2006): 364-375

10. http://www.copper.org/

11. Bethune D.S.b, Kiang C.H., De Vries M.S., Gorman G., Savoy R., Vazquez J., Beyers R "Cobalt-catalyzed growth of carbon nanotubes with single-atomic-layerwalls." Nature, 363 (6430) (1993), pp. 605–607

12. Iijima Sumio. "Helical microtubules of graphitic carbon." nature 354.6348 (1991): 56-58

13. Coleman Jonathan N., Umar Khan, Werner J. Blau, and Yurii K. Gun'ko. "Small but strong: a review of the mechanical properties of carbon nanotube–polymer composites." Carbon 44, no. 9 (2006): 1624-1652

14. Dresselhaus Mildred S., G. Dresselhaus, R. Saito, and A. Jorio. "Raman spectroscopy of carbon nanotubes." Physics Reports 409, no. 2 (2005): 47-99

15. Saito Riichiro, Gene Dresselhaus, and Mildred S. Dresselhaus. Physical properties of carbon nanotubes. Vol. 4. London: Imperial college press, 1998

16. Omar M. Ali. Elementary solid state physics: principles and applications. Vol. 157. Reading, MA, USA:: Addison-Wesley, 1975

17. Samsonidze Ge G., A. R. Saito, D. A. Jorio, E. Pimenta, Filho Souza, E. AG, F. A. Grüneis, D. G. Dresselhaus, and M. S. Dresselhausa. "The concept of cutting lines in carbon nanotube science." Journal of nanoscience and nanotechnology 3, no. 6 (2003): 431-458

18. Kataura H., Y. Kumazawa, Y. Maniwa, I. Umezu, S. Suzuki, Yo Ohtsuka, and Y. Achiba. "Optical properties of single-wall carbon nanotubes." Synthetic Metals 103, no. 1 (1999): 2555-2558

19. Fantini C., A. Jorio, M. Souza, M. S. Strano, M. S. Dresselhaus, and M. A. Pimenta. "Optical transition energies for carbon nanotubes from resonant Raman spectroscopy: Environment and temperature effects." Physical review letters 93, no. 14 (2004): 147406

20. Telg H., J. Maultzsch, S. Reich, F. Hennrich, and C. Thomsen. "Chirality distribution and transition energies of carbon nanotubes." Physical review letters 93, no. 17 (2004): 177401

21. Araujo Paulo T., Stephen K. Doorn, Svetlana Kilina, Sergei Tretiak, Erik Einarsson, Shigeo Maruyama, Helio Chacham, Marcos A. Pimenta, and Ado Jorio. "Third and fourth optical transitions in semiconducting carbon nanotubes." Physical review letters 98, no. 6 (2007): 067401

22. Tsyboulski Dmitri A., John-David R. Rocha, Sergei M. Bachilo, Laurent Cognet, and R. Bruce Weisman. "Structure-dependent fluorescence efficiencies of individual single-walled carbon nanotubes." Nano letters 7, no. 10 (2007): 3080-3085

23. Maultzsch J., S. Reich, C. Thomsen, H. Requardt, and P. Ordejón. "Phonon dispersion in graphite." Physical review letters 92, no. 7 (2004): 075501

24. Lazzeri Michele, and Francesco Mauri. "Coupled dynamics of electrons and phonons in metallic nanotubes: Current saturation from hot-phonon generation." Physical Review B 73.16 (2006): 165419

25. Ma Peng-Cheng, Naveed A. Siddiqui, Gad Marom, and Jang-Kyo Kim. "Dispersion and functionalization of carbon nanotubes for polymer-based nanocomposites: a review." Composites Part A: Applied Science and Manufacturing 41, no. 10 (2010): 1345-1367

26. Yu Min-Feng, Oleg Lourie, Mark J. Dyer, Katerina Moloni, Thomas F. Kelly, and Rodney S. Ruoff. "Strength and breaking mechanism of multiwalled carbon nanotubes under tensile load." Science 287, no. 5453 (2000): 637-640

27. Yu Min-Feng, Bradley S. Files, Sivaram Arepalli, and Rodney S. Ruoff. "Tensile loading of ropes of single wall carbon nanotubes and their mechanical properties." Physical review letters 84, no. 24 (2000): 5552

28. Xie Sishen, Wenzhi Li, Zhengwei Pan, Baohe Chang, and Lianfeng Sun. "Mechanical and physical properties on carbon nanotube." Journal of Physics and Chemistry of solids 61, no. 7 (2000): 1153-1158

29. Xu F., L. X. Sun, J. Zhang, Y. N. Qi, L. N. Yang, H. Y. Ru, C. Y. Wang *et al.* "Thermal stability of carbon nanotubes." Journal of thermal analysis and calorimetry 102, no. 2 (2010): 785-791

30. Kim Y. A., H. Muramatsu, T. Hayashi, M. Endo, M. Terrones, and M. S. Dresselhaus. "Thermal stability and structural changes of double-walled carbon nanotubes by heat treatment." Chemical Physics Letters 398, no. 1 (2004): 87-92

31. Berber Savas, Young-Kyun Kwon, and David Tomanek. "Unusually high thermal conductivity of carbon nanotubes." Physical review letters 84.20 (2000): 4613

32. Kim P., Li Shi, A. Majumdar, and P. L. McEuen. "Thermal transport measurements of individual multiwalled nanotubes." Physical review letters 87, no. 21 (2001): 215502

33. Van Wees B. J., H. Van Houten, C. W. J. Beenakker, J. Gr Williamson, L. P. Kouwenhoven, D. Van der Marel, and C. T. Foxon. "Quantized conductance of point contacts in a two-dimensional electron gas." Physical Review Letters 60, no. 9 (1988): 848

34. Tserkovnyak Yaroslav, and Bertrand I. Halperin. "Magnetoconductance oscillations in quasiballistic multimode nanowires." Physical Review B 74, no. 24 (2006): 245327

35. Frank Stefan, Philippe Poncharal, Z. L. Wang, and Walt A. de Heer. "Carbon nanotube quantum resistors." Science 280, no. 5370 (1998): 1744-1746

36. Wei B. Q., R. Vajtai, and P. M. Ajayan. "Reliability and current carrying capacity of carbon nanotubes." Applied Physics Letters 79.8 (2001): 1172-1174

37. Vinod K., RG Abhilash Kumar, and U. Syamaprasad. "Prospects for MgB2 superconductors for magnet application." Superconductor Science and Technology 20.1 (2007): R1

38. Dürkop T., S. A. Getty, Enrique Cobas, and M. S. Fuhrer. "Extraordinary mobility in semiconducting carbon nanotubes." Nano letters 4, no. 1 (2004): 35-39

39. Tang Z. K., Lingyun Zhang, N. Wang, X. X. Zhang, G. H. Wen, G. D. Li, J. N. Wang, C. T. Chan, and Ping Sheng. "Superconductivity in 4 angstrom single-walled carbon nanotubes." Science 292, no. 5526 (2001): 2462-2465

40. Kim Kyung Tae, Seung Il Cha, Seong Hyeon Hong, and Soon Hyung Hong. "Microstructures and tensile behavior of carbon nanotube reinforced Cu matrix nanocomposites." Materials Science and Engineering: A 430, no. 1 (2006): 27-33

41. Bakshi S. R., D. Lahiri, and Arvind Agarwal. "Carbon nanotube reinforced metal matrix composites-a review." International Materials Reviews 55, no. 1 (2010): 41-64

42. Dong S. R., J. P. Tu, and X. B. Zhang. "An investigation of the sliding wear behavior of Cu-matrix composite reinforced by carbon nanotubes." Materials Science and Engineering: A 313, no. 1 (2001): 83-87

43. Rajkumar K., and S. Aravindan. "Tribological studies on microwave sintered copper–carbon nanotube composites." Wear 270.9 (2011): 613-621

44. Lin C. B., Zue-Chin Chang, Y. H. Tung, and Yuan-Yuan Ko. "Manufacturing and tribological properties of copper matrix/carbon nanotubes composites." Wear 270, no. 5 (2011): 382-394

45. Kim Kyung Tae, Seung Il Cha, and Soon Hyung Hong. "Hardness and wear resistance of carbon nanotube reinforced Cu matrix nanocomposites." Materials Science and Engineering: A 449 (2007): 46-50

46. Chen W. X., J. P. Tu, L. Y. Wang, H. Y. Gan, Z. D. Xu, and X. B. Zhang. "Tribological application of carbon nanotubes in a metal-based composite coating and composites." Carbon 41, no. 2 (2003): 215-222

47. Guiderdoni Ch, Claude Estournès, Alain Peigney, Alicia Weibel, Viviane Turq, and Ch Laurent. "The preparation of double-walled carbon nanotube/Cu composites by spark plasma sintering, and their hardness and friction properties." Carbon 49, no. 13 (2011): 4535-4543

48. Laurent Ch, Emmanuel Flahaut, and Alain Peigney. "The weight and density of carbon nanotubes versus the number of walls and diameter." Carbon 48, no. 10 (2010): 2994-2996

49. Bangarusampath D. S., Holger Ruckdäschel, Volker Altstädt, Jan KW Sandler, Didier Garray, and Milo SP Shaffer. "Rheology and properties of melt-processed poly (ether ether ketone)/multi-wall carbon nanotube composites." Polymer 50, no. 24 (2009): 5803-58

50. Pham J. Q., C. A. Mitchell, J. L. Bahr, J. M. Tour, R. Krishanamoorti, and Peter F. Green. "Glass transition of polymer/single-walled carbon nanotube composite films." Journal of Polymer Science Part B: Polymer Physics 41, no. 24 (2003): 3339-3345

51. Barraza Harry J., Francisco Pompeo, Edgar A. O'Rea, and Daniel E. Resasco. "SWNT-filled thermoplastic and elastomeric composites prepared by miniemulsion polymerization." Nano letters 2, no. 8 (2002): 797-802

52. Mittal Vikas, ed. Polymer nanotube nanocomposites: synthesis, properties, and applications. Vol. 11. John Wiley & Sons, 2010

53. Díez-Pascual Ana M., Mohammed Naffakh, Marián A. Gómez, Carlos Marco, Gary Ellis, M. Teresa Martínez, Alejandro Ansón, José M. González-Domínguez, Yadienka Martínez-Rubi, and Benoit Simard., "Development and characterization of PEEK/carbon nanotube composites." Carbon 47, no. 13 (2009): 3079-3090

54. Wang Hongsong, Guibin Wang, Wenlei Li, Qitong Wang, Wei Wei, Zhenhua Jiang, and Shuling Zhang., "A material with high electromagnetic radiation shielding effectiveness fabricated using multi-walled carbon nanotubes wrapped with poly (ether

sulfone) in a poly (ether ether ketone) matrix." Journal of Materials Chemistry 22, no. 39 (2012): 21232-21237

55. Li Lingyu, Christopher Y. Li, Chaoying Ni, Lixia Rong, and Benjamin Hsiao. "Structure and crystallization behavior of Nylon 66/multi-walled carbon nanotube nanocomposites at low carbon nanotube contents." Polymer 48, no. 12 (2007): 3452-3460

56. Rong Changru, Gang Ma, Shuling Zhang, Li Song, Zheng Chen, Guibin Wang, and P. M. Ajayan. "Effect of carbon nanotubes on the mechanical properties and crystallization behavior of poly (ether ether ketone)." Composites Science and Technology 70, no. 2 (2010): 380-386

57. Kumar S., T. Rath, R. N. Mahaling, C. S. Reddy, C. K. Das, K. N. Pandey, R. B. Srivastava, and S. B. Yadaw., "Study on mechanical, morphological and electrical properties of carbon nanofiber/polyetherimide composites." Materials Science and Engineering: B 141, no. 1 (2007): 61-70

58. Sandler Jan, Philipp Werner, Milo SP Shaffer, Vitaly Demchuk, Volker Altstädt, and Alan H. Windle. "Carbon-nanofibre-reinforced poly (ether ether ketone) composites." Composites Part A: Applied Science and Manufacturing 33, no. 8 (2002): 1033-1039

59. Moniruzzaman Mohammad, and Karen I. Winey. "Polymer nanocomposites containing carbon nanotubes." Macromolecules 39.16 (2006): 5194-5205

60. Deng Fei, Toshio Ogasawara, and Nobuo Takeda. "Tensile properties at different temperature and observation of micro deformation of carbon nanotubes–poly (ether ether ketone) composites." Composites Science and Technology 67, no. 14 (2007): 2959-2964

61. Li Ning, Yi Huang, Feng Du, Xiaobo He, Xiao Lin, Hongjun Gao, Yanfeng Ma, Feifei Li, Yongsheng Chen, and Peter C. Eklund. "Electromagnetic interference (EMI) shielding of single-walled carbon nanotube epoxy composites." Nano letters 6, no. 6 (2006): 1141

62. Markarian Jennifer. "Increased demands in electronics drive additive developments in conductivity." Plastics, Additives and Compounding 7.1 (2005): 26-30

63. Broadbent Simon R., and John M. Hammersley. "Percolation processes." In Mathematical Proceedings of the Cambridge Philosophical Society, vol. 53, no. 03, pp. 629-641. Cambridge University Press, 1957

64. Stauffer Dietrich, and Amnon Aharony. Introduction to percolation theory. Taylor and Francis, 1991

65. Sahini M., and M. Sahimi. Applications of percolation theory. CRC Press, 1994

66. Vionnet-Menot Sonia, Claudio Grimaldi, Thomas Maeder, Sigfrid Strässler, and Peter Ryser. "Tunneling-percolation origin of nonuniversality: theory and experiments." Physical Review B 71, no. 6 (2005): 064201

67. Combessis Anthony, Lorrene Bayon, and Lionel Flandin. "Effect of filler auto-assembly on percolation transition in carbon nanotube/polymer composites." Applied Physics Letters 102.1 (2013): 011907

68. Zhang Rui, Alice Dowden, Hua Deng, Mark Baxendale, and Ton Peijs. "Conductive network formation in the melt of carbon nanotube/thermoplastic polyurethane composite." Composites Science and Technology 69, no. 10 (2009): 1499-1504

69. Martin C. A., J. K. W. Sandler, M. S. P. Shaffer, M-K. Schwarz, W. Bauhofer, K. Schulte, and A. H. Windle. "Formation of percolating networks in multi-wall carbon-nanotube–epoxy composites." Composites Science and Technology 64, no. 15 (2004): 2309-2316

70. Mohiuddin M., and S. V. Hoa. "Temperature dependent electrical conductivity of CNT–PEEK composites." Composites Science and Technology 72.1 (2011): 21-27

71. Koning Cor, Marie-Claire Hermant, and Nadia Grossiord, eds. Polymer Carbon Nanotube Composites: The Polymer Latex Concept. CRC Press, 2012

72. Bauhofer Wolfgang, and Josef Z. Kovacs. "A review and analysis of electrical percolation in carbon nanotube polymer composites." Composites Science and Technology 69.10 (2009): 1486-1498

73. Kovacs Josef Z., Bala S. Velagala, Karl Schulte, and Wolfgang Bauhofer. "Two percolation thresholds in carbon nanotube epoxy composites." Composites Science and Technology 67, no. 5 (2007): 922-928

74. Sandler J. K. W., J. E. Kirk, I. A. Kinloch, M. S. P. Shaffer, and A. H. Windle. "Ultra-low electrical percolation threshold in carbon-nanotube-epoxy composites." Polymer 44, no. 19 (2003): 5893-5899

75. Kilbride BE ea, J. N. Coleman, J. Fraysse, P. Fournet, M. Cadek, A. Drury, S. Hutzler, S. Roth, and W. J. Blau., "Experimental observation of scaling laws for alternating current and direct current conductivity in polymer-carbon nanotube composite thin films." Journal of Applied Physics 92, no. 7 (2002): 4024-4030

76. Díez-Pascual Ana M., Mohammed Naffakh, José M. González-Domínguez, Alejandro Ansón, Yadienka Martínez-Rubi, M. Teresa Martínez, Benoit Simard, and Marián A. Gómez., "High performance PEEK/carbon nanotube composites compatibilized with polysulfones-II. Mechanical and electrical properties." Carbon 48, no. 12 (2010): 3500-3511

77. Tishkova Victoria, Pierre-Ivan Raynal, Pascal Puech, Antoine Lonjon, Marion Le Fournier, Philippe Demont, Emmanuel Flahaut, and Wolfgang Bacsa. "Electrical conductivity and Raman imaging of double wall carbon nanotubes in a polymer matrix." Composites Science and Technology 71, no. 10 (2011): 1326-1330

78. Díez-Pascual Ana M., Mohammed Naffakh, Carlos Marco, and Gary Ellis. "Mechanical and electrical properties of carbon nanotube/poly (phenylene sulphide) composites incorporating polyetherimide and inorganic fullerene-like nanoparticles." Composites Part A: Applied Science and Manufacturing 43, no. 4 (2012): 603-612

79. Mamunya Ye P., V. V. Davydenko, P. Pissis, and E. V. Lebedev. "Electrical and thermal conductivity of polymers filled with metal powders." European polymer journal 38, no. 9 (2002): 1887-1897

80. Díez-Pascual Ana M., Behnam Ashrafi, Mohammed Naffakh, José M. González-Domínguez, Andrew Johnston, Benoit Simard, M. Teresa Martinez, and Marián A. Gómez-Fatou, "Influence of carbon nanotubes on the thermal, electrical and mechanical properties of poly (ether ether ketone)/glass fiber laminates." Carbon 49, no. 8 (2011): 2817-2833

81. Girifalco L. A., Miroslav Hodak, and Roland S. Lee. "Carbon nanotubes, buckyballs, ropes, and a universal graphitic potential." Physical Review B 62.19 (2000): 13104

82. Coleman Jonathan N., Umar Khan, and Yurii K. Gun'ko. "Mechanical reinforcement of polymers using carbon nanotubes." Advanced Materials 18.6 (2006): 689-706

83. O'connell Michael J., Sergei M. Bachilo, Chad B. Huffman, Valerie C. Moore, Michael S. Strano, Erik H. Haroz, Kristy L. Rialon *et al.* "Band gap fluorescence from individual single-walled carbon nanotubes." Science 297, no. 5581 (2002): 593-596

84. Banerjee Sarbajit, Tirandai Hemraj-Benny, and Stanislaus S. Wong. "Covalent surface chemistry of single-walled carbon nanotubes." Advanced Materials 17.1 (2005): 17-29

85. Niyogi S., M. A. Hamon, H. Hu, B. Zhao, P. Bhowmik, R. Sen, M. E. Itkis, and R. C. Haddon. "Chemistry of single-walled carbon nanotubes." Accounts of Chemical Research 35, no. 12 (2002): 1105-1113

86. Ramesh Sivarajan, Lars M. Ericson, Virginia A. Davis, Rajesh K. Saini, Carter Kittrell, Matteo Pasquali, W. E. Billups, W. Wade Adams, Robert H. Hauge, and Richard E. Smalley., "Dissolution of pristine single walled carbon nanotubes in superacids by direct protonation." The Journal of Physical Chemistry B 108, no. 26 (2004): 8794-8798

87. Bergin Shane D., Valeria Nicolosi, Philip V. Streich, Silvia Giordani, Zhenyu Sun, Alan H. Windle, Peter Ryan *et al.* "Towards Solutions of Single-Walled Carbon Nanotubes in Common Solvents." Advanced Materials 20, no. 10 (2008): 1876-1881

88. Benedict Lorin X., Nasreen G. Chopra, Marvin L. Cohen, A. Zettl, Steven G. Louie, and Vincent H. Crespi. "Microscopic determination of the interlayer binding energy in graphite." Chemical Physics Letters 286, no. 5 (1998): 490-496

89. Girifalco L. A., Miroslav Hodak, and Roland S. Lee. "Carbon nanotubes, buckyballs, ropes, and a universal graphitic potential." Physical Review B 62, no. 19 (2000): 13104

90. Hodak Miroslav, and L. A. Girifalco. "Fullerenes inside carbon nanotubes and multi-walled carbon nanotubes: optimum and maximum sizes." Chemical physics letters 350, no. 5 (2001): 405-411

91. Zacharia Renju, Hendrik Ulbricht, and Tobias Hertel. "Interlayer cohesive energy of graphite from thermal desorption of polyaromatic hydrocarbons." Physical Review B 69, no. 15 (2004): 155406

92. Vaisman Linda, H. Daniel Wagner, and Gad Marom. "The role of surfactants in dispersion of carbon nanotubes." Advances in colloid and interface science 128 (2006): 37-46

93. Luo Z. P., and J. H. Koo. "Quantifying the dispersion of mixture microstructures." Journal of microscopy 225.2 (2007): 118-125

94. Pegel S., P. Pötschke, T. Villmow, D. Stoyan, and G. Heinrich. "Spatial statistics of carbon nanotube polymer composites." Polymer 50, no. 9 (2009): 2123-2132

95. Hayes William, and Rodney Loudon. Scattering of light by crystals. Courier Dover Publications, 2012

96. Maultzsch J., H. Telg, S. Reich, and C. Thomsen. "Radial breathing mode of single-walled carbon nanotubes: Optical transition energies and chiral-index assignment." Physical Review B 72, no. 20 (2005): 205438

97. Milnera M., J. Kürti, Martin Hulman, and Hans Kuzmany. "Periodic resonance excitation and intertube interaction from quasicontinuous distributed helicities in single-wall carbon nanotubes." Physical review letters 84, no. 6 (2000): 1324

98. Jorio A., R. Saito, J. H. Hafner, C. M. Lieber, M. Hunter, T. McClure, G. Dresselhaus, and M. S. Dresselhaus. "Structural (n, m) determination of isolated single-wall carbon nanotubes by resonant Raman scattering.", Physical Review Letters 86, no. 6 (2001): 1118

99. Kürti Jeno, Viktor Zólyomi, Miklos Kertesz, and Guangyu Sun. "The geometry and the radial breathing mode of carbon nanotubes: beyond the ideal behaviour." New Journal of Physics 5, no. 1 (2003): 125

100. Puech P. Dunstan D.J., "Thickness of graphene and single-wall carbon nanotubes : mechanical effects" 2014 unpublished.

101. Krupke Ralph, Frank Hennrich, Hilbert V. Löhneysen, and Manfred M. Kappes. "Separation of metallic from semiconducting single-walled carbon nanotubes." Science 301, no. 5631 (2003): 344-347

102. Dresselhaus Mildred S., Ado Jorio, Mario Hofmann, Gene Dresselhaus, and Riichiro Saito. "Perspectives on carbon nanotubes and graphene Raman spectroscopy." Nano letters 10, no. 3 (2010): 751-758

103. Levshov Dmitry, T. X. Than, R. Arenal, V. N. Popov, R. Parret, M. Paillet, V. Jourdain *et al.* "Experimental evidence of a mechanical coupling between layers in an individual double-walled carbon nanotube." Nano letters 11, no. 11 (2011): 4800-4804

104. Machón M., S. Reich, H. Telg, J. Maultzsch, P. Ordejón, and C. Thomsen. "Strength of radial breathing mode in single-walled carbon nanotubes." Physical Review B 71, no. 3 (2005): 035416

105. Piscanec Stefano, Michele Lazzeri, John Robertson, Andrea C. Ferrari, and Francesco Mauri. "Optical phonons in carbon nanotubes: Kohn anomalies, Peierls distortions, and dynamic effects." Physical Review B 75, no. 3 (2007): 035427

106. Prudkovskiy Vladimir, Mourad Berd, Ekaterina Pavlenko, Konstantin Katin, Mikhail Maslov, Pascal Puech, Marc Monthioux, Walter Escoffier, Michel Goiran, and Bertrand Raquet., "Electronic coupling in fullerene-doped semiconducting carbon nanotubes probed by Raman spectroscopy and electronic transport." Carbon 57 (2013): 498-506

107. Puech Pascal, Hannes Hubel, David J. Dunstan, R. R. Bacsa, Christophe Laurent, and W. S. Bacsa. "Discontinuous tangential stress in double wall carbon nanotubes." Physical review letters 93, no. 9 (2004): 095506

108. Jorio A., R. Saito, G. Dresselhaus, and M. S. Dresselhaus. "Determination of nanotubes properties by Raman spectroscopy.", Philosophical Transactions of the Royal Society of London. Series A: Mathematical, Physical and Engineering Sciences 362, no. 1824 (2004): 2311-2336

109. Chen Gugang, S. Bandow, E. R. Margine, C. Nisoli, A. N. Kolmogorov, Vincent H. Crespi, R. Gupta, G. U. Sumanasekera, S. Iijima, and P. C. Eklund. "Chemically doped double-walled carbon nanotubes: cylindrical molecular capacitors.", Physical review letters 90, no. 25 (2003): 257403

110. Bushmaker Adam W., Vikram V. Deshpande, Marc W. Bockrath, and Stephen B. Cronin. "Direct observation of mode selective electron-phonon coupling in suspended carbon nanotubes." Nano letters 7, no. 12 (2007): 3618-3622

111. Maultzsch J., S. Reich, and C. Thomsen. "Double-resonant Raman scattering in graphite: Interference effects, selection rules, and phonon dispersion." Physical Review B 70, no. 15 (2004): 155403

112. Thomsen C., and S. Reich. "Double resonant Raman scattering in graphite." Physical Review Letters 85, no. 24 (2000): 5214

113. Tuinstra F., and J. L_ Koenig. "Raman spectrum of graphite." The Journal of Chemical Physics 53, no. 3 (1970): 1126-1130

114. Beams Ryan, Luiz Gustavo Cançado, and Lukas Novotny. "Low temperature Raman study of the electron coherence length near graphene edges." Nano letters 11, no. 3 (2011): 1177-1181

115. Cançado L. G., A. Jorio, and M. A. Pimenta. "Measuring the absolute Raman cross section of nanographites as a function of laser energy and crystallite size." Physical Review B 76, no. 6 (2007): 064304

116. Mallet-Ladeira Philippe, Pascal Puech, Constance Toulouse, Maximilien Cazayous, Nicolas Ratel-Ramond, Patrick Weisbecker, Gérard L. Vignoles, Marc Monthioux, "A Raman study to obtain crystallite size of carbon materials: a better alternative to the Tuinstra-Koenig law" 2014 unpublished

117. Eckmann Axel, Alexandre Felten, Artem Mishchenko, Liam Britnell, Ralph Krupke, Kostya S. Novoselov, and Cinzia Casiraghi. "Probing the nature of defects in graphene by Raman spectroscopy." Nano letters 12, no. 8 (2012): 3925-3930

118. Venezuela Pedro, Michele Lazzeri, and Francesco Mauri. "Theory of double-resonant Raman spectra in graphene: Intensity and line shape of defect-induced and two-phonon bands." Physical Review B 84, no. 3 (2011): 035433

119. Jorio A., M. A. Pimenta, A. G. Souza Filho, R. Saito, G. Dresselhaus, and M. S. Dresselhaus. "Characterizing carbon nanotube samples with resonance Raman scattering." New Journal of Physics 5, no. 1 (2003): 139

120. Ferrari A. C., J. C. Meyer, V. Scardaci, C. Casiraghi, Michele Lazzeri, Francesco Mauri, S. Piscanec *et al.* "Raman spectrum of graphene and graphene layers." Physical review letters 97, no. 18 (2006): 187401

121. Jorio A., C. Fantini, M. S. S. Dantas, M. A. Pimenta, A. G. Souza Filho, Ge G. Samsonidze, V. W. Brar *et al.* "Linewidth of the Raman features of individual single-wall carbon nanotubes." Physical Review B 66, no. 11 (2002): 115411

122. Sumanasekera G. U., J. L. Allen, S. L. Fang, A. L. Loper, A. M. Rao, and P. C. Eklund. "Electrochemical oxidation of single wall carbon nanotube bundles in sulfuric acid." The Journal of Physical Chemistry B 103, no. 21 (1999): 4292-4297

123. Mohr M., J. Maultzsch, E. Dobardžić, S. Reich, I. Milošević, M. Damnjanović, A. Bosak, M. Krisch, and C. Thomsen. "Phonon dispersion of graphite by inelastic x-ray scattering." Physical Review B 76, no. 3 (2007): 035439

124. Lazzeri Michele, and Francesco Mauri. "Nonadiabatic Kohn anomaly in a doped graphene monolayer." Physical review letters 97, no. 26 (2006): 266407

125. Hanfland M., H. Beister, and K. Syassen. "Graphite under pressure: Equation of state and first-order Raman modes." Physical Review B 39, no. 17 (1989): 12598

126. Chan C. T., W. A. Kamitakahara, K. M. Ho, and P. C. Eklund. "Charge-transfer effects in graphite intercalates: ab initio calculations and neutron-diffraction experiment." Physical review letters 58, no. 15 (1987): 1528

127. Wang Shiren, Richard Liang, Ben Wang, and Chuck Zhang. "Load-transfer in functionalized carbon nanotubes/polymer composites." Chemical Physics Letters 457, no. 4 (2008): 371-375

128. Filiou C., and C. Galiotis. "In situ monitoring of the fibre strain distribution in carbon-fibre thermoplastic composites1. Application of a tensile stress field." Composites science and technology 59, no. 14 (1999): 2149-2161

129. Lourie O., and H. D. Wagner. "Evaluation of Young's modulus of carbon nanotubes by micro-Raman spectroscopy." Journal of Materials Research 13, no. 09 (1998): 2418-2422

130. Guehenec Matthieu, Victoria Tishkova, Sylvie Dagreou, Frederic Leonardi, Christophe Derail, Pascal Puech, François Pons, Benedicte Gauthier, Pierre-Henri

Cadaux, and Wolfgang Bacsa., "The effect of twin screw extrusion on structural, electrical, and rheological properties in carbon nanotube poly-ether-ether-ketone nanocomposites." Journal of Applied Polymer Science 129, no. 5 (2013): 2527-2535

131. Williams David B., and C. Barry Carter. "The Transmission electron microscope." In Transmission Electron Microscopy, pp. 3-22. Springer US, 2009

132. Lazzara Giuseppe, Stefana. A. Milioto, M. Gradzielski, and S. Prevost., "Small angle neutron scattering, X-ray diffraction, differential scanning calorimetry, and thermogravimetry studies to characterize the properties of clay nanocomposites." The Journal of Physical Chemistry C 113, no. 28 (2009): 12213-12219

133. García-Gutiérrez Mari Cruz, Aurora Nogales Ruiz, Jaime J. Hernández, Daniel R. Rueda, and Tiberio A. Ezquerra Sanz. "X-ray scattering applied to the analysis of carbon nanotubes, polymers and nanocomposites." Optica Pura Y Aplicada 40, no. 2 (2007): 195-205

134. Kittel Charles, and Paul McEuen. Introduction to solid state physics. Vol. 8. New York: Wiley, 1976

135. Bauer Barry J., Erik K. Hobbie, and Matthew L. Becker. "Small-angle neutron scattering from labeled single-wall carbon nanotubes." Macromolecules 39, no. 7 (2006): 2637-2642

136. Schaefer Dale W., Jian Zhao, Janis M. Brown, David P. Anderson, and David W. Tomlin. "Morphology of dispersed carbon single-walled nanotubes." Chemical Physics Letters 375, no. 3 (2003): 369-375

137. Zhou Wei, M. F. Islam, H. Wang, D. L. Ho, A. G. Yodh, Karen I. Winey, and John E. Fischer. "Small angle neutron scattering from single-wall carbon nanotube suspensions: evidence for isolated rigid rods and rod networks." Chemical Physics Letters 384, no. 1 (2004): 185-189

138. Roe Ryong-Joon, and R. J. Roe. Methods of X-ray and neutron scattering in polymer science. Vol. 739. New York: Oxford University Press, 2000

139. http://www.animatedphysics.com/joinus.htm.

140. http://www.isis.stfc.ac.uk/.

141. http://www.mantidproject.org/.

142. Wignall GD T., and F. S. Bates. "Absolute calibration of small-angle neutron scattering data." Journal of applied crystallography 20, no. 1 (1987): 28-40

143. Bhaviripudi Sreekar, Xiaoting Jia, Mildred S. Dresselhaus, and Jing Kong. "Role of kinetic factors in chemical vapor deposition synthesis of uniform large area graphene using copper catalyst." Nano letters 10, no. 10 (2010): 4128-4133

144. Guiderdoni Ch, Ekaterina Pavlenko, Viviane Turq, Alicia Weibel, Pascal Puech, Claude Estournès, Alain Peigney, Wolfgang Bacsa, and Ch Laurent., "The preparation

of carbon nanotube (CNT)/copper composites and the effect of the number of CNT walls on their hardness, friction and wear properties." Carbon 58 (2013): 185-197

145. Chehaidar A., A. Zwick, R. Carles, and J. Bandet. "Multiple-order Raman scattering and the density of vibrational states in a-GaAs." Physical Review B 50, no. 8 (1994): 5345

146. Puech Pascal, Ahmad Ghandour, Andrei Sapelkin, Cyril Tinguely, Emmanuel Flahaut, David J. Dunstan, and Wolfgang Bacsa. "Raman G band in double-wall carbon nanotubes combining p doping and high pressure." Physical Review B 78, no. 4 (2008): 045413

147. Dresselhaus M. S., A. Jorio, A. G. Souza Filho, and R. Saito. "Defect characterization in graphene and carbon nanotubes using Raman spectroscopy." Philosophical Transactions of the Royal Society A: Mathematical, Physical and Engineering Sciences 368, no. 1932 (2010): 5355-5377

148. Reich Stephanie, Christian Thomsen, and Janina Maultzsch. Carbon nanotubes: basic concepts and physical properties. John Wiley & Sons, 2008

149. Seferis James C. "Polyetheretherketone (PEEK): Processing-structure and properties studies for a matrix in high performance composites." Polymer Composites 7, no. 3 (1986): 158-169

150. Kuo M. C., C. M. Tsai, J. C. Huang, and M. Chen. "PEEK composites reinforced by nano-sized SiO< sub> 2</sub> and Al< sub> 2</sub> O< sub> 3</sub> particulates." Materials Chemistry and Physics 90, no. 1 (2005): 185-195

151. Blundell D. J., and B. N. Osborn. "The morphology of poly (aryl-ether-ether-ketone)." Polymer 24, no. 8 (1983): 953-958

152. Sarasua J. R., P. M. Remiro, and J. Pouyet. "Effects of thermal history on mechanical behavior of PEEK and its short-fiber composites." Polymer composites 17, no. 3 (1996): 468-477

153. Rong Changru, Gang Ma, Shuling Zhang, Li Song, Zheng Chen, Guibin Wang, and P. M. Ajayan. "Effect of carbon nanotubes on the mechanical properties and crystallization behavior of poly (ether ether ketone)." Composites Science and Technology 70, no. 2 (2010): 380-386

154. Ferrari Andrea C., and Denis M. Basko. "Raman spectroscopy as a versatile tool for studying the properties of graphene." Nature nanotechnology 8, no. 4 (2013): 235-246

155. Stuart B. H. "Polymer crystallinity studied using Raman spectroscopy." Vibrational spectroscopy 10.2 (1996): 79-87

156. Nair R. R., P. Blake, A. N. Grigorenko, K. S. Novoselov, T. J. Booth, T. Stauber, N. M. R. Peres, and A. K. Geim. "Fine structure constant defines visual transparency of graphene." Science 320, no. 5881 (2008): 1308-1308

157. Shuba M. V., G. Ya Slepyan, S. A. Maksimenko, C. Thomsen, and A. Lakhtakia. "Theory of multiwall carbon nanotubes as waveguides and antennas in the infrared and the visible regimes." Physical Review B 79, no. 15 (2009): 155403

158. Bassil A., P. Puech, G. Landa, W. Bacsa, H. Hubel, D. J. Dunstan, S. Barrau *et al.* "Enhanced Raman signal of CH3 on carbon nanotubes." In MRS Proceedings, vol. 858, pp. HH14-7. Cambridge University Press, 2004

159. Brosse Anne-Carine, Sylvie Tencé-Girault, Patrick M. Piccione, and Ludwik Leibler. "Effect of multi-walled carbon nanotubes on the lamellae morphology of polyamide-6." Polymer 49, no. 21 (2008): 4680-4686

160. Golosova Anastasia A., Joseph Adelsberger, Alessandro Sepe, Martin A. Niedermeier, Peter Lindner, Sergio S. Funari, Rainer Jordan, and Christine M. Papadakis. "Dispersions of polymer-modified carbon nanotubes: a small-angle scattering investigation.", The Journal of Physical Chemistry C 116, no. 29 (2012): 15765-15774

161. Hammouda B., D. G. Reichel, and C. J. Wolf. "Neutron scattering from PEEK." Journal of Macromolecular Science—Physics 27, no. 4 (1988): 445-454

162. Tsuji Masaki, Hidetoshi Kawamura, Akiyoshi Kawaguchi, and Ken-ichi Katayama. "TEM Studies on Solution-Grown Crystals of Poly (aryl-ether-ether-ketone)(PEEK)." Bulletin of the Institute for Chemical Research, Kyoto University 67, no. 2 (1989): 77-88

163. Tishkova V., G. Bonnet, F. Pont, B. Gautier, P. H. Cadaux, P. Puech, and W. S. Bacsa. "Uniform dispersion of nanotubes in thermoplastic polymer through thermal annealing." Carbon 53 (2013): 399-402

164. Jhi Seung-Hoon, Steven G. Louie, and Marvin L. Cohen. "Electronic properties of oxidized carbon nanotubes." Physical Review Letters 85, no. 8 (2000): 1710

165. Cadek M., J. N. Coleman, V. Barron, K. Hedicke, and W. J. Blau. "Morphological and mechanical properties of carbon-nanotube-reinforced semicrystalline and amorphous polymer composites." Applied Physics Letters 81, no. 27 (2002): 5123-5125

166. Krause Beate, Mandy Mende, Petra Pötschke, and Gudrun Petzold. "Dispersability and particle size distribution of CNTs in an aqueous surfactant dispersion as a function of ultrasonic treatment time." Carbon 48, no. 10 (2010): 2746-2754

Probing dispersion and interaction of carbon nanotubes with metal and polymer matrices

The incorporation of carbon nanotubes (CNTs) into polymers and metals modifies their intrinsic properties. Dispersing CNTs uniformly in a matrix remains challenging due to strong tube agglomeration. Raman spectroscopy is a compelling technique to detect the presence of CNTs and their interaction with the environment. In this work, Raman spectroscopy is applied in association with other techniques to investigate CNTs in a metallic or polymer matrix. Doping with superacids, analysis of defects in friction wear and CNT dispersion are investigated. Statistical analysis of Raman images are used to generate histograms of Raman bands maps in order to estimate the amount of CNTs and their dispersion. The diffusion of a Poly (Ether Ether Ketone) PEEK thermoplastic polymer into agglomerated carbon nanotubes when annealing on the surface of a polymer sheet is studied by Raman imaging and transmission electron microscopy. Electronic transport measurements as a function of temperature and CNT concentration show high electrical conductivity consistent with the formation of a uniform percolating CNT network.

Sonder la dispersion et l'interaction des nanotubes de carbone avec des matrices métalliques et polymères

L'incorporation de nanotubes de carbone (NTC) dans des polymères et des métaux modifie leurs propriétés intrinsèques. Disperser des NTCs uniformément dans une matrice reste difficile du fait de leur forte agglomération. La spectroscopie Raman est une technique particulièrement adaptée pour détecter la présence et l'interaction avec l'environnement de NTCs. Dans ce travail, la spectroscopie Raman est utilisée, en association avec d'autres techniques, pour étudier les NTCs dans une matrice métallique ou polymère. Le dopage avec des super-acides, l'analyse de défauts dans les zones d'usure et la dispersion des NTCs sont abordés. L'analyse statistique des images Raman permet de générer des histogrammes permettant d'estimer la quantité et la dispersion des NTCs. La diffusion lors de recuit d'un polymère thermoplastique poly (éther-éther-cétone) ou PEEK dans des NTCs agglomérées est étudiée par imagerie Raman et microscopie électronique. Les mesures de transport électronique en fonction de la température et de la concentration de NTCs montrent une forte conductivité électrique compatible avec la formation d'un réseau percolant de NTCs.